ABSTRACT

Title of Thesis:	PHYSICS-OF-FAILURE METHODOLOGY FOR ACCELERATED THERMAL CYCLING OF LCC SOLDER JOINTS
Name of degree candidate:	Timothy Paul Rothman
Degree and Year:	Master of Science, 1995
Thesis Directed by:	Professor Abhijit Dasgupta Department of Mechanical Engineering University of Marlyand

This research presents a case study where existing physics-of-failure models and Bayesian statistical methods are used in conjunction to quantify the test-time compression achieved during accelerated temperature cycling tests on leadless solder joints. Different combinations of substrate materials and package styles are evaluated with physics-of-failure models and valuable information is obtained from a relatively small population of test specimens under accelerated stresses, because the critical variables are identified, and their influences on the stress magnitude are quantified. Bayesian statistical analysis is employed to obtain an acceleration transform, determine the confidence on the calculations, and determine which outliers are contaminating the database. In addition to accelerating the stress levels, the total test time is further minimized by tailoring the stress drivers in each sample such that multiple stress levels can be achieved under a single loading, which eliminates the need for repeating the test at multiple load levels. This research presents the details of how the models and statistical methods are applied, the results of evaluating different material combinations and package styles, problems encountered during the test, and a summary of the acceleration transforms obtained from the test. Analytical predictive models for life predictions are essential and will obviously result in significant savings of cost and time. The methods used in this are general enough to be applied to screening, qualification, and reliability enhancement tests of a wide range of new or existing electronics assemblies.

PHYSICS-OF-FAILURE METHODOLOGY FOR ACCELERATED THERMAL CYCLING OF LCC SOLDER JOINTS

by

Timothy Paul Rothman

Thesis submitted to the Graduate School
of The University of Maryland in partial fulfillment
of the requirements for the degree of
Master of Science
1995

c.1
MD

Advisory Committee:
Professor Abhijit Dasgupta, Chairman/Advisor
Professor Michael Pecht
Professor Donald Barker

Maryland
LD
3231
.M70m
Rothman,
T.P.

TABLE OF CONTENTS

Section	Page
List of Tables	iv
List of Figures	v
Nomenclature	vii
1. Introduction	1
2. Accelerated Test Procedure	7
2.1 Test Samples And Matrix	7
2.2 Qualitative Analysis of Failure Mechanism	11
2.3 CTE Characterization	13
3. Statistical Evaluation of Test Results	22
3.1 Weibull Statistical Probability Distribution	22
3.2 Statistical Evaluation of Mechanism, Site, and Mode of Failure	25
3.3 Acceleration Transform Based on a Bayesian Approach	28
4. Physics-of-Failure Evaluation of Test Results	36
4.1. Physics-of-Failure Models Considered	36
4.1.1 IPC Physics-of-Failure Model	38
4.1.2 CALCE Energy Partitioning Damage Model	44
4.2. Stress Analysis	47
4.2.1 Constitutive Models	47
4.2.2 FEM Modeling	52
4.2.3 FEM Results	55
4.3 Energy Partitioning Update	60
4.4 Physics-of-Failure Acceleration Transforms	65
5. Conclusions and Discussions	70
6. Contributions	73
Appendix A Dimensions and Mat. Properties of Modules Used in Accelerated Test	74

Appendix B Failure Data 75

Appendix C Histograms of Accelerated Test Failure Data 79

Appendix D CTE Measurements (Normalized by Component CTE) 94

Appendix E Failure Data Grouped According to Strain Range 103

Appendix F Algorithm to Compute Confidence Contours on Distribution Parameters 104

Appendix G Weibull Posterior Parameter Distribution at Different Strain Levels 105

Appendix H Plastic Constitutive Constants at Different Temperatures and Strain rates 108

Appendix I Material Properties and Dimensions Used for FEM Analysis, FEM Meshes and Contour Plots of Mises Equivalent Stress 111

Appendix J Sample Abaqus Input File 119

Appendix K Fortran Post Processing File for FEM Analysis 124

Appendix L Matlab Post Processing File Used to Create Hysteresis Plots 132

Appendix M Hysteresis Plots From FEM Analysis 136

Appendix N Acceleration Transforms at Different Percent Probability of Failure 142

7. References 143

LIST OF TABLES

Number		Page
2.1	Differences in Calculated and Measured CTEs	18
3.1	Classification of Wire Bond and Solder Joint Failures	27
4.1	Previous Fatigue Constants	45
4.2	Temperature and Strain Rate Dependence of Plastic Properties	48
4.3	Creep Constants Reported by Various Investigators	50
4.4	Fatigue Life from FEM Analysis and Energy Partitioning Damage Model	57

LIST OF FIGURES

Number	Page
2.1 Double-Sided Multilayered Module	10
2.2a-e Solder Joint Photographs at 30X Magnification	12
2.3 Placement of Strain Gages for CTE Characterization of Modules	15
2.4 CTE Measurements for Heatsink CTE > Substrate CTE	20
2.5 CTE Measurements for Heatsink CTE < Substrate CTE	21
3.2 Weibull Hazard Rate Showing Wire Bond vs. Solder Joint Failures	26
3.3 Wire Bond Failure Plotted Against Thermal Cycles	26
3.4 Three-Dimensional Weibull posterior Density	31
3.5 Elimination of Outliers Based on Confidence Contours	32
3.6 Acceleration Transform Based on a Bayesian Statistical Approach	35
4.1a-c Effect of Component Size, Module Material, and Component Placement on Time to Failure	43
4.3 Creep Strain Rate versus Temperature at Different Stress Levels	51
4.4a-b Example Hysteresis Plot of Mises Equivalent Stress vs. Total Eq. Strain	59
4.5 $L_d\Delta\alpha$ versus N_f from Experimental Data at 50% Probability of Failure	63
4.6 Creep work from FEM versus N_{fc} from Experimental Data and Energy Partitioning Damage Model	63
4.7 Updated Energy Partitioning Fatigue Constants	64
4.8 Acceleration Transforms at 50% Probaility of Failure	69
Appendix B Histograms of Accelerated Test Failure Data	79

Appendix D CTE Measurements (Normalized by Component CTE) 94

Appendix G Weibull Posterior Parameter Distribution at at Differnet Strain Levels 105

Appendix H Temp. and ε Dependance of Plastic Constitutive Model Constants 108

Appendix I FEM Meshes and Contour Plots of Mises Equivalent Stress 111

Appendix M Hysteresis Plots From FEM Analysis 136

Appendix N Acceleration Transforms at Different Percent Probability of Failure 142

NOMENCLATURE

MTTF	mean-time-to-failure
MTBF	mean-time-between-failure
FMEA	failure mode effects analysis
failure mode	physically observable change caused by the failure mechanism
failure mechanism	underlying process by which the specific combination of thermal, mechanical, electrical, stresses induce failure
failure site	location where a failure occurs
physics-of-failure	approach which involves the use of testing procedures which are based on quantitative models of the expected failure mechanisms derived and validated from previous test results
PCB	printed circuit board module consisting of substrates, and heatsink
CTE (α)	coefficient of thermal expansion
LCC	leadless chip carrier
PTH	plated through hole
bond pads	area where solder connects to LCC and substrate
castellation	semi-circular region where solder joint is attached to LCC
P(t)	cumulative probability of failure
B	slope parameter of Weibull distribution
θ	scale parameter or characteristic life of Weibull distribution
t_o	failure free time parameter of Weibull distribution
h(t)	Weibull hazard rate
N_f	thermal cycles to failure

$\Delta\gamma$	shear strain range
$\Delta\alpha$	differential thermal expansion
h	solder joint height
L_d	maximum diagonal distance between solder joints on a component
T_{sj}	mean cyclic solder joint temperature
ΔT	cyclic temperature range
ΔT_{eff}	calculated effective cyclic temperature
U_e	elastic strain energy density
W_p	plastic work density dissipated per thermal cycle
W_c	creep work density dissipated per thermal cycle
$D_{T,\,e,\,p,\,c}$	total, elastic, plastic, and creep damage respectively
ε	equivalent mechanical strain
E	elastic modulus
σ	equivalent (von Mises) stress
K	plastic strength coefficient
n_p	plastic strain hardening exponent.

1. Introduction

The failure of an electronic system is the loss of its ability to perform its desired functions. Actuarial statisticians lump failures into one of three categories: infant mortality, random failure or sudden overstress, and wear-out failure, depending on the trend of the failure rates. The phenomena of infant mortality, sudden overstress, and wear-out correspond to different failure mechanisms or their combination. The common practice is to quantify our ignorance of the stresses, materials, configurations and other variables using stochastic distribution to represent their behaviors. But even these stochastic characteristics cannot be quantified without an intimate knowledge of the characteristics of failure. [1]

In traditional reliability analysis for electronic systems application, typical practice is to assess the mean-time-to-failure (MTTF), constant mean-time-between-failure (MTBF), or constant failure rate by assuming an exponential distribution. This exhibits a blatant disregard for the individual failure mechanisms and their effect on field reliability, leading to poor estimates of time to failure. This is especially true for electronic components where traditional reliability prediction is based on empirical models fitted to field data where the root causes of failures are ignored. MIL-HDBK-217 [2] is one such example.

Failures of an electronic module are due to a complex set of interactions between (i) the "stresses" (*i.e.* environment parameters that act on and within the module) and (ii) the materials and configurations of components, solder interconnects, and boards. In order to

understand the interaction between the environment and the electronics device, as well as understand the effect of the critical variables on the statistical distribution and thus the life, physics-of-failure methodology must be used. From the view point of physics-of-failure, the characteristics of the failures of an electronic system should be defined by the failure mode, failure mechanism, and failure site. [3,4]

Failure mode is a physically observable change caused by the failure mechanism, such as an open, a short, an increase in resistance, or any other electrical change in the device. Failure mode can serve as a failure criterion in accelerated testing, and therefore, the traditional failure mode effects analysis (FMEA) is a helpful tool for identifying failure phenomena. However, in traditional FMEA, the failure modes can not be quantitatively related to applied stresses, material damage, and product life by a physical model, and therefore is not a sufficient analysis tool.

The failure mechanism is the underlying process by which the specific combination of thermal, mechanical, electrical, stresses induce failure. The process of a failure usually starts from existing defects such as voids in a material or microcracks in the interface of two materials.

The location where a failure occurs is called the failure site. The failure site can be classified into different levels such as components, interconnects, substrate, and housing. A failure mechanism could occur at different sites. The failure mechanisms should not be

confused with failure modes and initial defects, although they are often called the root cause of failures.

A correct reliability qualification procedure for critical components should begin with an investigation of all critical failure mechanisms, followed by an identification of where and when they may occur, and their effect on the operation of the electronic module over the required useful life. Failures must be identified with respect to the failure mechanisms that could potentially be activated in an electronic module during operation, with the understanding that a given failure mechanism can occur at many sites. Therefore, investigation of failure mechanism, site, and mode should serve as a guide for accelerated testing.

In the development of an electronics module, timely and cost effective techniques for qualification, reliability enhancements, and screening are extremely important to minimize the time-to-market and satisfy the customer expectation of long-term reliability. In order to anticipate the likelihood of failure under long-term operational conditions, it is necessary to fully understand the basic failure mechanisms and then take steps to guard adequately against the manifestation of these failure mechanisms. [5, 6] The ability of an electronic assembly to perform its required function must be evaluated because the reliability of a module is a function of the reliability of individual components and of the interconnects. Testing to ensure adequate reliability and quality is usually done under accelerated stresses to achieve test time compression. Qualification tests as defined in this study are performed during product

development and are intended to assess the product's ability to conform to nominal design and manufacturing specifications by satisfying long term reliability requirements. Reliability enhancement testing is performed to guide the ruggedization of products when the demonstrated reliability is deemed to be inadequate. Screening provides a means by which an investigator may find fragile or faulty items in an electronic module by means of a test with appropriately accelerated stresses without weakening or causing the failure of sufficiently robust items. In each case, the necessity to quantify the results of the test remains. Applying physics-of-failure methodology to an accelerated test provides the investigator with information other than just pass-fail. [7]

This research is performed to introduce the inexperienced engineer to the physics-of-failure methodology as it applies to accelerated testing. The approach is illustrated for testing of solder joint interconnects. The physics-of-failure methodology is employed in detail to evaluate the results of the accelerated test and provide useful information on long term reliability of electronic components. Around the electronic packaging industry, accelerated test are performed regularly to evaluate the package design relative to each particular application. [8,9] However, these test results are often evaluated using stochastic approaches in which the effect of the failure mechanisms is evaluated without regard to actual mechanism. In fact, as this study shows, some mechanisms which are unwanted may appear. While statistical methods can sometimes help identify these mechanisms, it is not possible to correctly evaluate them using statistics alone. It is suggested that statistical methods be used to reinforce the physics-of-failure methods, and not be used in place of them.

A properly designed accelerated test must not only provide accurate information, but also provide economic savings and quick turn-around during development of new products or during process changes in existing products. Test time compression is achieved by accelerating the stress levels on judiciously chosen test specimens. An acceleration transform is a useful tool which can be used to relate the accelerated test results to any operational environment. Unfortunately, accelerated tests are often performed without identifying the potential failure mechanisms, without adequately investigating the existing acceleration transform models, and without continuously modifying the test specifications for introduction of new technology. Therefore, testing based solely on historical testing specifications can be costly and lead to erroneous conclusions. Furthermore, empirical parametric studies using accelerated testing techniques often require the testing of many samples under multiple load histories in order to create an accurate, populated database. By carefully varying the critical variables in the test specimens, the time required for the parametric-accelerated test can be effectively compressed by allowing the investigator to achieve multiple stress levels from a single load history.

The physics-of-failure approach involves the use of testing procedures which are based on quantitative models of the expected failure mechanisms derived and validated from previous test results. In addition, the physics-of-failure approach provides a method to obtain acceleration transforms and useful trends from limited amount of test data with confidence. This study attempts to apply the physics-of-failure approach to accelerated testing of surface-mount components with leadless solder joints, and proposes a practical procedure for

extracting information from a single accelerated test.

Solder joints typically fail due to cyclic creep-fatigue interactions under thermally applied cyclic stress. The driving stress is due to the thermal expansion mismatch between the component and the printed circuit board (PCB), as well as the shear stress in the solder joint near the bond pad due to the thermal expansion mismatch between the solder material and the bond pad. The critical variables in this example of an accelerated test are the differences of the coefficients of thermal expansion (CTEs) of the PCB material and the components. Other critical variables include the component dimensions and the geometry of the solder joint. Physics-of-failure models are used to correctly evaluate the acceleration transform for solder joint reliability without having to create a huge experimental database.

The parametric-accelerated fatigue test for surface-mount solder joints is described in Section 2. The observed failure mechanisms statistical evaluation of the test results are discussed in Section 3. The physics-of-failure models used to quantify the results of the test and extract acceleration transform information based on the physics-of-failure are discussed in Section 4. Conclusions and discussions are presented in Section 5.

2. Accelerated Test Procedure

As discussed in Section 1, in order to correctly evaluate the ability of an electronics assembly to withstand long term conditions in a harsh operating environment, the wearout mechanisms must be assessed and accelerated. In doing so, care must be taken to accelerate the mechanisms that will cause failure in field conditions without accelerating those mechanisms which would not ordinarily cause damage. It is well understood and widely accepted that the driving stress which defines solder joint reliability under thermomechanical cyclic loading is the differential thermal expansion caused by the size of the component and the difference in the CTE between the substrate and the component. Additionally, the height of the solder joint, cross sectional profile of the solder joint, formation of intermetalics, and bond pad integrity can affect fatigue life of the solder joint.

2.1 Test Samples and Matrix

In this study, the critical variables which are considered are the differential thermal expansion between the component and the substrate and the size of the components. It is assumed that the solder joint geometry, quality, and metallurgy are nominally uniform across each of the modules. It is also assumed that the CTE of the module is uniform across each of the modules such that the same size components on each of the modules experiences the same stress due to the differential expansion regardless of its location on the module. These assumptions are then evaluated to determine their validity within the scope of accelerated testing.

Fifteen double-sided, symmetric, multilayered circuit board modules, consisting of ceramic leadless chip carriers (LCCs) and plated through holes (PTHs), are chosen for this study. Each module consists of two PCB substrates adhesively bonded to a thermally conductive core or heatsink. The samples chosen in this study have different combinations of PCB, heatsink, and adhesive material as given in Appendix A. The dimensions and material properties of the modules are also given in Appendix A. Each module consists of four 68-pin LCCs, six 48-pin LCCs, twenty 32-pin LCCs, and two PTH arrays as shown in Figure 2.1. Thus, there are many stress levels for a single load history. The effect of the size of the components, placement of the components, and materials used to manufacture the modules on the stresses can be evaluated and comprehensive acceleration transforms can be created from a single load history because of the multitude of stress levels reached in different solder joints.

Each component is daisy chained and continuously digitally monitored using Anatech event detectors, and are polled every 10 seconds. If a transient resistance spike in excess of 300 Ohms is detected, temperature and elapsed thermal cycles for the event are recorded in a database. This type of intermittent, transient change in resistance is typical of fatigue failures. The occurrence of 15 such events within less than 20 thermal cycles is defined as a failure of the solder joint or PTH because the event detectors retain information on only the first 15 events.

The thermal cycling for the parametric-accelerated test is performed in an accelerated stress

test chamber, which is capable of temperature ranges of 200 °C to -100 °C (392 °F to -148 °F) at a temperature rate of change of 60 °C/min. (140 °F/min.). The accelerated test temperature profile chosen for this study has temperature extremes in this profile of 90 °C and -55 °C. These extremes are typical of the harshest conditions which will be experienced in an operating environment. In fact the temperature range is analogous to the temperatures experienced by a module mounted on an airplane which takes off from an asphalt runway located in a desert and flies at high altitudes in Siberia. The thermal rate of change is chosen to be 10 °C/min. in order to ensure that all of the modules located in the chamber will experience the same temperatures. The temperature holding or soak time of 23.5 minutes at the high temperature excursion is chosen to ensure that there are no thermal gradients in the modules, and facilitate the time and temperature dependent stress relaxation. A soak time of 5.5 minutes is used at the low temperature excursion in order to ensure that there are no thermal gradients in the modules. Each thermal cycle takes 58 minutes to complete. In order to achieve failure of a sizable percentage of the population, the cycling is continued until 1000 thermal cycles are completed.

To measure the temperature distribution in the test chamber, 15 thermocouples are strategically placed in the testing array. The air stream temperature differs by as much as 10 °C from the temperature measured at the module which is located furthest from the plenum at the front of the chamber while ramping. The air stream temperature and the module temperatures coincide within the first few minutes of the dwell periods. However, due to close proximity of the boards to each other, and the interference of the air flow caused by the cables connecting the boards to the Anatech devices, the temperature

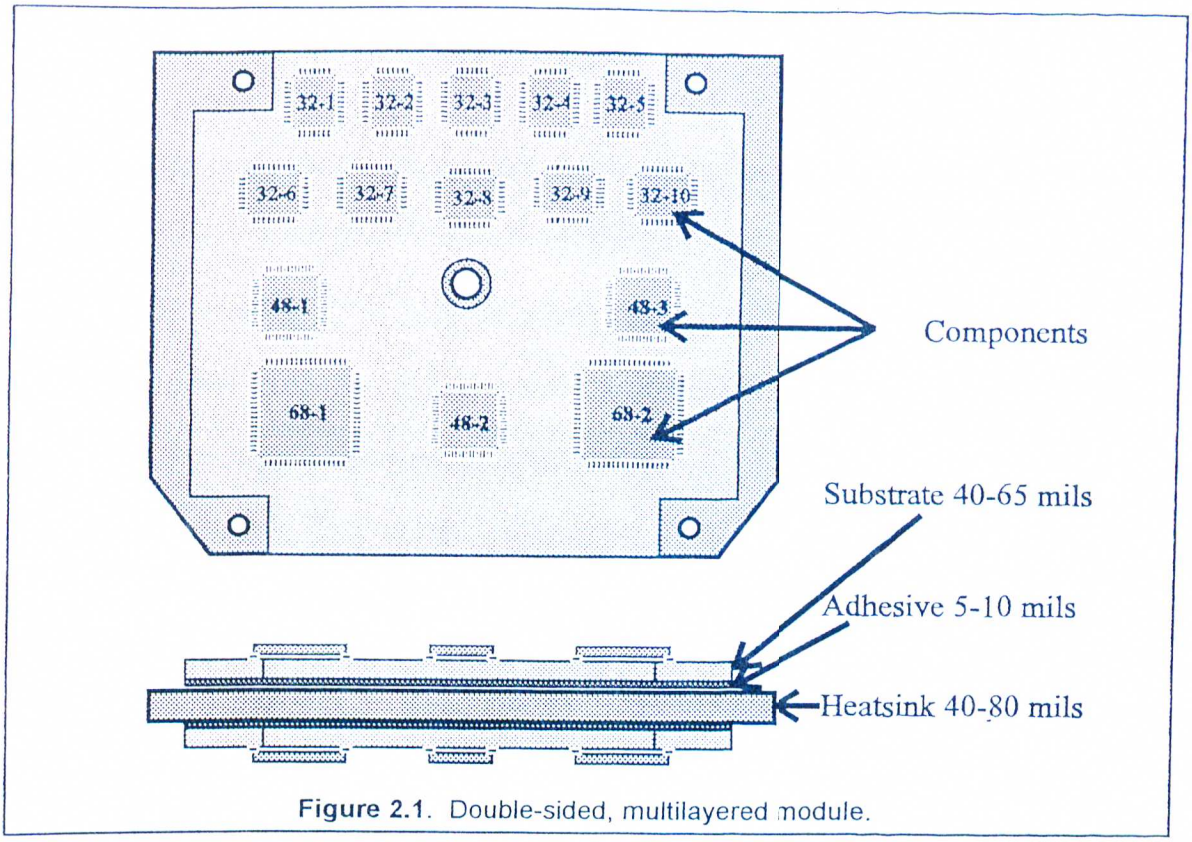


Figure 2.1. Double-sided, multilayered module.

distribution across each board may be marginally non-uniform. However, this difference is found to be less than 3 °C, which is within acceptable limits.

The failure data for solder joint failures is shown in Appendix B. The failure data is separated by groups which have the same approximate CTE. In order to qualitatively obtain some trends of the failure data, histograms are shown in Appendix C. It is apparent from these histograms that the trends follow intuition. The larger components typically fail before the smaller components within the same group. However, there are some 32 pin components which failed on Group 2 (CIC core) before the 48 pin components failed on the same module. Statistical analysis along with physics-of-failure methodology will be used in Sections 2 and 3 to explain this phenomenon.

2.2 Qualitative Analysis of Failure Mechanism

As discussed in the Introduction, the shape of the solder joint is also assumed to be nominally uniform, which implies that the variabilities in the shape of the solder joint play no role on the reliability. This study has shown that there is, in fact, a variability in the shape of the solder joint. Figure 2.2a shows a 30X magnification photograph of a premature failure which occurred on a 32-pin LCC on a polyimide/fiberglass board with a CIC heatsink. This premature failure occurred prior to any 48-pin LCC failures on that board. This premature failure was not an isolated event, and the 32-pin LCCs on the CIC heatsink boards (modules 4A and 4B) consistently occurred earlier than the 48-pin LCCs on those boards. Precise characterization of the CTEs of these modules showed that there was delamination of the substrate from the heatsink. Although the 68-pin LCC shown in Figure 2.2b was photographed at 341 thermal cycles and some damage inevitably has occurred between the times at which each photograph was taken, it serves to qualitatively illustrate that there is some variation in the shapes of the solder joints and that variation could affect the solder joint reliability. The solder joint on the 32-pin LCC has a higher concentration of solder near the neck (castellation) where the solder connects to the component, and the 68-pin LCC has a thinner column-like shape. The amount of bulbousness is controlled by the volume of solder deposited in the board prior to reflow.

As stated earlier, the driving factor which determines the reliability of the surface mount components is the shear stress at the solder joint caused by differential thermal expansion

of the substrate and the component. Figure 2.2c shows a 68-pin LCC on a kevlar board with a carbon composite heatsink. There were no failures recorded on this module. Figure 2.2d shows a 68-pin LCC on a polyimide/CIC foil board with an aluminum heatsink. Although there were no failures on the Kevlar board, some fatigue damage is noted by the striations at the castellation.



Figure 2.2a Polyimide on CIC LCC 32
Photographed at 950 Cycles
Failed at 500 Thermal Cycles
Adhesive Rigid Bond
Normalized CTE 1.7



Figure 2.2b Polyimide on CIC LCC 68
Photographed at 341 Cycles
Completed 1000 Cycles without Failure
Adhesive: Rigid Bond
Normalized CTE 1.7



Figure 2.2c Kevlar/Epoxy on Carbon Composite LCC 68
Photographed at 950 Cycles
Completed 1000 Cycles without Failure
Adhesive: Compliant Bond
Normalized CTE 1.57

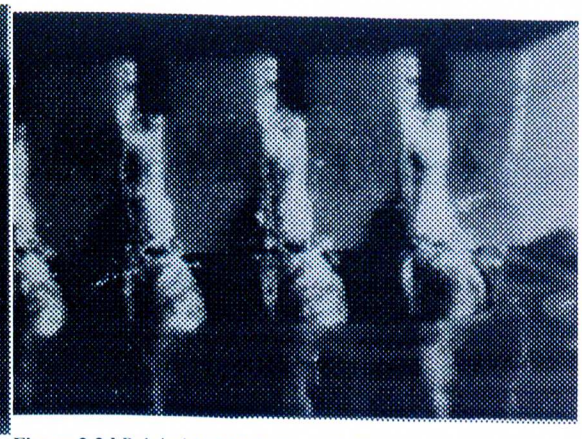


Figure 2.2d Polyimide/CIC Foil on Al 6061-T6 LCC 68
Photographed at 341 Cycles
Failed at 179 Cycles
Adhesive: Compliant Bond
Normalized CTE 1.71

2.3 CTE Characterization

As stated in the Introduction, the driving factor which determines the reliability of the surface mount components is the shear stress at the solder joint caused by differential thermal expansion of the substrate and the component; therefore, precise characterization of the CTEs of the materials is essential to perform an accurate reliability analysis. This study illustrates that estimation of multilayered assemblies is a difficult task and experimental characterization is sometimes necessary.

The CTEs of the module materials are either taken from in-house data, provided by the manufacturer of each of the substrates and heatsinks, or taken from the CALCE database. The CALCE software contains a laminate analysis tool which is used to determine the CTEs of the glass-polyimide/CIC (copper-invar-copper) foil substrates. These substrates are comprised of glass-polyimide reinforced with two 6 mil thick 12.5/75/12.5 (%copper-%invar-%copper) CIC foils. However, the CTEs of bonded assemblies cannot be predicted well with laminate analysis because laminate analysis does not perform well for imperfect bonding or viscoelastic materials such as the adhesives used to attach the substrates to the heatsinks in each module. The inability of a compliant bond to couple the CTE of the substrate to that of the heatsink material cannot be precisely determined using laminate analysis because it is formulated for completely rigid or perfectly bonded elastic materials. Therefore, it is necessary to characterize the CTEs of the modules through careful experimental measurements.

The CTEs are measured as per Measurements Group Technical Note 513. The surface of the substrates of the modules are prepared by removing the solder mask and conformal coating and the 350 Ω strain gages are mounted using M-Bond 600 adhesive according to Measurements Group Instruction Bulletin B-130-14. The gages are then clamped to ensure a thin, hard glue line. The assembly is then placed in the thermal chamber and ramped at 10 °C/min. to 150 °C where the adhesive is cured for two hours. In order to minimize the effects of the change in resistance of the lead wires on the strain measurements due to thermal change in resistivity, a three wire configuration is used. Further, the length (≅ 50 cm) and the size of the wire (30 AWG =.25 mm diameter) is kept as small as possible. Finally, a protective coating (3140 RTV) is applied to the strain gage.

The strain gages are placed in the active arm in a quarter Wheatstone Bridge configuration. A reference gage mounted on a material with a known, near zero CTE (titanium silicate) is placed in a separate quarter bridge. The reference gage is also placed in the thermal chamber for thermal compensation of the measurement. The strain experienced by the reference gage is mainly due to the thermal response of the gage, and not the material on which the gage is mounted due to the fact that the reference material has a near zero CTE. In this way any effects of the CTE of the gage and the internal heating effects of the gage due to the bridge voltage are known. In addition, the transverse sensitivity of the strain gage (although small) should be taken into account.

The strain in the reference gage is subtracted from the apparent strain of the measurement gage to give the actual strain of the material to be measured. The slope of a linear least squares regression of the strain measurements taken at 10 °C increments versus temperature gives an averaged CTE of the material over the temperature range. This averaged value is used as inputs into the physics-of-failure models. The x-intercept of the linear least squares regression is the temperature at which the bridges are balanced.

The CTE measurements are done on the surface of each module substrate at four locations as shown in Figure 2.3 (both in plane directions x and y, in the center and edge of the substrate). Measuring the CTEs in two places gives valuable information about the CTE distributions in each module. Measuring the CTEs in two places and two directions provides insight into potential delamination failure modes of the module.

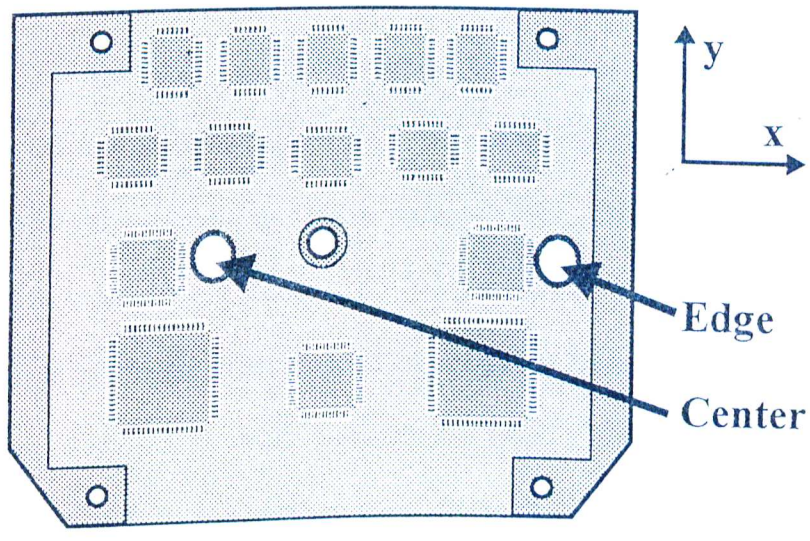


Figure 2.3. Placement of Strain Gages for CTE Characterization of Modules.

In order to plot the CTE as a function of temperature, the strain as a function of temperature is divided by ΔT, where ΔT is the absolute temperature difference relative to the temperature at which the bridge is balanced. Taking this local gradient becomes numerically unsound due to the fact that there is some noise in the strain measurements (+/- 10 $\mu\varepsilon$), and ΔT approaches zero near the balance temperature (division by zero). In order to smooth the data, weighted cubic splines with linear interpolation functions at the endpoints are fitted through every third CTE calculation. The average of the three sets of cubic splines fits the data by weighting the outliers less. This technique of averaging the cubic splines to smooth the experimental data provides the CTE as a function of temperature as opposed to an averaged CTE which provides a single value over the entire temperature range. The CTEs are then normalized by the component CTE in order to gain insight into the stress levels experienced by the components.

Figure 2.4 shows the measured CTE distribution of one module in which the heatsink has a CTE which is greater than the substrate CTE. The adhesive which is used to attach the substrate to the heatsink becomes rigid at low temperatures. The measurements taken at the middle of the module become higher at low temperatures. This is due to the adhesive becoming rigid, making the substrate respond more like the heatsink which has a lower CTE. The inverse effect occurs for the measurement taken at the edge of the module due to some delamination of the substrate from the heatsink at the edge. These measurements highlight the limitation in assuming a uniform CTE distribution across each module. In

fact, the components located near the edge on this module undergo less strain than the center components at low temperatures. Further, these measurements emphasize inaccuracies in calculating the module CTE instead of measuring it, and the errors which can be introduced by assuming the CTE to be independent of temperature.

Figure 2.5 shows the CTE distribution of one module in which the heatsink CTE is less than the substrate CTE. The adhesive which is used to attach the substrate to the heatsink is compliant for the whole temperature range. As usual, the measurements taken on the edge are driven by the substrate and the measurements taken near the middle are driven by the CTE of the heatsink. The reason the edge measurement in the x-direction is higher than the middle measurement in the x-direction is because the substrate CTE is higher than the heatsink. The measurements taken in the y-direction do not follow the same trend, because the strain gages oriented in the y-direction are on the x-edge, not the y-edge, as shown in Figure 2.3. Note that although the adhesive is considered relatively compliant at all temperatures, the viscoelastic response of the adhesive does make it stiffer at low temperatures. This tends to couple the CTE of the substrate to the lower CTE of the heatsink at low temperatures. In addition, the substrate material becomes stiffer at low temperatures thus reducing the CTE. The fact that the CTE drops off drastically at lower temperatures is a desirable response. In fact, this is the only module which had no failures after 1000 thermal cycles. Again, the inaccuracy of estimating a uniform, constant CTE over the temperature range is illustrated clearly.

The CTE measurements for the remaining modules is presented in Appendix D. Note the modules with the CIC heatsink (modules 4A, B) which had 32-pin components failing before the larger 48-pin components has a very large CTE near the edge in the x-direction. This measurement was repeated several times and with different strain gages at that location to ensure that no errors were caused by the experimental setup. The CTE measurements show that the substrate has become delaminated from the heatsink due to the thermal cycling. This is a very simple example of statistical data (histograms) which must be verified using the physics-of-failure approach. The experimental data suggested a control problem with these components, but careful analysis of the situation uncovered a new failure mechanism: in this case the new failure mechanism is delamination of the substrate from the heatsink. Although this is a very simple example of using the physics-of-failure methodology in conjunction with a statistical analysis, it serves to illustrate the point. Now that the new mechanism has been identified, care can be taken in the future to prevent it from affecting the useful life of the assembly and contaminating the failure data.

Board Number	X- Middle CTE Normalized	X- Edge CTE Normalized	Y- Middle CTE Normalized	Y- Edge CTE Normalized	Board CTE (avg)	Calc CTE
1	1.76	1.6			1.67	1.67
2A	Data from 1	Data from 1			1.67	1.67
2B	Data from 1	Data from 1			1.67	1.67
3	1.65	1.8			1.72	1.5
4A	1.61	1.69	1.8	3.7	1.7	1.48
4B	Data from 4A	Data from 4A	Data from 4A	Data from 4A	1.7	1.48
5	1.7	1.72			1.71	1.9
6	Data from 5	Data from 5			1.71	1.9
7	1.65	1.6			1.62	1.78
8A	1.74	1.93			1.84	1.15
8B	Data from 8A	Data from 8A			1.74	1.15
9	1.46	1.72	1.57	1.52	1.57	1.06
10	1.74	1.91			1.74	1.15
11	1.44	1.94			1.69	1.06
12	1.67	1.74			1.7	1.76

Table 2.1 Differences in Calculated and Measured CTEs.

The calculated and measured average CTEs are summarized in Table 2.1. The measured CTEs shown are the average CTEs over the temperature range, which are the slope of the linear least squares regression of the strain versus temperature. All values have been normalized by the CTE of the components.

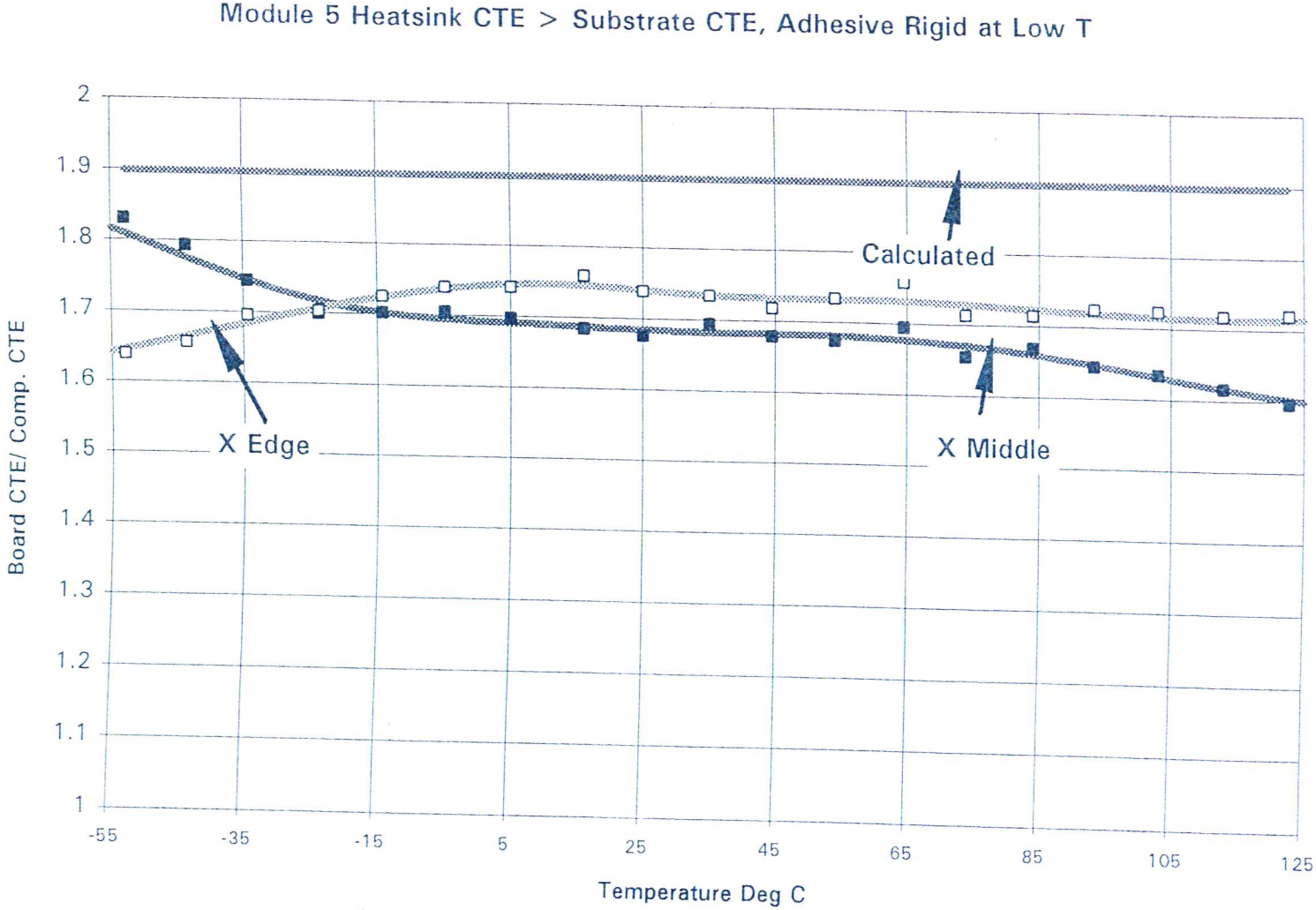


Figure 2.4 CTE Measurements for Heatsink CTE > Substrate CTE

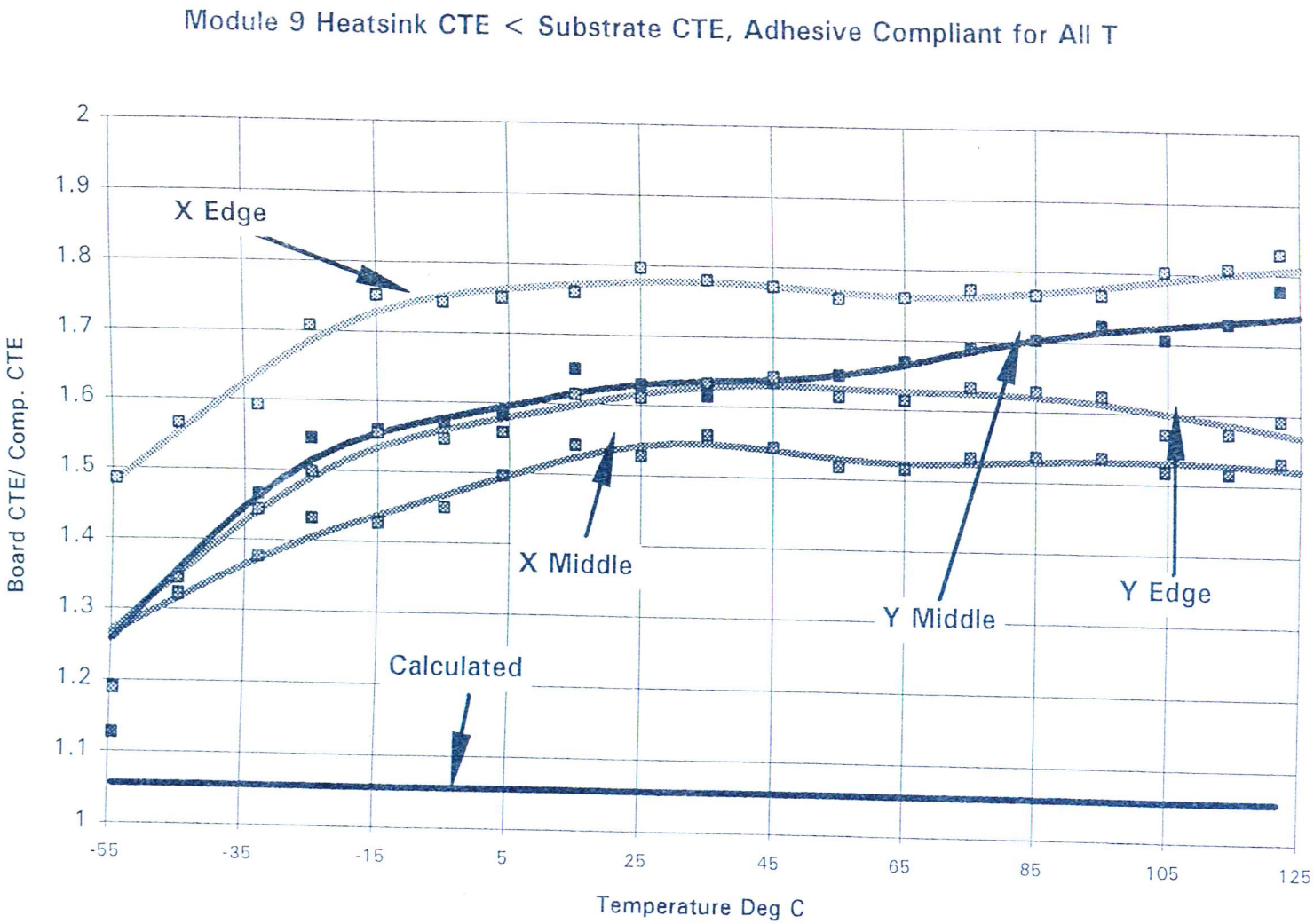


Figure 2.5 CTE Measurements for Heatsink CTE < Substrate CTE

3. Statistical Evaluation of Test Results

Once the parametric-accelerated test is completed, it is necessary to comprehensively analyze the failure data using rigorous statistical analysis because of large scatter in the test data. In addition, it is necessary to assess the effect of the critical variables on the accelerated test and how they affect the life of the electronics device. Physics-of-failure methodology is combined with statistical evaluations to assess the influence of these critical variables.

3.1 Weibull Statistical Probability Distribution

In typical engineering application; traditional reliability analysis of electronics involves assessment of the mean-time-to-failure (MTTF) and mean-time-between-failure (MTBF) based on a constant failure rate assuming an exponentially distributed probability of failure. This model cannot capture initial failure free periods typical of wearout failures in electronic interconnects, and is usually based on empirical models fitted to field data where the root causes of failures are ignored. In designing, qualifying or strengthening a new product or an existing product with new technologies, these models are sometimes inappropriate and misleading because they are not derived from or based on physics or mechanics of real failure [10], and as such, they do not give us insight into or control over actual failure mechanisms. A survey of commonly occurring failure mechanisms reveals that power-law relationships are more appropriate than exponential relationships for formulating

models. It is noteworthy that the Weibull distribution was originally derived by assuming a power-law relationship for the hazard rate. For example, crack propagation for brittle materials according to the Griffith Crack Theory relates the applied stress to the stress at the crack according to a power-law relationship ($\sigma_{max} = k\sigma(l/r)^{0.5}$, where l and r represent dimensions of the crack) [11]. Miner's Rule relates cumulative fatigue damage due to n applications of the applied stress by a power-law relationship ($D = n\sigma^b$, where b represents a material property) [12]. A similar power-law relationship is used in this study to model the accumulation of creep-fatigue wearout damage in solder joints. Probability of failure is expressed by a three-parameter Weibull distribution.

The cumulative probability of failure, P(t), is defined as:

$$P(t) = \frac{k}{n+1}, \quad k = 1 \ldots n \tag{3.1}$$

where k represents the failure number and n is the sample size. The experimentally obtained cumulative probability of failure represented with a three-parameter Weibull distribution:

$$P(t) = 1 - \exp^{-[(t - t_0)/\theta]^B} \quad \text{for } t > t_0$$
$$0 \quad \text{for } t < t_0 \tag{3.2}$$

where t_0, B and θ are the location, scale, and slope parameters, respectively. The two parameter Weibull assumes that the location parameter is zero, which means that at a time corresponding to zero thermal cycles, the probability of failure is zero. It has been shown that the three-parameter Weibull has a higher correlation coefficient than the two

parameter Weibull or a Log-Normal distribution because of its ability to capture the initial failure-free period [13]. Note that when B = 1 and when $t_0 = 0$, the Weibull distribution reduces to the Exponential distribution (constant hazard rate). Equation (2), for $t > t_0$, can be solved for B explicitly as shown in Equation (3.3)

$$B = \frac{\log_{10}\ln(1 - P(t))^{-1}}{\log_{10}(t - t_0) - \log_{10}\theta} \qquad 3.3$$

The numerator of Equation (3.3) is the reduced variate $y = \log_{10}\ln[1 - P(t)]^{-1}$, and the lead term of the denominator of Equation (3.3) is the reduced variate $x = \log_{10}(t - t_0)$. When assumed to be non-zero, t_0 must be adjusted so that the data will fall on a straight line when plotted against the reduced x and y variates. The scale parameter, θ, is also termed the characteristic life, which is the time when 63.2% of the population will have failed. The slope parameter, B, is the slope of the best fit line when the data is plotted in terms of the reduced x and y variates [14].

The hazard rate, h(t), for a Weibull distribution is defined as the probability density divided by the reliability.

$$h(t) = \frac{dP(t)}{dt}\frac{1}{1-P(t)} = \frac{\frac{B}{\theta}\left(\frac{t - t_0}{\theta}\right)^{B-1} e^{-[(t - t_0)/\theta]^B}}{e^{-[(t - t_0)/\theta]^B}} \qquad 3.4$$

$$h(t) = \frac{B}{\theta}\left(\frac{t - t_0}{\theta}\right)^{B-1} \qquad 3.5$$

The measured P(t) and h(t) help assess the failure mechanisms and the acceleration transforms.

3.2 Statistical Evaluation of Mechanism, Site and Mode of Failure

Cyclic fatigue can induce damage in solder joints by causing grain boundary coarsening and sliding resulting in void growth between the interfaces of the grain. Eventually, these voids either grow or coalesce resulting in solder joint cracks which create open circuits causing the circuit to malfunction.

Two types of failures occurred while performing the accelerated test, which are identified and distinguished as follows. Solder joint fatigue failures are typically expected to occur first on larger components, where the shear stress due to the coefficient of thermal expansion mismatch between the substrate and the component is greatest. However, in this test the first failures occurred in the smaller 32-pin LCCs very early, within 200 elapsed thermal cycles. Because these failures were detected at a very early stage of the testing, and on the smaller components, further investigation was necessary. Weibull hazard rate plots of these early failures, shown in Figure 3.2, revealed that these failures follow a decreasing hazard rate, which is consistent with an infant mortality trend. Solder joint failures which occur due to accelerated testing are not expected to follow an infant mortality failure trend. Instead they should show an increasing hazard rate, consistent with a wear-out failure mechanism.

The temperature and the time of each resistance spike is plotted against the thermal cycle to gain further insight into the mechanism of failure for each of the early failures. As shown in Figure 3.3, these early failures on the 32-pin LCCs always occurred during the transition from

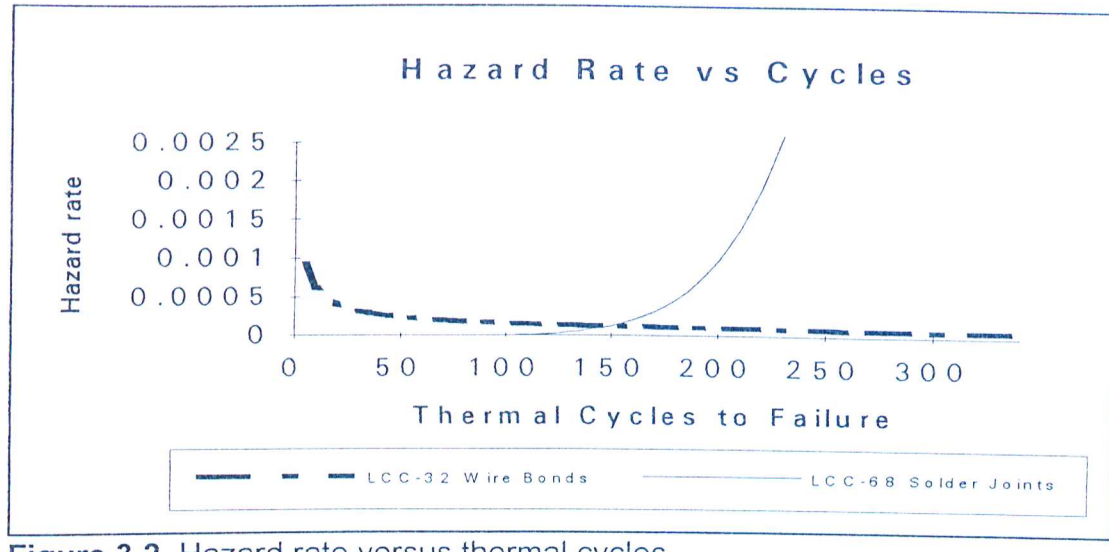


Figure 3.2. Hazard rate versus thermal cycles showing wire-bond and solder joint failures

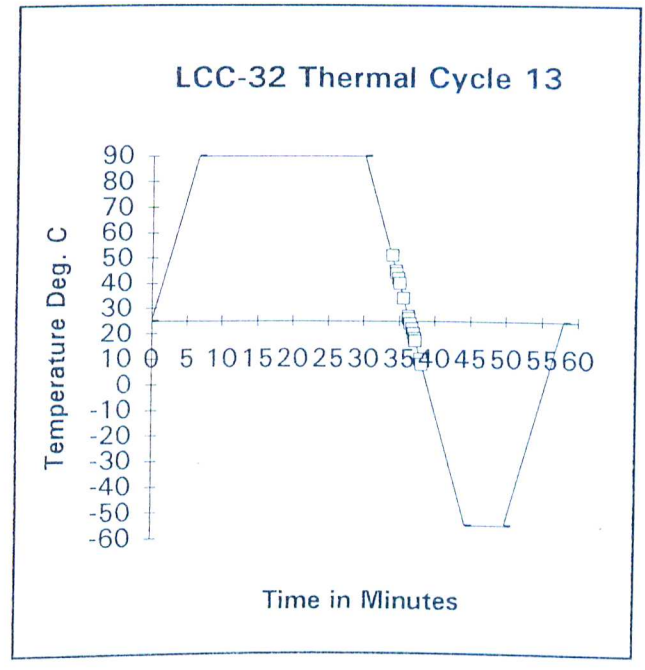


Figure 3.3. Wire-bond failure plotted against thermal cycles.

high to low temperature, and consistently occurred catastrophically, with a small time interval between the first and the fifteenth resistance spike on each circuit. Typically, in solder joint failure there is no such pattern regarding the part of the cycle where failure will occur, and

there is a longer time gap between crack initiation and propagation to final failure. According to Frear et al. [15], wear-out mechanisms in solder joints include microstructural coarsening and deformations due to plastic flow and creep, followed by crack initiation and growth, and crack propagation or coalescence through the solder joints [15]. Final wearout failure occurs when damage accumulates beyond the endurance threshold of the solder joint. The process of a crack evolving into an open circuit often takes several hours or several cycles of accelerated testing. The premature failure, the decreasing hazard rate, the fact that the failures on the smaller components consistently occurred during transition from high to low temperature, and the small interval of time between the first and fifteenth resistance spikes all led to the conclusion that these were not solder joint failures. Failure root-cause analysis at 340 thermal cycles consisting of delidding and visual inspection under 30X magnification confirmed that these early failures on the smaller components were wire-bond failures. Since the target of this test program was solder joint fatigue, these wire-bonds were repaired and returned to test. Fatigue failure of solder joints, as expected, began to occur later, beginning with the larger components first and then continuing on the smaller components. The two observed failure types are classified in Table 3.1.

Failure Type 1	
Mode	Change in resistance-open circuit
Load	Transition from high to low temperature
Site	Wire bonds on smaller 32-pin LCCs
Mechanism	Wire bond debonding due to shear stress
Failure Type 2	
Mode	Change in resistance-open circuit
Load	Thermal cycling
Site	Solder joint fracture
Mechanism	Interaction between low-cycle fatigue and creep

Table 3.1 Classification of wire-bond and solder joint failure.

3.3 Acceleration Transform Based on a Bayesian Approach

The experimental data is analyzed using the Weibull statistical distribution described in Section 3.1. The cycles to failure at a given percent probability of failure are computed from the maximum-likelihood distribution parameters. However, in order to measure the uncertainty in determining these parameters, a more rigorous statistical method is necessary. These parameters are evaluated using a Bayesian approach. [16,17]

The maximum likelihood estimates of the two parameter Weibull distribution provide the maximum-likelihood that when these parameters are used, the failure data will fall as closely as possible to the distribution within a degree of uncertainty. This degree of uncertainty is of paramount importance when attempting to estimate fatigue life. In many cases an investigator may blindly compute probability distributions without determining how accurately the distributions fit the actual data. In these cases, outliers are eliminated from the failure data without sufficient justification. The Bayesian statistical approach provides a systematic method for computing probability distributions and determining which data is contaminating the distributions. Failure analysis can then be used to confirm if there is a good reason for eliminating the outliers.

The maximum-likelihood estimators have desirable properties for large samples, and these estimators become more precise as additional data becomes available. Therefore when using relatively small sample sizes, as is true for this study, the uncertainty of the true

parameters becomes a major concern. Other techniques such as sample theory methods measure the uncertainty in terms of the sampling distribution of the estimators of the parameters. Unfortunately, when using sampling theory it is practically impossible to obtain the joint distribution of the maximum-likelihood estimates for both of the Weibull parameters simultaneously. The Bayesian approach does provide a method to obtain confidence contours on both parameters of the Weibull distribution. The confidence contours also provide a quantitative method to recognize and eliminate outliers. In this study, prior knowledge of the distribution parameters is not assumed. Assuming no prior knowledge of the distribution parameters is a conservative approach. However, in cases of relatively small sample size, existing data suggests a less conservative approach. [18]

The two-parameter Weibull distribution for $t > 0$ is obtained from Equation 3.2 as:

$$P(t) = 1 - \exp^{-[t/\theta]^B} \qquad 3.6$$

For this distribution, the mean time to failure (MTTF) is:

$$MTTF = \theta\Gamma(1 + 1/B) \qquad 3.7$$

where Γ is the gamma function.

The probability density for the two-parameter Weibull distribution is:

$$p(t) = \int_{-\infty}^{t} P(x)dx = \frac{B}{\theta^B} t^{B-1} \exp^{-[t/\theta]^B} \qquad 3.8$$

There are n failures from the population occurring at times X_1, X_2, $X_3 \ldots X_n$, and d samples have not failed at the end of the test at time T. The joint probability for n failures and d censored data is proportional to the conditional likelihood, P, of the data on the distribution parameters P(Data|θ, B).

$$P(Data|\theta, B) \propto f(X_1)dx\, f(X_2)dx\, f(X_3)dx \ldots f(X_n)(1-F(T))^d \qquad 3.9$$

From Equation (3.8) this reduces to:

$$P(Data|\theta, B) \propto \frac{B^n}{\theta^{nB}}\left[\prod_{i=1}^{n} X_i\right]^{B-1} \exp\left[-\theta^{B-1}\left[dT + \sum_{i=1}^{n} X_i\right]^B\right] \qquad 3.10$$

If we assume a prior probability density $\pi_o(\theta, B)$ the posterior density , π, is

$$\pi(\theta, B|Data) \propto P(Data|\theta, B)\pi_o(\theta, B) \qquad 3.11$$

The posterior density is normalized by the numerical integral of the posterior density by integrating θ from zero to infinity. Further, if a constant prior density is assumed we get:

$$\pi(B|Data) \propto \pi_o \int_0^\infty P(Data|\theta, B)d\theta \qquad 3.12$$

After some work, this becomes:

$$\pi(B|Data) \propto \frac{\Gamma(n+1/B)}{B\left(dT^B + \sum_{i=1}^{n} X_i^B\right)^{1/B}} \prod_{i=1}^{n}\left[\frac{BX_i^{B-1}}{dT^B + \sum_{i=1}^{n} X_i^B}\right] \qquad 3.13$$

Equation (3.13) is then normalized by the numerical integral of the right hand side. This gives the marginal posterior density of the Weibull slope parameter, B. However, our goal is to obtain the posterior density of both parameters based on a constant prior density. This is obtained directly from Equation (3.10) by normalizing by the numerical integral of the right hand side of the equation to obtain:

$$P(\theta, B|Data) = \frac{\frac{B^n}{\theta^{nB}}\left[\prod_{i=1}^{n} X_i\right]^{B-1} \exp\left[-\theta^{B-1}\left[dT + \sum_{i=1}^{n} X_i\right]^B\right]}{\int_{\theta=0}^{\infty}\int_{B=0}^{\infty} \frac{B^n}{\theta^{nB}}\left[\prod_{i=1}^{n} X_i\right]^{B-1} \exp\left[-\theta^{B-1}\left[dT + \sum_{i=1}^{n} X_i\right]^B\right] dB\, d\theta} \qquad 3.14$$

A typical three dimensional plot of Equation (3.14) is shown in Figure 3.4. The total

volume under the plot is equal to unity due to the normalization. The algorithm to compute confidence contours at any percent confidence is given in Appendix F.

The experimental failure data is separated into twelve groups based on shear strain range $\Delta\gamma$, estimated as [19]:

$$\Delta\gamma = \frac{\Delta\alpha\Delta T L_4}{2h} \qquad 3.15$$

The failure data grouped according to strain range is given in Appendix E. Confidence contours at of 95%, 90%, 50%, and 5% for the twelve different groups are shown in Appendix G. The maximum-likelihood estimates of B and θ occur at the peak of Figure 3.4.

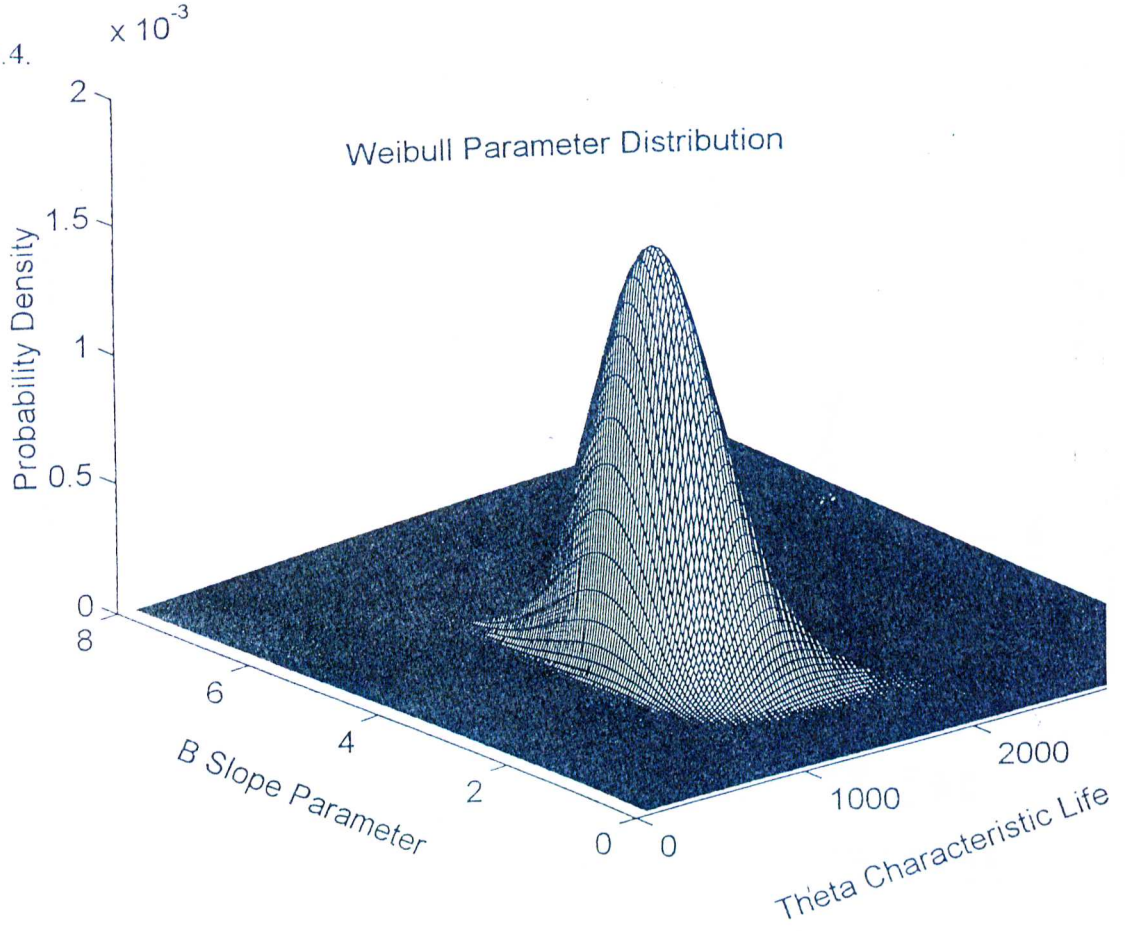
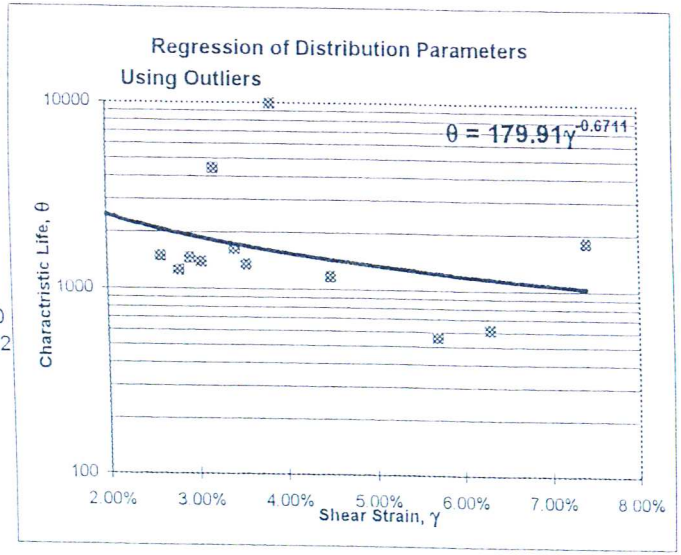
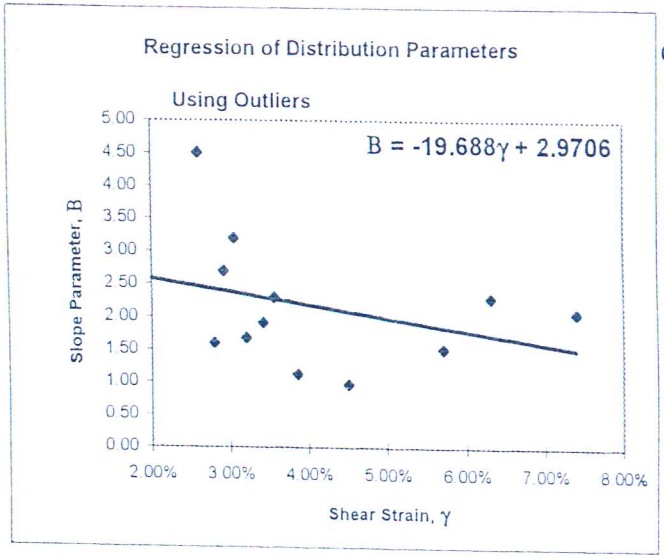


Figure 3.4 Three-Dimensional Weibull posterior Density

Using All Data

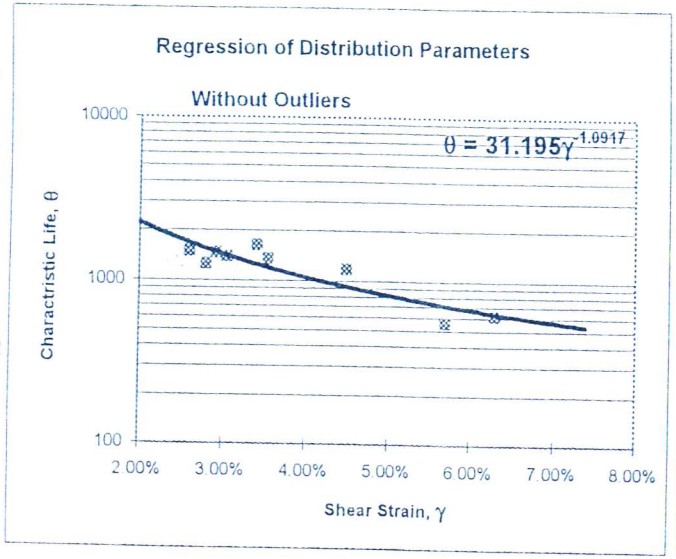
%γ	B	θ	Group
2.00%			1
2.60%	4.51	1494	2
2.80%	1.60	1256	3
2.92%	2.70	1460	4
3.05%	3.20	1387	5
3.20%	1.68	4430	6
3.42%	1.92	1630	7
3.55%	2.31	1348	8
3.85%	1.14	9901	9 & 10
4.50%	0.98	1171	11 & 12
5.70%	1.53	557	13
6.30%	2.31	616	14
7.40%	2.07	1815	15





Getting Rid of Outlayers

%γ	B	θ	Group
2.00%			1
2.60%		1494	2
2.80%	1.60	1256	3
2.92%	2.70	1460	4
3.05%	3.20	1387	5
3.20%	1.68		6
3.42%	1.92	1630	7
3.55%	2.31	1348	8
3.85%	1.14		9 & 10
4.50%	0.98	1171	11 & 12
5.70%	1.53	557	13
6.30%	2.31	616	14
7.40%	2.07		15



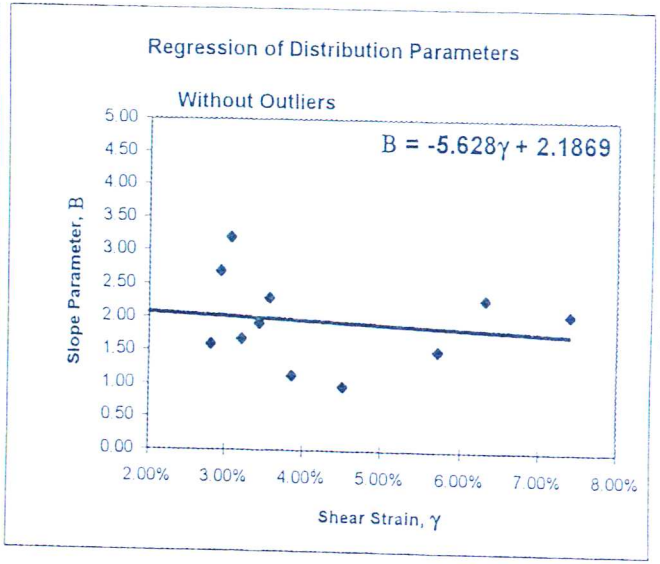


Figure 3.5 Elimination of Outliers Based on Confidence Contours

When the posterior parameter density plot is sharp, as shown in Figure 3.4, there is good confidence in the calculated distribution parameters. When this plot is flat, there is little confidence in the parameters. This lack of confidence is due to small sample size, much of the data being censored, and the fact that a conservative flat prior distribution is assumed. All three of these effects are interrelated. As seen in Appendix G, the 95% confidence contour for B at 2.60% strain can range from 2.0 to 9.0. This shows that there is little confidence in this calculation for the maximum-likelihood estimate of B, but there is much confidence in the calculation for θ. Blindly fitting the Weibull distribution to the failure data without examining the confidence on the distribution parameters may not have led to this conclusion. Similarly, the confidence contours on θ for 3.20, 3.85, and 7.40% strain show that there is little confidence in the maximum-likelihood estimates of θ for these strain levels. Based on these observations, these values of B and θ are eliminated from the data as shown in Figure 3.5

Now that the maximum-likelihood estimates of the distribution parameters are determined at different strain levels, the final step in obtaining a physics-of-failure acceleration transform is to relate these parameters to the critical variables. The strain is related to θ by a power law relationship, and the strain is related to B by a linear regression. This fitting of the distribution parameters to the strain is shown in Figure 3.5 at the top using all of the distribution parameters and in the bottom of Figure 3.5 the outliers discussed above are eliminated from the data. There is a dramatic change in the results when eliminating the outliers from the data, and all of the uncontaminated data shows a consistent trend.

Note that slope parameter, B, remains essentially constant when the outliers are eliminated. The time to failure based on X percent probability of failure as a function of strain is computed using the following relation:

$$X\% = 1 - \exp^{-[N_f(X\%)/\theta]^B} \qquad 3.16$$

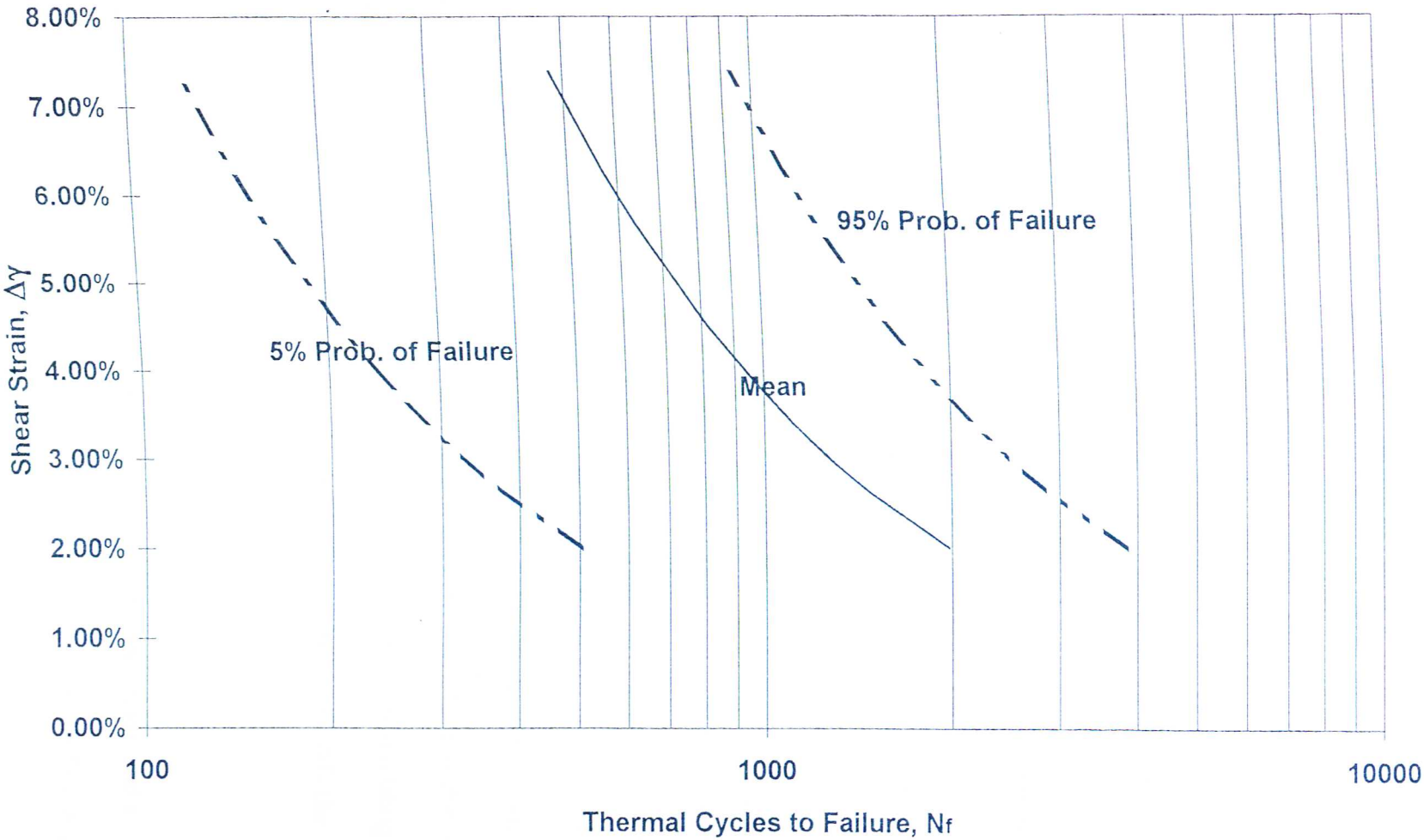
Rearranging Equation (3.16) and simplifying gives

$$N_f(X\%) = \theta[-\ln(1 - X\%)]^{1/B} \qquad 3.17$$

where $\theta = 31.195\dot{\gamma}^{-1.0917}$ and B = 2.0 as shown in Figure 3.5 Note that θ is dependent on strain. The reason for this dependence will be discussed in Section 4.1.

Figure 3.6 shows the acceleration transform model based on the Bayesian statistical approach as calculated from Equation (3.17). Note that this acceleration transform model is based on strain and not temperature. The temperature can be back calculated from each strain level by Equation (3.15).

Figure 3.6 Acceleration Transform Based on a Bayesian Statistical Approach



4. Physics-of-Failure Evaluation of Test Results

One of the goals of this study is to obtain qualitative assessment of the damage caused in the LCC solder joint during thermal cycling. Another goal is to extract information regarding the acceleration transform from the test described in Section 2. To maximize the information extracted from the experiment for more accurate acceleration transforms, the effect of critical variables (such as component size and module CTE) on the solder joint stresses is estimated from physics-of-failure models. In order to correctly evaluate any accelerated test, it is necessary not only to define the critical variables, but also to quantify the effect of these variables in laboratory as well as in the field conditions. The Bayesian statistical approach as it is presented in the previous section is used for eliminating the outliers from the failure data in order to achieve a more dependable database which can be used accurately with physics-of-failure models to obtain acceleration transforms. By estimating the total shear strain and then determining the dependence of the distribution parameters on the strain range, it is possible to obtain a hybrid analytical-empirical acceleration transform model based on the statistical evaluation of the empirical results. Alternatively, it is possible to obtain a purely analytical acceleration transform using only physics-of-failure modeling. In both situations, the test data serves to verify the accuracy of the models or modify the models for more accurate acceleration transforms for future studies.

A physics-of-failure model consists of two crucial parts, a stress analysis model and a damage model. The stress analysis is used to compute the state of stress at the failure site,

as a result of environmental loads. In this example, we are interested in the history of mechanical stress and strain in the solder joint caused by the global temperature changes. Typically this involves solving a boundary value which depends on the critical variables such as the differential thermal expansion, the size of the components, and the geometry of the solder joint. The damage model relates the amount of stress to time to failure based on each failure mechanism.

4.1 Physics-of-Failure Models Considered

In this study two physics-of-failure models, namely the IPC model [19] and the CALCE energy partitioning model [25], are used to comparatively evaluate the accelerated test results. The IPC model makes several simplifying assumptions to enable closed form stress analysis. The CALCE energy partitioning model requires more detailed inputs which normally require nonlinear viscoplastic stress analysis.

4.1.1 IPC Physics-of-Failure Model

The fifteen modules are separated into five groups determined by CTE in order to obtain the acceleration transforms. All of the modules in each group have approximately the same CTE. In addition to the CTEs of the modules, an additional experimental parameter is the component size. The failure data is separated into 15 groups because there are three different component sizes and five different calculated effective module CTEs. For simplicity, other variables such as solder joint geometry and temperature distribution are assumed to be nominally uniform for all of the components. In addition, the thermal expansion coefficient is assumed to be uniform across each module. Due to the differential thermal expansion between the board and component, the magnitude of the stresses is different for each combination of module CTE and component size. Thus, there is a wealth of information available from a single test.

The influence of each critical variable on the stress magnitude is modeled with simple closed-

form stress analysis and combined with a single power-law damage model. The physics-of-failure model proposed by Engelmaier and recommended by IPC SM-785 [19] for solder joint fatigue provides a first order approximation to estimate the thermal cycles to failure as a function of percent probability of failure. This model makes use of a modified Coffin-Manson low cycle fatigue equation [20] developed for more typical elastic-plastic engineering metals which relates strain range to time to failure by a power law. Because of the time dependent viscoplastic stress-relaxation and creep behavior of solder, the Coffin-Manson equation requires modification to a more general relationship proposed by Morrow [21]. Furthermore, based on empirical data [22], the fatigue ductility exponent is expressed as a function of temperature and time. This type of functional relationship is sometimes used as an attempt to quantify the effects of creep and stress relaxation on fatigue damage. The model for determining the cycles to failure, N_f, for leadless surface-mount solder joints undergoing accelerated thermal cycling is [19]:

$$N_f(x\%) = \frac{1}{2}\left[\frac{F}{2\varepsilon_f}\frac{L_d \Delta\alpha\Delta T}{h}\right]^{\frac{1}{c}}\left[\frac{\ln(1 - 0.01x)}{\ln(0.5)}\right]^{\frac{1}{B}} \qquad 4.1$$

where the fatigue ductility exponent, c, is

$$c = -0.422 - 6X10^{-4}T_{sj} + 1.74X10^{-2}\ln\left(1 + \frac{360}{t_d}\right) \qquad 4.2$$

and where

ε_f fatigue ductility coefficient, $2\varepsilon_f \cong 0.65$ for near-eutectic tin-lead solder.

F empirical "non-ideal" factor accounting for non-ideal solder joint geometry, larger solder fillets, Pb rich boundary layers, etc... For leadless chip carriers, $1.2 > F > 0.7$. For this analysis F = 1.

h solder joint height. h is the distance from the substrate to the bottom of a component, h = 6.5 mils in the present study.

L_d maximum diagonal distance between solder joints for each component.

$\Delta\alpha$ absolute difference in coefficients of thermal expansion of the ceramic components and the substrate. $\Delta\alpha$ ranges from 0.5 ppm/ °C to 5 ppm/ °C in this study.

ΔT cyclic temperature swing, which can account for the internal heating of components due to power dissipation effects as well as external temperature variations. Because the components were not powered up, ΔT = 145 °C in this study.

T_{sj} mean cyclic solder joint temperature. Because the components were not powered up, this temperature is the average temperature due to the thermal cycle. T_{sj} = 40 °C.

t_d dwell time in minutes. Because more stress relaxation occurred during the longer 23.5 minute dwell at 90 °C as shown in Figure 3, t_d = 23.5 minutes.

B Weibull slope parameter. B = 4.0 for LCCs [23].

c for this study c = -0.417 from Equation 4.2.

Equation (4.1) combines a low-cycle fatigue model with simplified stress analysis, and has been experimentally validated for temperatures greater than 20 °C. Note that the component size (L_d), the CTE mismatch between the PCB and the component ($\Delta\alpha$), and the cyclic temperature range (ΔT) are all explicit parameters in this model, and hence their effects on solder joint stresses can be quantitatively assessed. This stress analysis ignores the local CTE mismatch at the solder pads on the substrate and the component, and assumes complete stress relaxation during the dwells at high as well as low temperatures. Due to the fact that the mean cyclic

temperature and dwell time remain constant, the fatigue ductility exponent, c, remains constant for each combination of module and component. The cycles to failure for each combination of module and component is computed relative to an arbitrary reference configuration according to Equation (4.1).

$$(N_f)_{ref} = \frac{1}{2}\left[\frac{F}{2\varepsilon_f}\frac{(L_d)_{ref}\,\Delta\alpha_{ref}\,\Delta T_{eff}}{h}\right]^{\frac{1}{c}} \qquad 4.3$$

Equation (4.3) relates the cycles to failure to an effective cyclic temperature range, ΔT_{eff} which would cause failure if each combination of module and component had the same critical variables (L_d and $\Delta\alpha$) as the reference configuration. The cycles to failure determined by the actual critical variables for each combination of module and component is equated with the cycles to failure given by Equation (4.3).

$$\frac{1}{2}\left[\frac{F}{2\varepsilon_f}\frac{(L_d)_{ref}\,\Delta\alpha_{ref}\,\Delta T_{eff}}{h}\right]^{\frac{1}{c}} = \frac{1}{2}\left[\frac{F}{2\varepsilon_f}\frac{L_d\,\Delta\alpha\Delta T_{test}}{h}\right]^{\frac{1}{c}}$$

Simplification and rearrangement gives:

$$\Delta T_{eff} = \left[\frac{L_d\,\Delta\alpha}{(L_d)_{ref}\,\Delta\alpha_{ref}}\right]\Delta T_{test} \qquad 4.4$$

Because the stress levels are different for each combination of component and module, the physics-of-failure model allows us to compute fifteen different values for ΔT_{eff} from the ΔT_{test}. In summary, Equation (4.4) is an expression of an effective cyclic temperature range which would have produced failure in the reference configuration, in the same number of cycles observed on each configuration for the actual cyclic temperature range used in the test.

Equation (4.4) is used later in this study to compute acceleration transform using this physics-of-

failure model. This physics-of-failure model along with the experimental data is used to estimate the effect of the size of the components and module materials on the stresses in the solder joints. When assessing the effect of the component size on the stresses, Equation (4.1) is solved for each module and each component at 50% probability of failure. Then, a reference module is chosen and the cycles to failure given by Equation (4.1) is used to normalize the failure data with respect to the reference module. The experimental data relative to the reference module is separated into three groups determined by component size, and three-parameter Weibull distributions of the three different size components are shown in Figure 4.1a as if they had been mounted on the reference module. This method of estimating the effect of the stresses is used, as opposed to lumping together all of the failure data for each of the component sizes regardless of the module on which they are mounted, because it eliminates the influences of the stresses due to the different module materials on the statistical distributions. The reference module for this study is chosen to be a glass/polyimide substrate with CIC foils on an aluminum heatsink. In a similar manner, the effect of the substrate material, heatsink material, and adhesive used to attach the substrate to the heatsink on the stresses is assessed by normalizing the failure data relative to a reference component (32-pin LCC in this example) and separating the experimental data into five groups determined by module CTE, as shown in Figure 4.1c.

In order to quantify the effect of the CTE variation across the modules on the experimental results, the stress levels for each component and module combination are determined relative to a reference configuration by using Equation (4.1), and the experimental data is normalized with respect to these stresses. The failure data is then separated into two groups determined by component placement on the PCB (center and edge). The center components are labeled 32-7, 32-8, 32-9, and 48-2 in Figure

2.1. By eliminating the effect of the module CTE and component size on the stresses, it is clear from Figure 4.1b that the components located closer to the center of the module are less likely to fail than the components near the edge. This is due to the non-uniformity of CTE distribution discussed in Section 2.4 can affect the transform since the physics-of-failure model assumes that same size components on all similar modules undergo similar fatigue due to the same differential thermal expansion regardless of the location of the components on the modules.

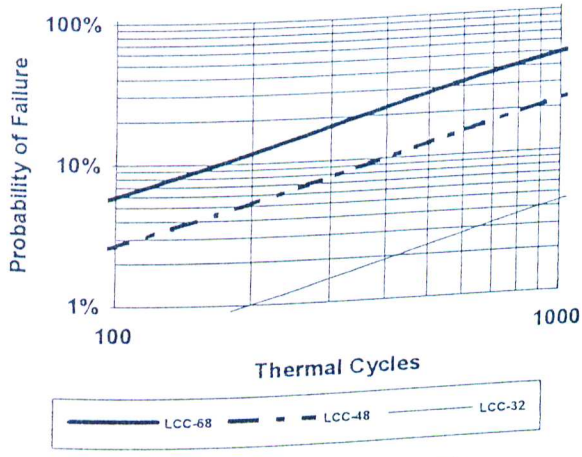


Figure 4.1a Effect of Component Size on Probability of Failure

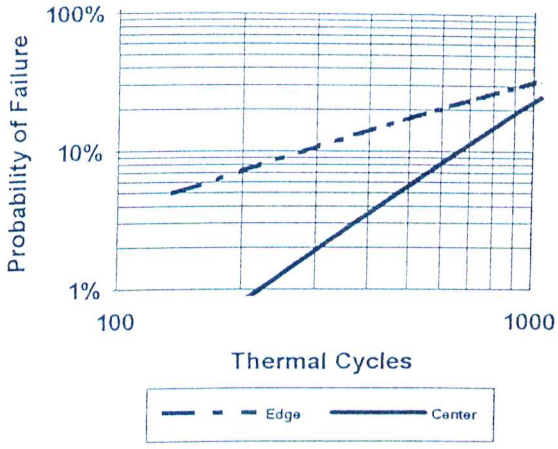


Figure 4.1b Effect of Component Placement on Probability of Failure

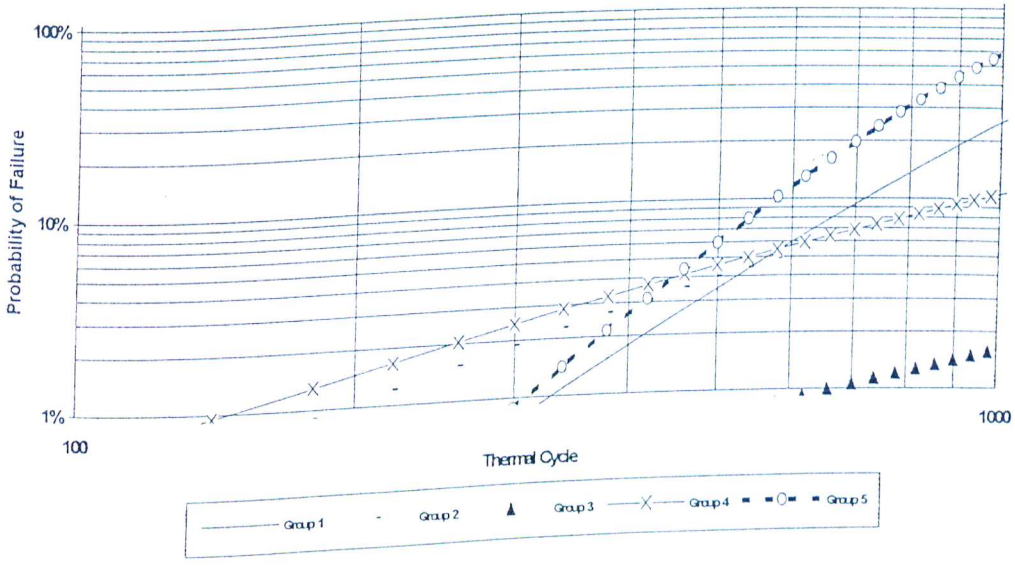


Figure 4.1c Effect of Module Material Probability of Failure

4.1.2 CALCE Energy Partitioning Damage Model

As discussed in the previous section Engelmaier attempts to obtain a closed form physics-of-failure model by simplification of the Manson-Coffin equation through relating the shear strain amplitude to the fatigue life by a one term relationship. This relationship , although easy to apply and quick to yield results, includes assumptions which may not be completely acceptable. A different damage model is proposed by Manson et al. [24], for creep-fatigue interactions. This model uses a strain range partitioning technique where creep and plastic strains are recorded separately and the damage due to each mechanism is evaluated independently. The total damage is the sum of the damage from the individual mechanisms. In fact, the strain range partitioning considers the damage due to (i) completely reversed plasticity, (ii) tensile plasticity reversed by compressive creep, (iii) tensile creep reversed by compressive plasticity, and (iv) completely reversed creep. Each of these components is related to damage by a Coffin Manson type power law and the total damage and thus the time to failure is determined by superposition. However, implementation of this damage model using finite element stress analysis requires maintaining a state of constant stress during creep straining, which is difficult to simulate in a CTE mismatch problem.

An alternative to the strain-range partitioning approach for separating the damage due to the different fatigue mechanisms is the CALCE energy partitioning damage model.[25] In this proposed approach, the energy dissipated for each thermal cycle is partitioned into the

elastic strain energy density, U_e, the plastic work density dissipated per cycle, W_p, and the creep work density dissipated per cycle, W_c. Each of the components of energy is then related to time to failure by Coffin-Manson type power laws as follows:

$$U = U_e + W_p + W_c = U_{e0} N_{fe}^{\ b'} + W_{p0} N_{fp}^{\ c'} + W_{c0} N_{fc}^{\ d'} \qquad 4.1$$

where

$$U_e = U_{e0} N_{fe}^{\ b'} \cong \frac{1}{2}\sigma\varepsilon,\ W_p = W_{p0} N_{fp}^{\ c'} = \int \sigma d\varepsilon_p, and\ W_c = W_{c0} N_{fc}^{\ d'} = \int \sigma \dot{\varepsilon}_c dt \qquad 4.2$$

The fatigue constants U_{eo}, b', W_{po}, c', W_{co}, and d' are determined from experimental data taken from various investigators [26].

Fatigue Constants for Pb/Sn Solder	
b'	-0.18
c'	-0.6
d'	-1.16
Ueo	0.698 Mpa/cycle^b'
Wpo	165 Mpa/cycle^c'
Wco	143 Mpa/cycle^d'

Table 4.1 Fatigue Constants ([26] 1993)

As shown in Table 4.1, the fatigue constants and thus the time to failure can vary significantly depending on the damage mechanism. The damage due to the elastic, plastic, and creep energy density dissipated is $D_e=1/N_{fe}$, $D_p=1/N_{fp}$, and $D_c=1/N_{fc}$, respectively. The total damage , D_T, is computed by using Miner's postulate for superposition of damage.

$$D_T = D_e + D_p + D_c = \frac{N_{fe} N_{fp} N_{fc}}{N_{fe} N_{fp} + N_{fp} N_{fc} + N_{fe} N_{fc}} \qquad 4.3$$

The energy terms U_e, W_p, and W_c are typically computed from viscoplastic FEM analysis. The cycles to failure for each mechanism N_{fe}, N_{fp}, and N_{fc} are then obtained by using the fatigue constants given in Table 4.1. The advantage of using this type of physics-of-failure model over the IPC model is that (i) there are no assumptions about the load history , or the amount of stress relaxation, (ii) damage due to the different mechanisms (elasticity, plasticity, and creep) can be addressed separately instead of lumping them into a single term, and (iii) the local and global CTE mismatches can be addressed in a unified manner. The advantage of energy partitioning over strain range partitioning is that the loads are easy to simulate since they are not constant during the dwells. There is a wealth of experimental data from which the fatigue constants in Table 4.1 can be determined for each mechanism.

4.2. Stress Analysis

As discussed in Section 4.1, the CALCE Energy Partitioning model requires a detailed viscoplastic FEM analysis. The details of this stress analysis are presented here.

4.2.1 Constitutive models

In order to model the viscoplastic response of solder, it is necessary to comprehensively evaluate the constitutive models which are used to simulate the material response using FEM.

Plastic deformation, as defined in this study, are "instantaneous" inelastic deformations which occur when the stress exceeds the yield stress. The constitutive model for the elastic-plastic response of solder is given by a power-law hardening Ramberg-Osgood model

$$\varepsilon = \varepsilon_e + \varepsilon_p = \frac{\sigma}{E} + \left(\frac{\sigma}{K}\right)^{1/n_p} \qquad 4.8$$

where ε is the equivalent mechanical strain, E is the elastic modulus, σ is the equivalent (von Mises) stress, K is the strength coefficient, and n_p is the plastic strain hardening exponent. It is assumed that plasticity and creep are independent and therefore, the strength coefficient and strain hardening exponent should be independent of creep. It is therefore desirable to obtain these material properties from experiments conducted at high strain rates such that they are unaffected by any creep mechanisms. The values which have been used in previous studies (K = 48.44 MPa and n_p = 0.0565 [25,26]) have been taken from experimental data obtained at temperatures of 20 °C, at strain rates of

0.002/sec. At this relatively low strain rate it is possible that creep may have allowed the stresses to relax, resulting in a flatter stress strain response and thus a low plastic exponent. In order to remedy this situation, experimental data at high strain rates is used to determine the plastic material properties. In addition the yield stress is temperature dependent. The temperature dependent plastic material properties used in this study are given in Table 4.2. The experimental data along with the regressions to determine these material properties is shown in Appendix H. The plastic properties used in this study are taken from the experimental data at strain rates of 0.1/sec as shown in the last three rows of Table 4.2.

Temp C	σy MPa	ε /sec	K MPA	nc
-40	29.9	0.001	49.16	0.105
-40	29.9	0.01	40.15	0.142
-40	29.9	0.1	38.85	0.15
20	29.1	0.1	40.27	0.057
80	17.4	0.1	27.76	0.066

Table 4.2 Plastic Material Properties

Creep, as defined in this study, is temperature-time dependent plastic deformations which may occur even though the applied stress may be less than the yield strength. Stress relaxation occurs when the strain is held constant and viscous flow occurs. Since the dimensions are fixed due to the constant strain, the viscous flow allows the stress to be reduced or relaxed. Strictly speaking, creep and stress relaxation are defined by changes in different state variables, however, they can be modeled to occur simultaneously.

It is now well established that steady state creep deformation of metals can be expressed by the general Dorn Equation

$$\frac{\dot{\varepsilon}_c kT}{D\mu b} = A\left(\frac{\sigma}{\mu}\right)^{n_c}\left(\frac{b}{d}\right)^{p} \qquad 4.9$$

where ε_C is the creep strain rate, D the diffusion coefficient, μ the shear modulus, b the Burger's vector, d the grain size (or interphase spacing), σ the applied stress (usually shear), k is Boltzman's constant, and A, n_c and p are material constants. The diffusion coefficient is given by an Arrhenius equation:

$$D = D_o e^{-\frac{\Delta H}{kT}} \qquad 4.10$$

The diffusion coefficient, activation energy, and the creep exponent, n_c depend on the controlling mechanism: grain boundary diffusion, grain boundary sliding, and matrix creep due to bulk diffusion. The mechanism which dominates depends on the temperature and stress level. Shine and Fox [27] have illustrated that there is little correlation between fatigue life due to creep damage and grain boundary creep. In addition, grain boundary creep dominates at high stresses (> 20 MPa), and is not considered in this study.

In order to simplify the analysis method, Equations 4.9 and 4.10 can be combined and simplified to give a Weertman steady state model:

$$\dot{\varepsilon}_c = \varepsilon_0 \sigma^{n_c} e^{-\left(\frac{\Delta H}{kT}\right)} \qquad 4.11$$

At any constant temperature experimental data of $\dot{\varepsilon}_c$ versus applied shear stress provides n_c and $\varepsilon_0 e^{-\left(\frac{\Delta H}{kT}\right)}$ by power-law regression. The test temperature and the activation energy

for the creep mechanism enable calculation of ε_o. Another group of investigators use a Norton equation to express the creep strain rate in which the coefficient and exponent are temperature dependent. [29]

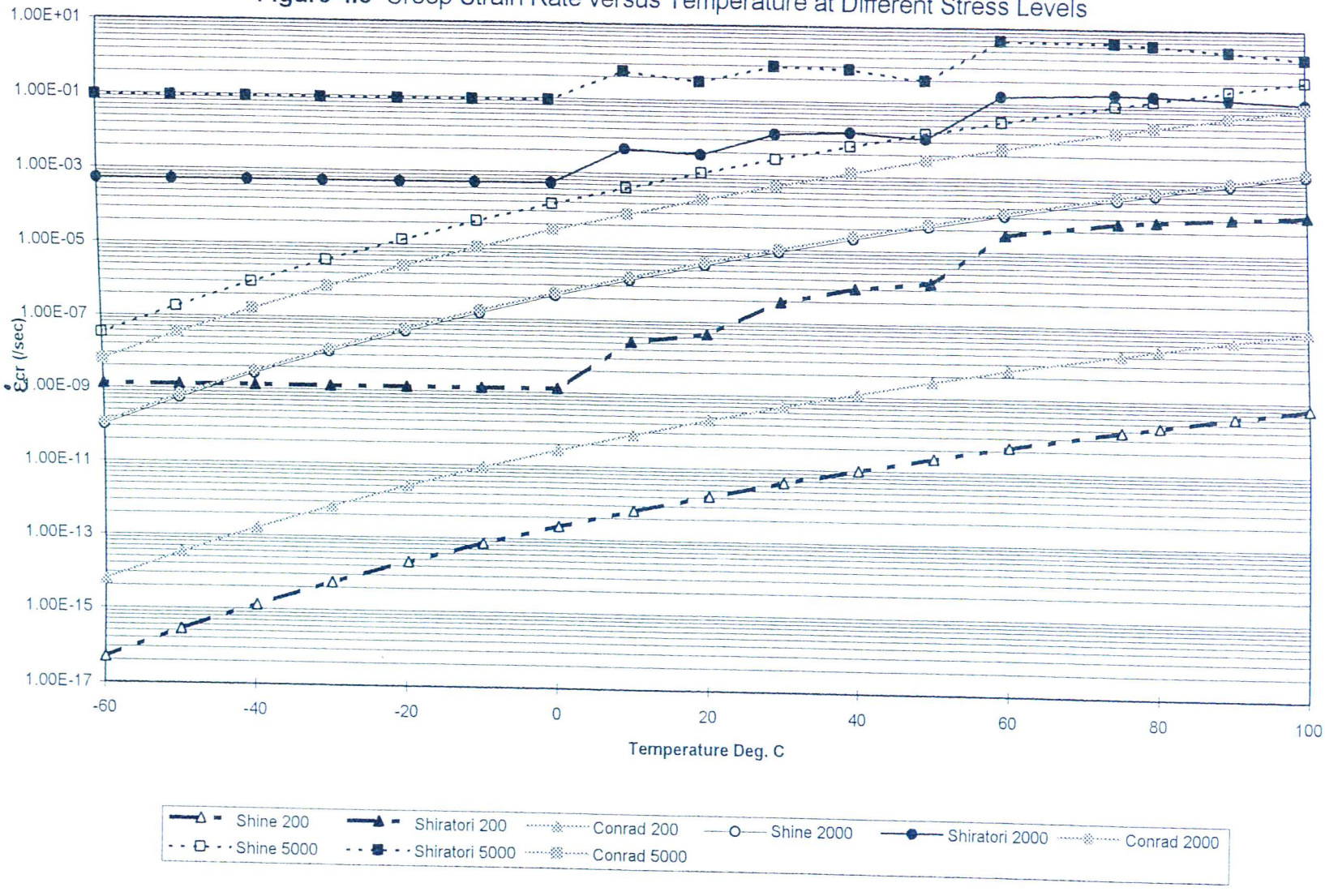
$$\dot{\varepsilon}_c = A(T)\sigma^{n_c(T)} \qquad 4.12$$

Investigator	Shine [27]	Conrad [28]	Temp. Deg C	A %/hr*Mpa^n	nc	Shiratori [29]
εo /sec*Mpa^n	2.56E-01	6.70E+01	0	3.57E-10	5.6	
nc	6.3	4.3	25	1.98E-08	4.7	
ΔH/k	8165.2	8165.2	50	6.42E-07	3.9	
			100	7.04E-05	3	

Table 4.3 Creep Material Properties from Several Investigators

Figure 4.3 shows creep strain rate versus temperature at stresses of 200, 2000, and 5000 psi (1.379, 13.79, and 34.48 MPa) respectively, using the creep material properties given in Table 4.3. It is noteworthy that the creep response can change drastically depending on which experimental properties are used for the analysis. This effectively illustrates how differences in FEM results can change from study to study depending on the constitutive model. Care must be taken to ensure that the FEM results, based on whichever constitutive model is chosen, represent the physical response of the system. For this study, each of the constitutive models was evaluated using finite elements, and based on the monotonic results, the creep properties reported by Shine [27] are chosen.

Figure 4.3 Creep Strain Rate versus Temperature at Different Stress Levels



4.2.2 FEM Modeling

In order to facilitate the complex numerical calculations involved in the stress analysis, the geometry is modeled approximately as two dimensional plane stress. This is recognized to be an assumption, since the loads and the material responses are three-dimensional in nature, with the stress distribution in the fillet region consisting of combined normal, bending, and shear stress which varies throughout the thickness. The solder joints of the LCCs tested as described in Section 2 are examined in detail to accurately model the solder joint profile. It is widely understood that the shape of the solder joint greatly affects the fatigue life, and the IPC model, in an attempt to account for this variability includes a fillet thickness factor (F) which can range from 1.2 to 0.7 for LCCs. [23] The geometry is generated using Patran 3 commercial finite element software, and the nonlinear numerical analysis is conducted using Abaqus 5. The geometry is described in Appendix I.

All materials except solder are treated as linear elastic. The dimensions and material properties are given in Appendix I. The FEM mesh is generated using 4 noded quadrilateral generalized plane stress elements which have two displacement degrees of freedom per node. Symmetric boundary conditions are applied along the center of the component. The bottom of the substrate is constrained in the thickness direction to prevent board warpage. The thermal loads which correspond to those encountered during the accelerated test are applied to the structure in a piecewise incremental fashion. In

order to evaluate the effect of creep during the temperature loading and unloading, the analysis is carried out as follows:

1. A small temperature change is applied to the structure (2 °C for this study) and an elastic-plastic analysis is conducted.
2. The elastic-plastic analysis is followed by a creep analysis with a dwell equal to the time taken for the temperature change of the previous step. For example, when the ramp rates are 10 °C/min and each step consists of a 2 °C temperature change, the time for each step is 12 seconds.
3. The creep analysis is performed at the upper and lower dwell temperatures for times corresponding to those encountered during the accelerated test. [29]

In reality, creep occurs at all times during the loading and unloading, not just once every 12 seconds. It is postulated that if this analysis were to be performed using smaller temperature increments, the stresses would decrease, while the creep strains would increase accordingly. However, the area under the hysteresis plot corresponding to creep would converge to a single value. This approximation remains valid because the useful parameter is the creep work dissipated in the energy partitioning model. This approximation would present problems when using the strain range partitioning model. This analysis is conducted for two thermal cycles to eliminate the effects of ratcheting and thermal shakedown. The calculations for strain energy, plastic work, and creep work densities are done using stress-strain histories recorded during second thermal cycle. It is noteworthy that some previous studies which have used the CALCE energy partitioning

model ignored the creep during the temperature ramps [25, 26, 31]. This approximation can have a significant impact on the results, as shown in Section 4.2.3.

In order to determine the effect of mesh size on the FEM results, a fine and coarse mesh are evaluated. The first mesh contains 1337 elements and 1426 nodes, and the second mesh contains 269 elements and 314 nodes. Contour plots are generated after a 3 °C elastic plastic step. The maximum stress in both cases occurs at the element located at the heel of the solder joint under the component. In fact, solder joint cracks for LCCs typically begin at the heel and propagate parallel to the underside of the component, then proceed at a 45° angle through the fillet thickness. [9] The maximum stress at this element for both meshes differs by less than 1%. This small difference when considering the drastic differences in the number of elements for each mesh is not surprising when realizing that the coarser mesh was optimized such that the size of the critical element is as close as possible to the size of that element in the finer mesh, while allowing the other elements to become larger. This type of convergence study is desirable, because it allows the investigator to obtain the same results with the coarser mesh while saving computational time. The computational time for finer meshes while doing nonlinear analyses can be twice as long, which becomes more important when the analysis is performed several times.

4.2.3 FEM Results

As stated earlier, the there are some assumptions and limitations when using a 2-D stress analysis to represent a 3-D mechanical system. The fact that the shear stress distribution changes through the thickness of the fillet of the solder joint does not greatly effect the results, however, because the critical location occurs at the heel of the solder joint. Three-dimensional finite element analyses [9] have shown that the maximum stress occurs at a cross section taken about the center of the solder joint at the heel, which is the same location that is analyzed in this study.

Hysteresis plots of the critical element are partitioned into their elastic, plastic, and creep components as discussed in Section 4.1.2. These hysteresis plots, as shown in Figure 4.4 show how the combined effect of the size of the component and the differential thermal expansion affect the stress-strain curve, and thus the energy associated with the hysteresis loop.

The effect of allowing creep during the loading as opposed to allowing creep during only the dwells is summarized as follows:

1. The beginning of the dwell for the first thermal cycle (labeled "b-c") shows that a large portion of the creep strains occur during that dwell. During the second thermal cycle, after ratcheting and thermal shakedown, the majority of the creep strains occur during the temperature loading , while only a small portions of the creep strains for that cycle occur during the dwell. This illustrates the significance of both eliminating the thermal

shakedown from the first thermal cycle, and more importantly the creep damage which occurs during the loading. These results suggest that if the ramp rates are slow enough, the importance of the dwell is minimal for fatigue damage.

2. In previous studies, the creep strain was not considered during the loading which underestimates the strains and overestimates the stresses. In addition, not considering the stress relaxation due to creep during the loading causes the portion of creep strain to become interchanged with plastic strains. As the damage model implies, erroneously shifting the failure mechanism can lead to poor life estimations.
3. During the temperature unloading, at relatively high temperatures, if the creep behavior is not considered, the creep strains once again are significantly underestimated.
4. Almost no creep damage occurs at the low temperature dwell.

The fact that a low portion of the total creep strains occur during the high temperature dwell is an important observation when considering that accelerated tests are often performed with extended dwell times in order to maximize the stress relaxation. Instead, the goal should be to optimize the damage while minimizing the test time. Engelmaier suggests that in applying his model to an accelerated test, the high temperature dwell be conducted for at least one hour for the stresses to relax completely. This study shows rather effectively that the majority of the creep damage can be induced within a few minutes of the high temperature dwell.

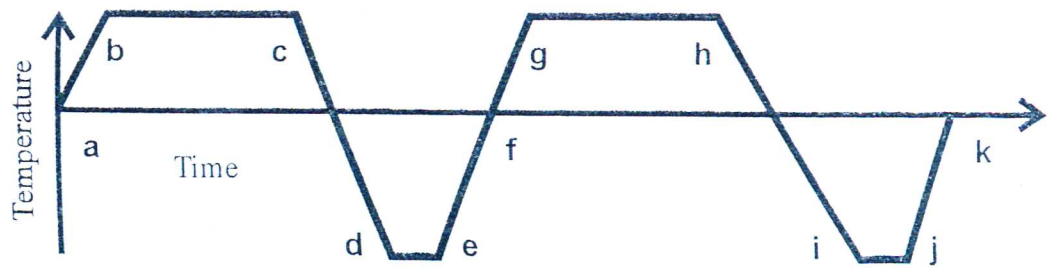
At relatively low temperatures, as the creep constitutive model dictates, less stress relaxation can occur even when considering creep during the unloading. The stress eventually exceeds the temperature dependent yield stress and plastic strains occur. However, during the low temperature dwell, the creep strains are very small. This is explained by the fact that the creep strain rate as shown in Figure 4.3 at low temperatures and high stresses (5000 psi, 34 MPa) is on the order of 10^{-7}/sec. When multiplied by the total low temperature dwell time, the creep strains during the dwell are negligible. It is a common practice for simplicity that the dwell time at the low temperature is chosen to be equal to the dwell time at the high temperature. However, the high costs which can be incurred by maintaining low temperatures in the test chamber for longer dwell times cannot be justified. This explains why a relatively short dwell time, in which the main goal is to allow the solder to reach thermal equilibrium, is chosen for this study, and is highly recommended for future accelerated tests.

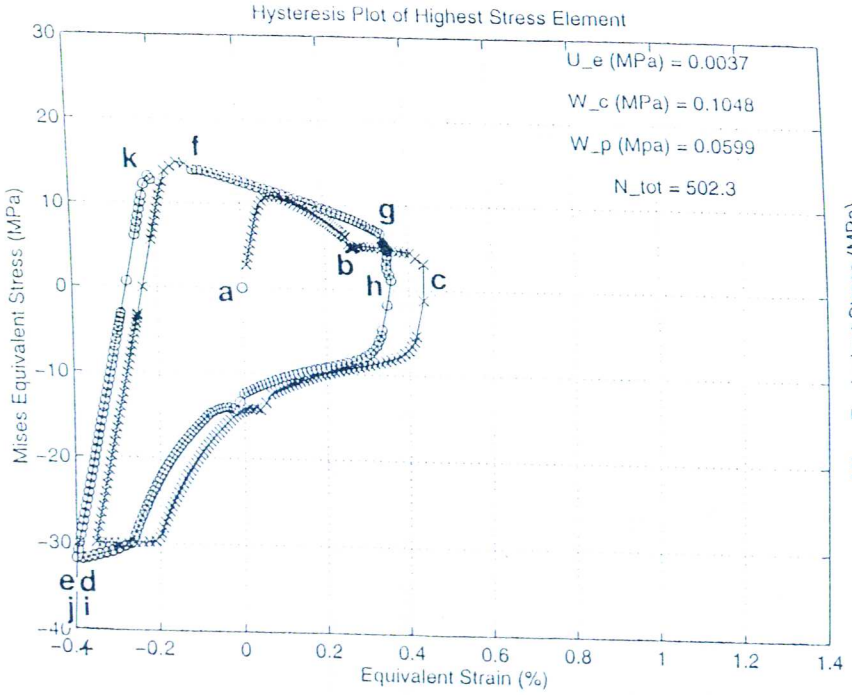
$L_d\Delta\alpha$ 10E 6 mils/C	Ue (MPA)	Wp (MPA)	Wc (MPA)	Nfe	Nfp	Nfc	Nf
5372	0.0034	0.0668	0.2043	6.57E+12	4.54E+05	282.8	282.6
4902	0.0034	0.0687	0.1857	6.57E+12	4.33E+05	307.0	306.7
4257	0.0034	0.0651	0.1669	6.57E+12	4.74E+05	336.6	336.4
3707	0.0035	0.0614	0.1574	5.59E+12	5.22E+05	354.1	353.8
3166	0.0036	0.0602	0.1385	4.78E+12	5.40E+05	395.4	395.1
2592	0.0037	0.0599	0.1048	4.11E+12	5.44E+05	502.8	502.3

Table 4.4 Fatigue Life from FEM Analysis and Energy Partitioning Model.

The fatigue life is calculated using the energy partitioning method based on the previously obtained fatigue constants, as shown in Table 4.4. Note that as the displacement (and thus the creep work dissipated) increases by about a factor of two, the life decreases by a factor

of two. This relationship is seen because the majority of the damage is due to the creep strains, and the Energy Partitioning fatigue constants for creep use a Coffin-Manson slope of approximately -1.0, which suggests fatigue life is approximately linearly related to creep work. However, the experimental failure data for this test suggests that the Coffin-Mason slope should be flatter. It stands to reason that if the damage model is giving poor fatigue life estimations for an accelerated test, this discrepancy will be magnified for fatigue life estimations in the field, where the stresses and the proportions of damage due to the different mechanisms changes. Thus the model constants are updated in the next section to improve accuracy of the prediction.





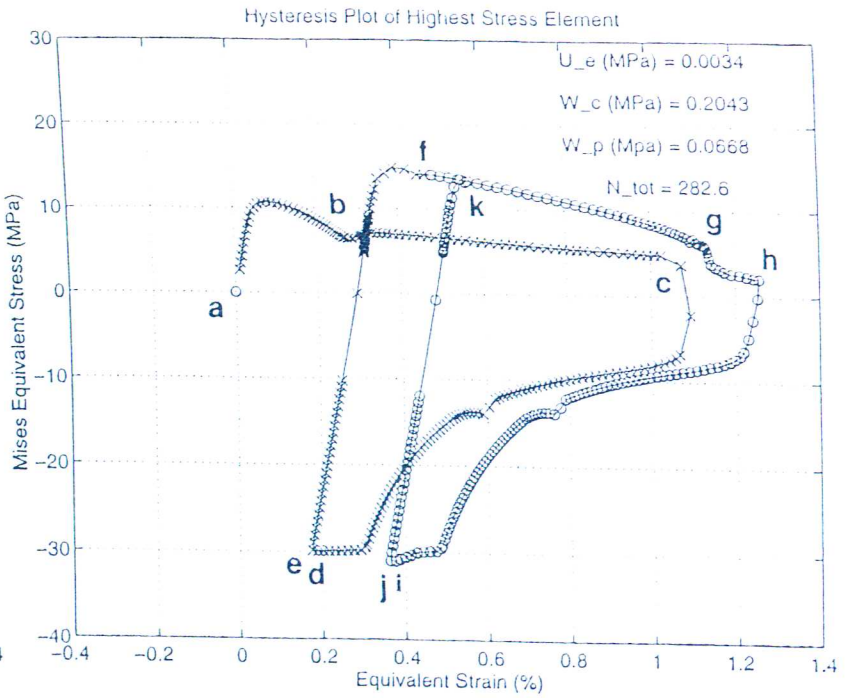


Figure 4.4a $L_d\Delta\alpha$ = 2592 X10^{-6} mils/ °C

Figure 4.4b $L_d\Delta\alpha$ = 5372 X10^{-6} mils/ °C

Example Hysteresis Plot of Mises Equivalent Stress vs. Total Equivalent Mechanical Strain

4.3 Energy Partitioning Update

The constitutive model and method of analysis are continuously being modified and improved as we increase our understanding of the actual damage mechanisms, the physical parameters which contribute to the damage mechanisms and how that damage relates to useful life. In addition, the damage model which ultimately relates the damage to fatigue life estimation must be refined. As stated earlier, the fatigue constants do not match the experimental results, and therefore will not match the field results. In order to obtain better predictions, the experimental data along with the FEM results are used to improve the damage model.

In order to correctly evaluate the fatigue constants, we once again refer to Solomons [30], data for mechanical cycling of eutectic solder at different temperatures. Solomon provides Coffin-Manson fatigue curves for plastic strain versus fatigue life at low temperature (-50 °C), where the creep strains are assumed to be negligible. This data at 50% load drop provides the following relationship:

$$\Delta\varepsilon_p = \Delta\varepsilon_{po} N_{fp}^{\ c} \Rightarrow \Delta\varepsilon_p = 0.3 N_{fp}^{\ 0.38} \qquad 4.13$$

However, the goal is to relate the damage in the strain domain to the energy domain. There is a unique relationship between strain and energy based on the constitutive model. The exponents are related by the following[25]:

$$c' = (1 + n_p)c = (1 + 0.14)(-0.38) = -0.43 \qquad 4.14$$

The next task is to relate $\Delta\varepsilon_{po}$ to W_{po}. This is done quite simply by evaluating the following integral:

$$W_{po} = 2\int_0^{\Delta\varepsilon_{po}} \sigma d\varepsilon_p \qquad 4.15$$

From the Ramberg-Osgood plastic model at low temperature and high strain rate we get:

$$W_{po} = 2\int_0^{\Delta\varepsilon_{po}} K\varepsilon_p^{n_p} d\varepsilon_p \qquad 4.16$$

$$W_{po} = \frac{2K\Delta\varepsilon_{po}^{n_p+1}}{n_p+1} = 14.7 \qquad 4.17$$

Note that the plastic fatigue constants, W_{po} and c' listed in Table 4.1 are incorrect in part due to typographical errors in [30]. The next goal is to reevaluate the creep fatigue constants relative to the new plastic fatigue constants, the experimental failure data and the FEM simulations of the damage due to the accelerated test environment. The strain energy, plastic, and creep work dissipated is determined from the FEM analysis at different values of $L_d\Delta\alpha$, therefore, it is necessary to evaluate the functional dependence of the experimental data to $L_d\Delta\alpha$. The experimental data at different values of $L_d\Delta\alpha$ is plotted thermal cycles to failure. The outliers are eliminated from the experimental data using the operational Bayesian method as described in Section 3.3. A power law regression is performed on the experimental data as shown in Figure 4.5 to obtain the following relationship between $L_d\Delta\alpha$ and cycles to failure due to the total (elastic, plastic, and creep) damage:

$$\Delta\alpha L_d = 42200 N_f^{-0.38} \qquad 4.18$$

In order to evaluate the damage due to the creep, the elastic and plastic damage is subtracted from the total damage:

$$D_c = D_{tot} - D_e - D_p, \; where \; D_i = 1 / N_{fi} \qquad 4.19$$

Using Equation (4.18) and the strain energy and plastic work from the FEM analysis along with the new plastic fatigue constants gives:

$$D_c = \left(\frac{\Delta\alpha L_d}{42200} \right)^{1/0.38} - \left(\frac{U_e}{U_{eo}} \right)^{-1/b'} - \left(\frac{W_p}{W_{po}} \right)^{-1/c'} \qquad 4.20$$

Finally, W_c at different values of $L_d\Delta\alpha$ is plotted against N_{fc} ($1/D_c$) to obtain the updated creep constants (d'=-0.4, and W_{co} = 1.8 MPa/cycle$^{d'}$). The updated Energy Partitioning fatigue constants are shown in Table 4.6, and the strain energy and work densities versus fatigue life using these constants is shown in Figure 4.7. FEM analyses using these new fatigue constants will match the experimental results for this study, and therefore can be considered to be more accurate for extrapolations to field conditions.

Figure 4.5 $L_d\Delta\alpha$ versus N_f from Experimental Data at 50% Probability of Failure

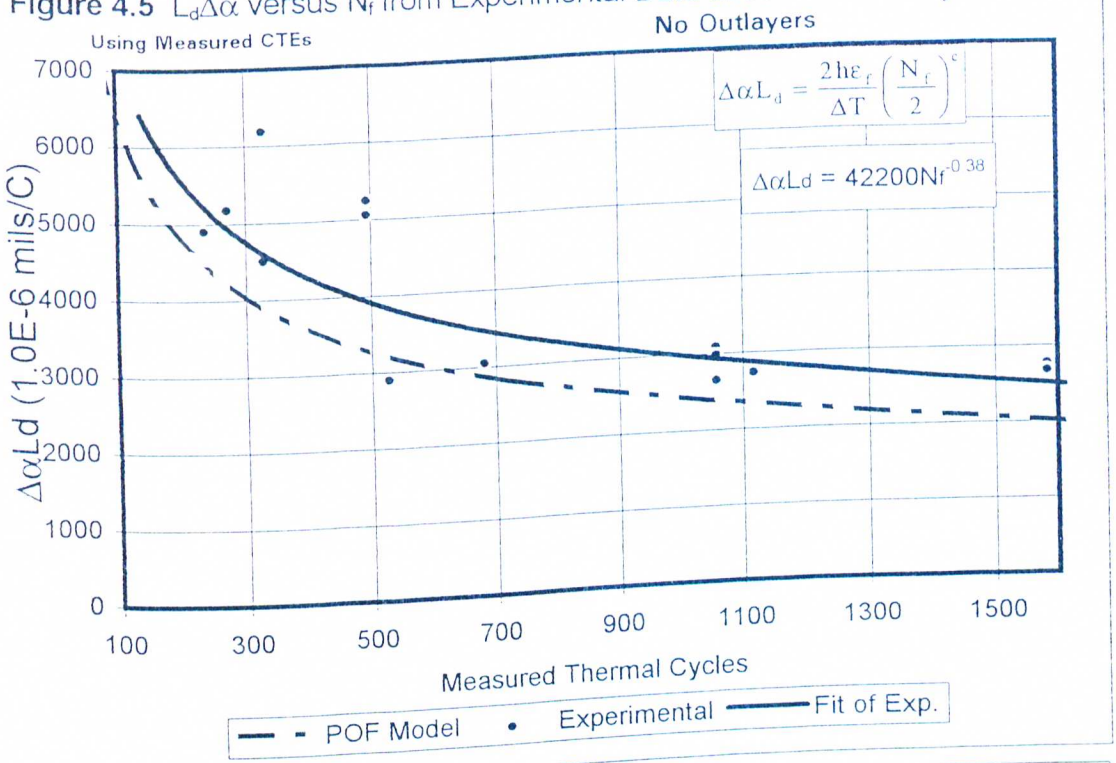
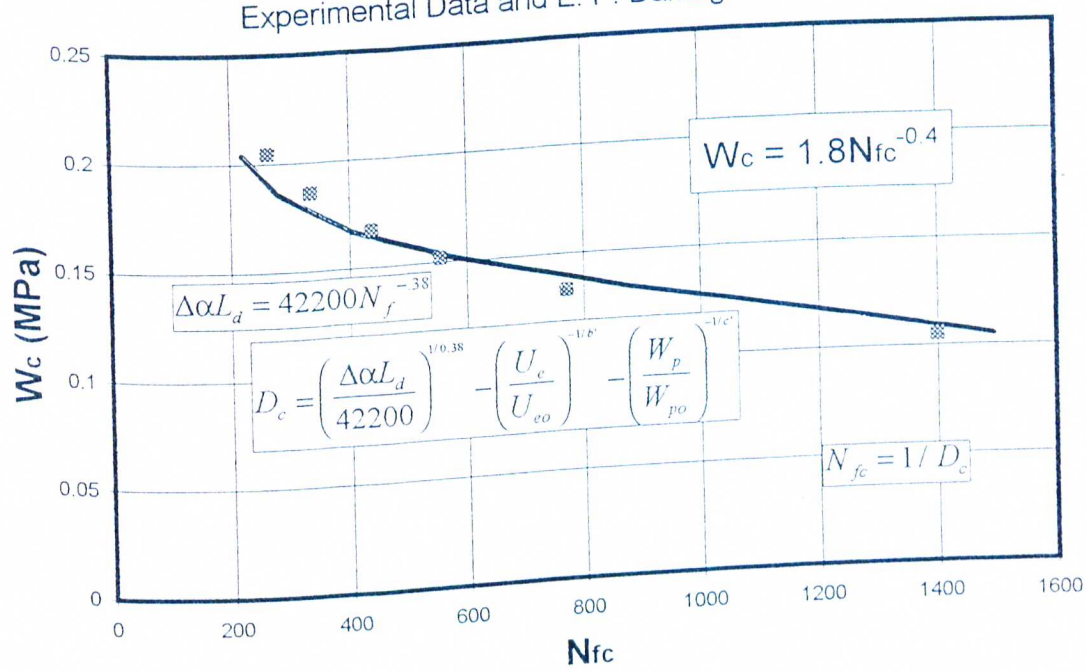
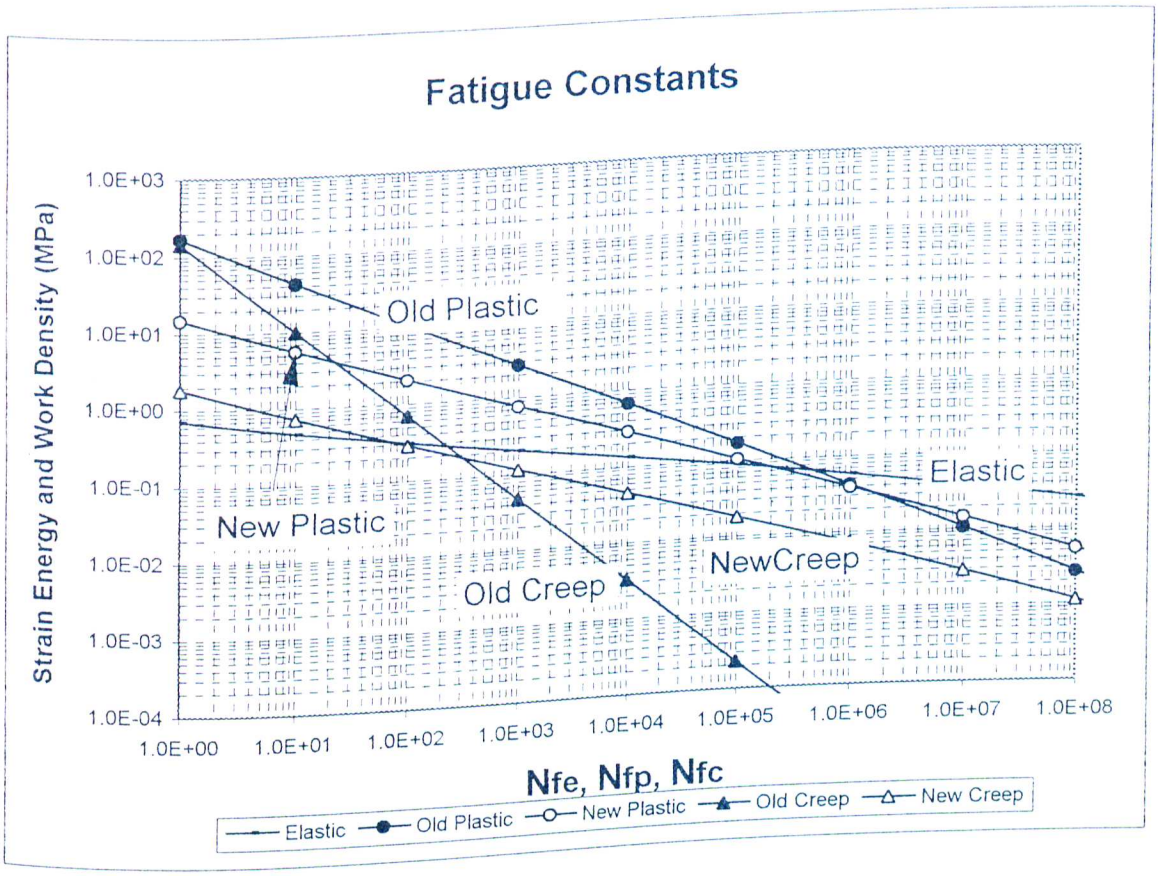


Figure 4.6 Creep work from FEM versus N_{fc} from Experimental Data and E. P. Damage Model





Fatigue Constants for Pb/Sn Solder	
b'	-0.18
c'	-0.6
c' (new)	-0.43
d'	-1.16
d' (new)	-0.4
Ueo	0.698 Mpa/cycle^b'
Wpo	165 Mpa/cycle^c'
Wpo (new)	14.7 Mpa/cycle^c'
Wco	143 Mpa/cycle^d'
Wco (new)	1.8 Mpa/cycle^d'

Figure 4.7 Updated Energy Partitioning Fatigue Constants

4.4 Physics-of-Failure Acceleration Transforms

The acceleration transform is computed from the measured material responses by separating the failure data into fifteen groups according to component size, component location, and module on which the component is placed. Each component in each of the groups has the same differential thermal expansion.

Acceleration transforms are computed using Equation (4.4) and are shown in Figure 4.8. Each value for ΔT_{eff} is plotted against the cycles to failure for a given probability of failure, as determined from the three-parameter Weibull distributions of the corresponding experimental failure data with the outliers eliminated using the operational Bayesian method. The acceleration transform for the reference configuration at 50% probability of failure is shown in Figure 4.8. The fitting of the ΔT_{eff} versus experimental cycles to failure is done according to a power-law relationship ($\Delta T_{eff} = aN_f^b$). For this study, the reference configuration has been chosen to be a 68-pin component on a substrate consisting of a glass/polyimide laminate with copper-invar-copper (CIC) foils for constraining the CTE. The substrate is mounted on an aluminum heatsink. Figure 4.8 also shows the theoretically predicted acceleration transform according to the physics-of-failure model given in Equation (4.1). Similar plots at 5%, 10%, and 25% probability of failure are shown in Appendix N.

The data is right censored, meaning that some of the specimens in each population have not failed. The censoring of the data is implicitly taken care of in the acceleration transform

because the Weibull distributions used to compute the measured thermal cycles at each percent probability of failure makes use of the censored data. Additional plots can be generated by this method for any reference combination of component size and module material at different probabilities of failure.

There is clearly some disagreement between the experimentally obtained acceleration plots and the analytical prediction. The differences can be attributed partially to the limitations and assumptions of the physics-of-failure model used in this study, and partially to the limitations of the test methods.

The IPC SM-785 physics-of-failure model includes assumptions and fatigue properties which are not valid at the temperatures and dwell times encountered during this accelerated test. Since this model is recommended for use only above the temperature of 20 °C and dwell times of at least 1 hour, it is not well suited for accelerated testing outside these specifications. Fortunately, Equation (4.4) which is used to compute the experimental acceleration transform is independent of the fatigue properties proposed by the physics-of-failure model. In this paper, this model is used only for illustrating the method of extracting acceleration transform data from a single test. As discussed by Engelmaier, the strain range accompanied by creep and stress relaxation can be significantly overestimated in this model, and thus the fatigue life is underestimated. Therefore, the model provides a lower bound for reliability estimates [23]. This is increasingly evident in Appendix N as the range of the temperature cycle increases. The monotonic increase of the deviation between the experimental acceleration transform and this

physics-of-failure model is seen to increase with increasing probability of failure. This suggests that the slope parameter, B = 4.0, recommended in [23] is probably inaccurate. The experimental data for this test gives a different value for B (2.0), and as a result, the disagreement between the experiment and the model is seen to increase with increasing probability of failure. In fact, a survey of other experimental data suggests values much lower than 4.0 for the slope parameter. Clech reports a slope parameter of 2.2 for LCCs. [13]

A nominally uniform solder joint geometry is assumed in this study for simplicity. It is clear from Equation (4.1) that the model is strongly dependent on the height of the solder joint. Typically, solder joint height changes from module-to-module due to the manufacturing processes, and this variability has been considered to be included in the slope parameter in this study, creating additional sources of inaccuracy. Further, the amount of intermetalics formed in each solder joint is dependent on the bond pad surface quality, plating (if any), location on module, and component size (thermal inertia). These manufacturing variabilities affecting bond integrity have also been ignored in the present illustrative example.

In addition to the assumptions about the solder joints, it is assumed that the CTE distribution is uniform across each module, and that it is single valued throughout the temperature range. In fact, the edge effects due to delamination and damage due to repeated thermal cycling can contaminate the failure data as demonstrated in Sections 3.3 and 4.1.1. The assumption that the CTEs can be represented by a single value for the entire temperature range is also not completely valid as shown by the CTE measurements.

The acceleration transform using the calculated and measured CTEs are shown in Figure 4.8. Note that the effect of the calculated CTEs changes the acceleration transform dramatically, especially at lower values of ΔT_{eff}. Life predictions using the calculated CTEs may lead to erroneous conclusions, and the goal of the acceleration transform is to accurately determine the time to failure at lower temperature ranges such as those encountered in an operational environment. This demonstrates the significance of accurate experimental measurements in order to evaluate the critical variables.

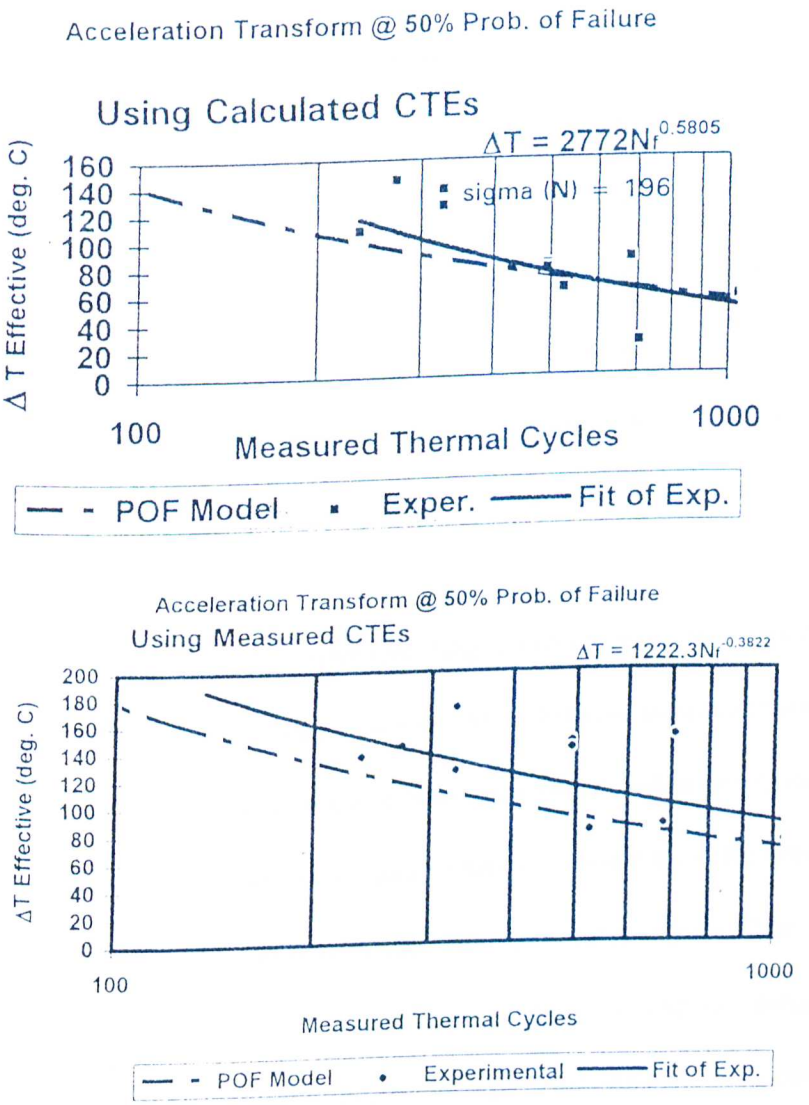


Figure 4.8 Acceleration Transforms at 50% Probaility of Failure

5. Conclusions And Discussions

This research has illustrated that physics-of-failure models and statistical approaches can be used in conjunction with accelerated test data to quantify damage caused in LCC solder joints during temperature cycling and extract acceleration transform information from a single test on a well-designed sample. Further, we can determine the effect of component size, module material, and location of the component on the stresses. Such techniques are essential for cost effective, timely testing of highly reliable modules under accelerated stresses. However, all sources of experimental errors and analytical errors due to assumptions in the model must be monitored closely. Furthermore, these errors must be minimized to create more accurate acceleration transforms and provide quantitative data based on the critical variabilities.

The methodology is illustrated for solder joint fatigue failures on surface-mount printed circuit board modules under thermal cycling; however, the techniques are general enough to be applied to a very broad range of accelerated tests using physics-of-failure models to evaluate the tests and proactively engineer the product. There are several areas for improving the agreement between the semi-analytical models and experimental results. The effect of the non-uniformity of the CTE distributions in the modules is addressed, and the change in the acceleration transform based on calculated versus measured material responses is determined. The difference in the acceleration transform models depending on how the data is analyzed suggests that it is necessary to carefully measure the critical variables, validate all assumptions in the models, and systematically analyze the data searching for outliers which cannot be

physically explained based on our evaluation method in order to obtain accurate acceleration transform information. Bayesian statistics provide a systematic method to determine the maximum-likelihood estimates of the Weibull distribution parameters and confidence on these estimates. Although this method is numerically more difficult, it is more sophisticated and provides a finer analysis than sequentially examining the data. By judiciously eliminating the contaminated data from the population it is possible to obtain more accurate relationships between the distribution parameters, and ultimately the time to failure, and the critical variables in order to obtain the acceleration transform. However, a less conservative choice of a prior distribution should be used in future analyses. The solder fatigue data from the literature and the results of this study can be used in future analyses to obtain more accurate prior distribution information and update the physics-of-failure models to obtain more accurate acceleration transforms. Experimental data confirms (as observed by other researchers) that the IPC model (i) is too conservative under accelerated stress conditions encountered in this study, (ii) overpredicts the Weibull slope parameter by a factor of two.

Two different physics-of-failure models have been used to obtain quantitative insights into this problem. The physics-of-failure FEM modeling performed in this study leads to several important conclusions:

1. The stress analysis in the IPC model is too simplistic to capture complex effects such as multiaxiality and nonuniformity of stress fields, incomplete stress relaxation, and local CTE mismatches.
2. Creep damage dominates while elastic and plastic damage are negligible, for the cases

examined. This explains why models based on total energy have worked reasonably well. However for low temperature behavior, as well as combined temperature and vibrational loading, the energy partitioning method may still provide an advantage.

3. Ratcheting and shakedown is followed by a stable hysteresis loop within a few thermal cycles for the cases examined.

4. Most of the creep damage occurs during the temperature loading and unloading for the ramp rate (10 °C/min.) used in this study. There is very little additional damage done during the high temperature dwell, and there is almost no damage done at the low temperature dwell. Reduction of dwell times is an effective way to reduce testing time when testing for solder fatigue. Decisions to reduce dwell times should also include considerations of time needed to achieve thermal equilibrium and the influence of dwell times on other potential failure mechanisms.

5. At 10 °C/min. ramp rate, creep relaxation causes the maximum stress to be approximately the same for all of the cases examined regardless of the magnitude of loading ($2592 < L_d\Delta\alpha < 5372 \times 10^{-6}$ mils/ °C, $\Delta T = 145$ °C, $T_{sj} = 40$ °C). This leads to an almost one-to-one correspondence between total strain range and energy (mostly creep) associated with the hysteresis loop. This explains why strain-based fatigue models work reasonably well for leadless solder joints. However, this may not be true for leaded components and different loading rates.

6. This study has provided the data necessary to provide a significant update and improvement to the CALCE energy partitioning creep fatigue damage constants

6. Contributions

This research provides an example of using physics-of-failure methodology to combine test data with statistics and analytical-empirical models to obtain quantitative damage metrics and acceleration transforms.

The results from the accelerated test illustrate the importance of accurately modeling loads, critical variables, and constitutive properties of the materials to obtain valuable information to quantify these tests.

The method analysis of is improved and the constitutive model for eutectic tin-lead solder is refined. The CALCE energy partitioning damage model is updated and improved for eutectic solder.

An analytical predictive ability based on this type of physics-of-failure evaluation for accelerated tests will obviously result in significant savings of cost and time and provide valuable information during qualification, reliability enhancement, or screening tests.

Substrate Number	Substrate Material	Thick. mills	Adhesive Type	In Plane CTE ppm/C	In Plane Modulus 10E+6ps	Out of Plane Modulus 10E+6psi	ν_{xy}	ν_{yz}	ν_{zx}
1	Poly/CIC Foil	60.8	Compliant	8.48**	3.915*	1.682*	0.12*	0.3*	0.14*
2A	Poly/CIC Foil	61.8	Compliant	8.48**	3.915*	1.682*	0.12*	0.3*	0.14*
2B	Poly/CIC Foil	62.8	Compliant	8.48**	3.915*	1.682*	0.12*	0.3*	0.14*
3	Poly/CIC Foil	63.8	Compliant	8.48**	3.915*	1.682*	0.12*	0.3*	0.14*
4A	Polyimide/FGlass	41.6	Rigid	15	3.815*	1.682*	0.12*	0.3*	0.14*
4B	Polyimide/FGlass	41.6	Rigid	15	3.815*	1.682*	0.12*	0.3*	0.14*
5	Poly/CIC Foil	58.4	Rigid at Low T	8.48**	3.915*	1.682*	0.12*	0.3*	0.14*
6	Poly/CIC Foil	59.4	Rigid at Low T	8.48**	3.915*	1.682*	0.12*	0.3*	0.14*
7	Poly/CIC Foil	60.4	Compliant	8.48**	3.915*	1.682*	0.12*	0.3*	0.14*
8A	Kevlar/Epoxy	45.6	Very Rigid	5.7	4.0745*	0.8265*	0.05*	0.24*	0.1*
8B	Kevlar/Epoxy	45.6	Very Rigid	5.7	4.0745*	0.8265*	0.05*	0.24*	0.1*
9	Kevlar/Epoxy	49.6	Compliant	5.7	4.0745*	0.8265*	0.05*	0.24*	0.1*
10	Kevlar/Epoxy	57.6	Compliant	5.7	4.0745*	0.8265*	0.05*	0.24*	0.1*
11	Kevlar/Epoxy	51	Compliant	5.7	4.0745*	0.8265*	0.05*	0.24*	0.1*
12	Polyimide/FGlass	65	Rigid	16	3.815*	1.682*	0.12*	0.3*	0.14*
Copper Electro Deposited				16.7*	12.0*	12.0*	.34*	.34*	.34*
Copper Tungsten				5.4*	10.4*	10.4*	.17*	.17*	.17*
60Pb-40Sn Solder				23.9	4.34	4.34	0.4	0.4	0.4
Ceramic				5.4	54.97***	54.97***	0.21***	0.21***	0.21***

Board Number	Core Material	Thick. mills	In Plane CTE ppm/C	In Plane Modulus 10E+6psi	XY Poissons Ratio
1	Al 6061-T6	50	22.7**	11.6*	0.33*
2A	Al 6061-T6	50	22.7**	11.6*	0.33*
2B	Al 6061-T6	50	22.7**	11.6*	0.33*
3	Carbon Comp.	53	0	28	0.12*
4A	20/60/20 CIC	40	5.2	19.6*	0.3*
4B	20/60/20 CIC	40	5.2	19.6*	0.3*
5	Al 6061-T6	50	22.7**	11.6*	0.33*
6	Al 6061-T6	50	22.7**	11.6*	0.33*
7	Al 6061-T6	50	22.7**	11.6*	0.33*
8A	Al 6061-T6	50	22.7**	11.6*	0.33*
8B	Al 6061-T6	50	22.7**	11.6*	0.33*
9	Carbon Comp.	53	0	28	0.12*
10	Al 6061-T6	50	22.7**	11.6*	0.33*
11	Carbon Comp.	53	0	28	0.12*
12	Lanx. Al/SiC	80	6.9	37.41	0.15*

* CALCE Database
** Laminate Analysis
*** Papers Verma, Das,...
Otherwise measured by HS
1psi=6.895e3 Pa
Poly/CIC Foil is modeled as Polyimide/FGlass except for CTE
Solder Data from International Tin Research Institute (I.T.R.I. Publication No. 65)

Appendix B Failure Data

Group 1
Modules 1,2A,2B,3,7

CIC Foil Boards with Compliant Adhesive
Center Components LCC48-3, LCC32-7,8,9

Failure # /Group	Channel Number	Thermal Cycle	Board Side Number		Component Name	First Fail	
1	15	156	1	A	LCC 68 - 1	156	
2	48	157	2A	A	LCC 68 - 2	157	
3	47	179	2A	A	LCC 68 - 1	179	
4	16	196	1	A	LCC 68 - 2	196	
5	64	216	2A	B	LCC 68 - 2	216	
6	95	218 - 224	2B	B	LCC 68 - 1	218	
7	96	245 - 247	2B	B	LCC 68 - 2	245	
8	32	259	1	B	LCC 68 - 2	259	
9	288	264 & 265	7	B	LCC 68 - 2	264	
10	31	280 - 282	1	B	LCC 68 - 1	280	
11	111	288 & 289	3	A	LCC 68 - 1	288	
12	272	295	7	A	LCC 68 - 2	295	
13	63	296 - 297	2A	B	LCC 68 - 1	296	
14	80	296 - 301	2B	A	LCC 68 - 2	296	
15	287	299 - 300	7	B	LCC 68 - 1	299	
16	79	310 - 313	2B	A	LCC 68 - 1	310	
17	271	312	7	A	LCC 68 - 1	312	
18	112	353 & 354	3	A	LCC 68 - 2	353	
19	127	357 & 358	3	B	LCC 68 - 1	357	
20	128	516 - 527	3	B	LCC 68 - 2	516	
1	45	OFF, 269+	2A	A	LCC 48 - 2	269	Edge
2	44	324	2A	A	LCC 48 - 1	324	Edge
3	28	347	1	B	LCC 48 - 1	347	Edge
4	77	392 - 394	2B	A	LCC 48 - 2	392	Edge
5	268	OFF, 422+	7	A	LCC 48 - 1	422	Edge
6	61	435	2A	B	LCC 48 - 2	435	Edge
7	76	443 & 444	2B	A	LCC 48 - 1	443	Edge
8	285	456	7	B	LCC 48 - 2	456	Edge
9	92	475 - 477	2B	B	LCC 48 - 1	475	Edge
10	46	479	2A	A	LCC 48 - 3	479	Center
11	269	500 - 501	7	A	LCC 48 - 2	500	Edge
12	284	503 - 506	7	B	LCC 48 - 1	503	Edge
13	13	519 - 520	1	A	LCC 48 - 2	519	Edge
14	14	541	1	A	LCC 48 - 3	541	inner
15	12	545	1	A	LCC 48 - 1	545	Edge
16	286	546 - 547	7	B	LCC 48 - 3	546	Center
17	62	565 - 566	2A	B	LCC 48 - 3	565	Center
18	30	589	1	B	LCC 48 - 3	589	Center
19	29	617	1	B	LCC 48 - 2	617	Edge
20	94	645	2B	B	LCC 48 - 3	345	Center
21	93	743	2B	B	LCC 48 - 2	743	Edge
22	78	854 - 855	2B	A	LCC 48 - 3	854	inner
23	108	855	3	A	LCC 48 - 1	855	Edge
24	109	860	3	A	LCC 48 - 2	860	Edge
25	125	937 & 938	3	B	LCC 48 - 2	937	Edge
26	124	956 & 957	3	B	LCC 48 - 1	956	Edge
27	270	981	7	A	LCC 48 - 3	981	Center

Group 1 continued — CIC Foil Acrylic SD113

Modules 1,2A.2B,3,7 — Center Components LCC48-3, LCC32-7,8,9

Failure # /Group	Channel Number	Thermal Cycle	Board Side Number		Component Name	First Fail	
1	85	648 & 649	2B	B	LCC 32 - 4	648	Edge
2	39	708	2A	A	LCC 32 - 6	708	Edge
3	3	727	1	A	LCC 32 - 4	727	Edge
4	37	751	2A	A	LCC 32 - 4	751	Edge
5	42	754	2A	A	LCC 32 - 9	754	Center
6	43	784	2A	A	LCC 32 - 10	784	Edge
7	82	805 & 806	2B	B	LCC 32 - 1	805	Edge
8	35	860	2A	A	LCC 32 - 2	860	Edge
9	38	860	2A	A	LCC 32 - 5	860	Edge
10	36	864 - 866	2A	A	LCC 32 - 3	864	Edge
11	20	888	1	B	LCC 32 - 3	888	Edge
12	34	894 - 895	2A	A	LCC 32 - 1	894	Edge
13	2	907 & 908	1	A	LCC 32 - 1	907	Edge
14	10	912	1	A	LCC 32 - 8	912	Center
15	114	917 & 918	3	B	LCC 32 - 1	917	Edge
16	24	926	1	B	LCC 32 - 7	926	Center
17	283	942	7	B	LCC 32 - 10	942	Edge
18	66	955 & 956	2B	A	LCC 32 - 1	955	Edge
19	72	974 -976	2B	A	LCC 32 - 7	974	Center
20	21	1001&1002	1	B	LCC 32 - 4	1001	Edge

Group 2 — CIC Core
Modules 4A,4B — Center Components LCC48-3, LCC32-7,8,9

Failure # /Group	Channel Number	Thermal Cycle	Board Number	Side	Component Name	First Fail	
1	175	OFF, 269+	4B	A	LCC 68 - 1	269	
2	143	343	4A	A	LCC 68 - 1	343	
3	191	435 - 453	4B	B	LCC 68 - 1	435	
4	160	485 - 491	4A	B	LCC 68 - 2	485	
5	176	495	4A	A	LCC 68 - 2	495	
6	144	852 - 855	4A	A	LCC 68 - 2	855	Center
7	192	870 - 879	4B	B	LCC 68 - 2	879	Edge
1	158	676	4A	B	LCC 48 - 3	676	Edge
2	172	719	4B	A	LCC 48 - 1	719	Edge
1	130	347 - 369	4A	A	LCC 32 - 1	347	Edge
2	134	471 - 476	4A	A	LCC 32 - 5	471	Edge
3	135	500	4B	A	LCC 32 - 6	500	Edge
4	179	619 & 620	4B	B	LCC 32 - 2	619	Edge
5	187	666	4B	B	LCC 32 - 10	666	Edge
6	162	742 & 743	4B	A	LCC 32 - 1	742	Edge
7	182	750 - 756	4B	B	LCC 32 - 5	750	Edge
8	133	893 -894	4A	A	LCC 32 - 4	893	
9	167	1001&1002	4B	A	LCC 32 - 6	1001	

Group 3 — Kevlar
Mod. 8A,8B,9,10,11 — Center Components LCC48-3, LCC32-7,8,9

Failure # /Group	Channel Number	Thermal Cycle	Board Number	Side	Component Name	First Fail	
1	335	460	10	A	LCC 68 - 1	460	
2	351	509 - 511	10	B	LCC 68 - 1	509	
3	336	634 - 636	10	A	LCC 68 - 2	634	
4	384	787	11	B	LCC 68 - 2	787	
5	368	952	11	A	LCC 68 - 2	952	
6	415	(945-947)-341 =604 - 606	8A	B	LCC 68 - 2	604	
7	448	1000-341=659	8B	B	LCC 68 - 3	659	
* 1	410	365-341=24	8A	B	LCC 32 - 9	24	
* 2	402	(404&405)-341 =63 & 64	8A	B	LCC 32 - 1	63	Edge Edge
3	388	751-341=410	8A	A	LCC 32 - 3	410	
4	390	(927-944)-341 =586 - 603	8A	A	LCC 32 - 5	586	

* Were not Plotted in Histograms. Possible Wire Bond Failures.
Modules 8A, 8B were added after other
Boards have completed 341 thermal cycles

Group 4 — Al/SiC Core
Module 12 — Center Components LCC48-3, LCC32-7,8,9

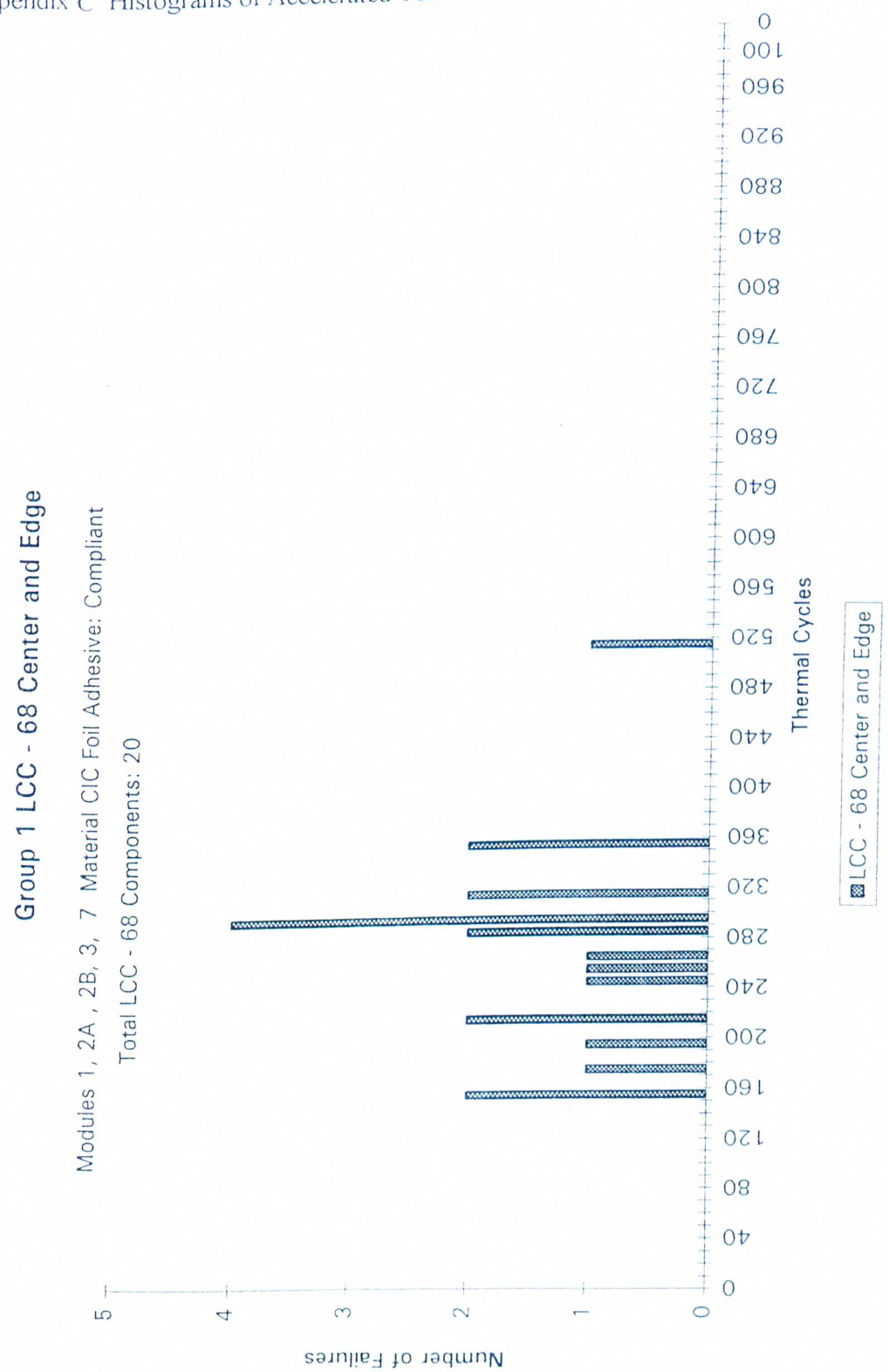
Failure # /Group	Channel Number	Thermal Cycle	Board Number	Side	Component Name	First Fail
* 1	467	567-341=226	12	B	LCC 32 - 2	226
1	463	568-341=227	12	A	LCC 68 - 1	227
2	479	620-341=279	12	B	LCC 68 - 1	279
3	464	865-341=524	12	A	LCC 68 - 2	524
1	458	857-341=516	12	A	LCC 32 - 9	516

* Were not Plotted in Histograms. Possible Wire Bond Failures.
Module 12 was added after other
Boards have completed 341 thermal cycles

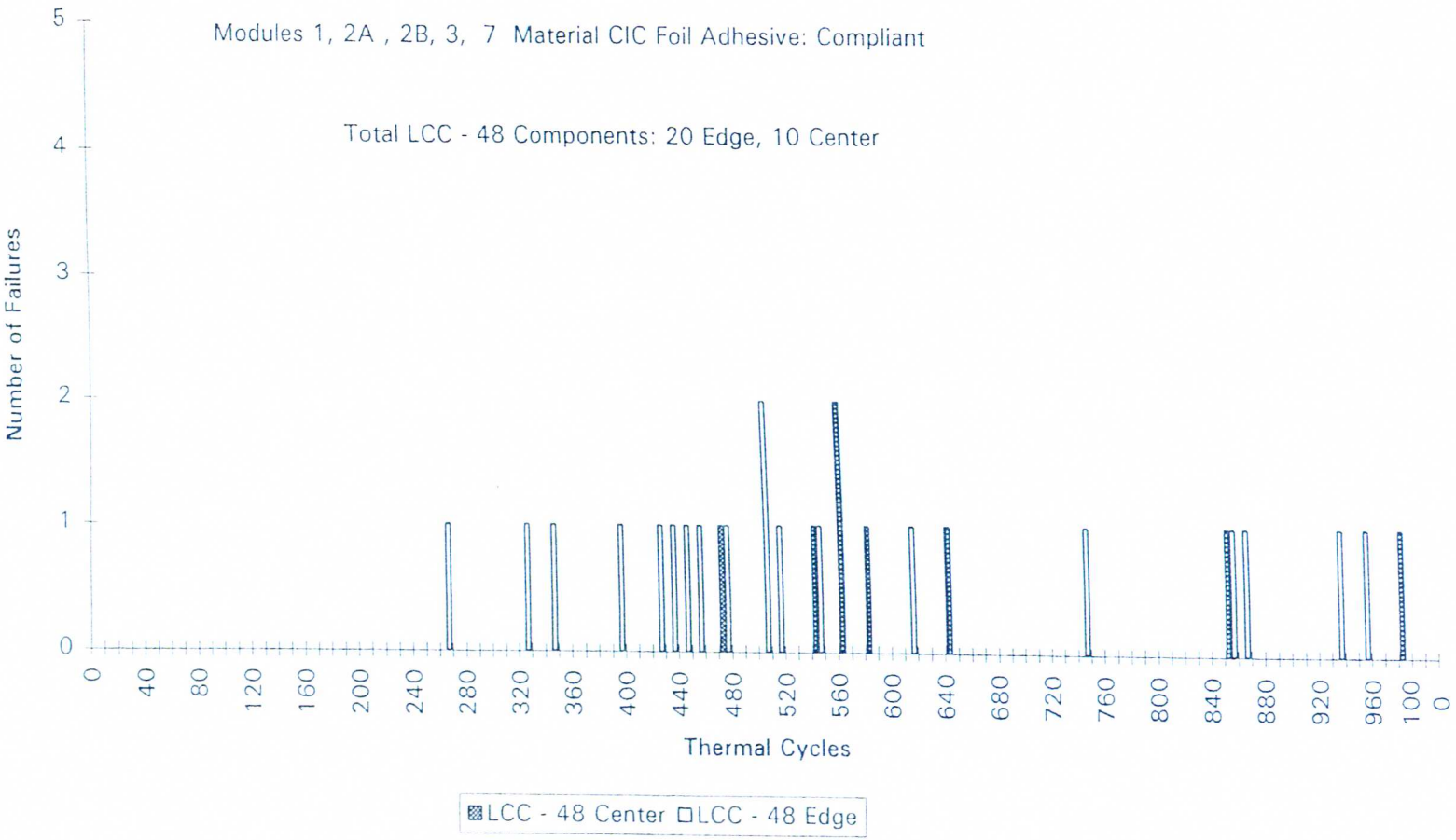
Group 5 — CIC Foil Boards with Adhesive which is Rigid at Low T.
Modules 5, 6 — Center Components LCC48-3, LCC32-7,8,9

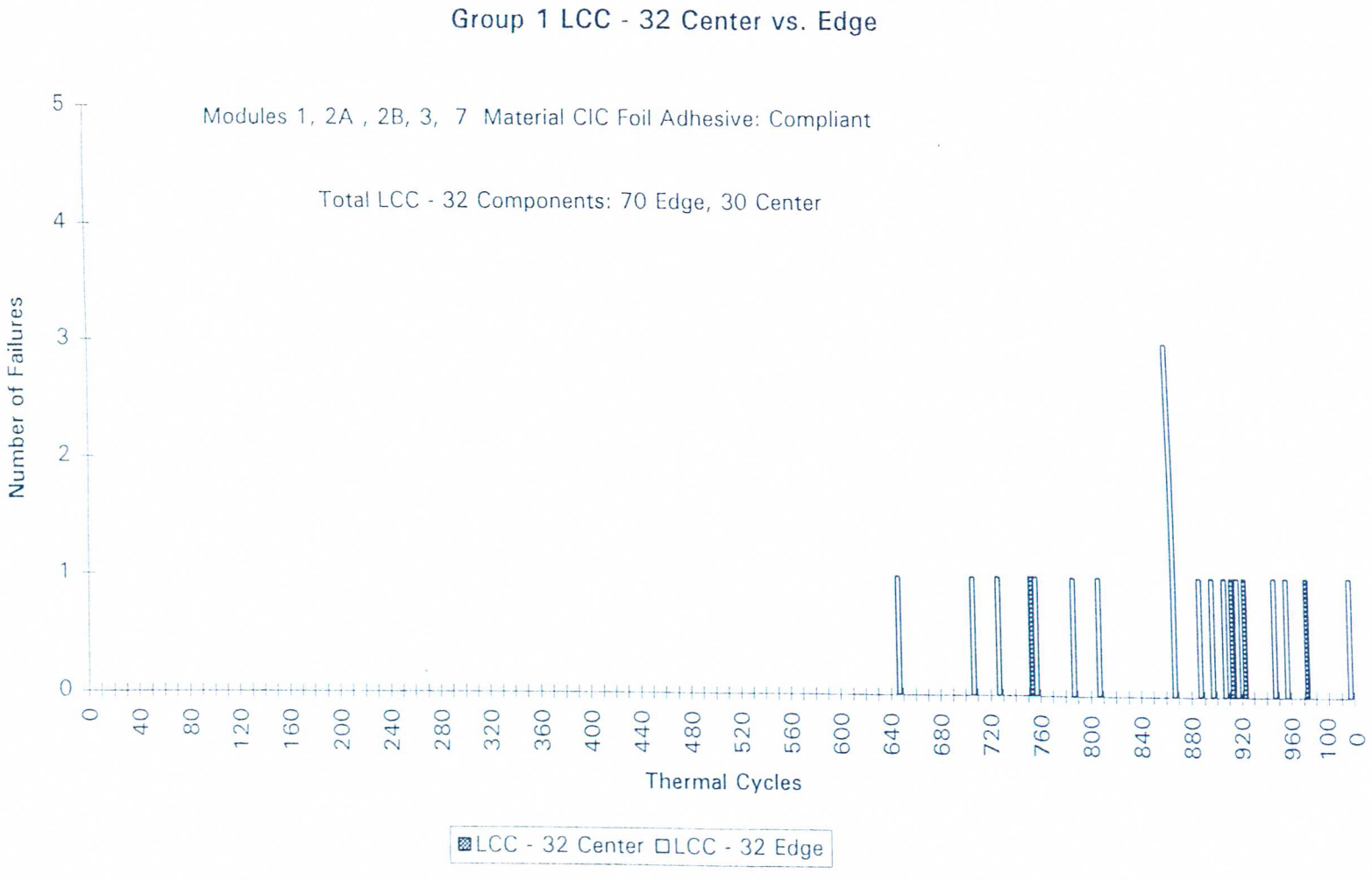
Failure # /Group	Channel Number	Thermal Cycle	Board Number	Side	Component Name	First Fail	
1	240	123	6	B	LCC 68 - 2	123	
2	256	194	6	B	LCC 68 - 2	194	
3	255	252	6	B	LCC 68 - 1	252	
4	208	261 & 261	5	A	LCC 68 - 2	261	
5	239	262 - 264	6	A	LCC 68 - 1	262	
6	207	299 - 303	5	A	LCC 68 - 1	299	Edge
7	223	376	5	B	LCC 68 - 1	376	Edge
1	236	338	6	A	LCC 48 - 1	338	Edge
2	237	431	6	A	LCC 48 - 2	431	Center
3	252	449 & 450	6	B	LCC 48 - 1	449	Edge
4	238	459	6	A	LCC 48 - 3	459	Edge
5	204	590	5	A	LCC 48 - 1	590	Edge
6	220	645 & 646	5	B	LCC 48 - 1	645	Center
7	253	701 & 702	6	B	LCC 48 - 2	701	Edge
8	222	789	5	B	LCC 48 - 3	789	Edge
9	205	890	5	A	LCC 48 - 2	890	outer
10	254	914 - 916	6	B	LCC 48 - 3	914	Center
1	214	402 & 403	5	B	LCC 32 - 6	402	Edge
2	202	728	5	A	LCC 32 - 9	728	Center
3	231	728	6	A	LCC 32 - 6	728	Edge
4	200	734	5	A	LCC 32 - 7	734	Edge
5	245	772	5	B	LCC 32 - 4	772	Edge
6	215	819 - 822	5	B	LCC 32 - 6	819	Edge
7	242	823	6	B	LCC 32 - 1	826	Edge
8	247	826	6	B	LCC 32 - 6	826	Center
9	197	851 - 890	5	A	LCC 32 - 4	851	Center
10	232	882	6	A	LCC 32 - 7	882	Center
11	217	887	5	B	LCC 32 - 8	887	Edge
12	234	939	6	A	LCC 32 - 9	939	
13	213	995 & 996	5	B	LCC 32 - 4	995	

Appendix C Histograms of Accelerated Test Failure Data

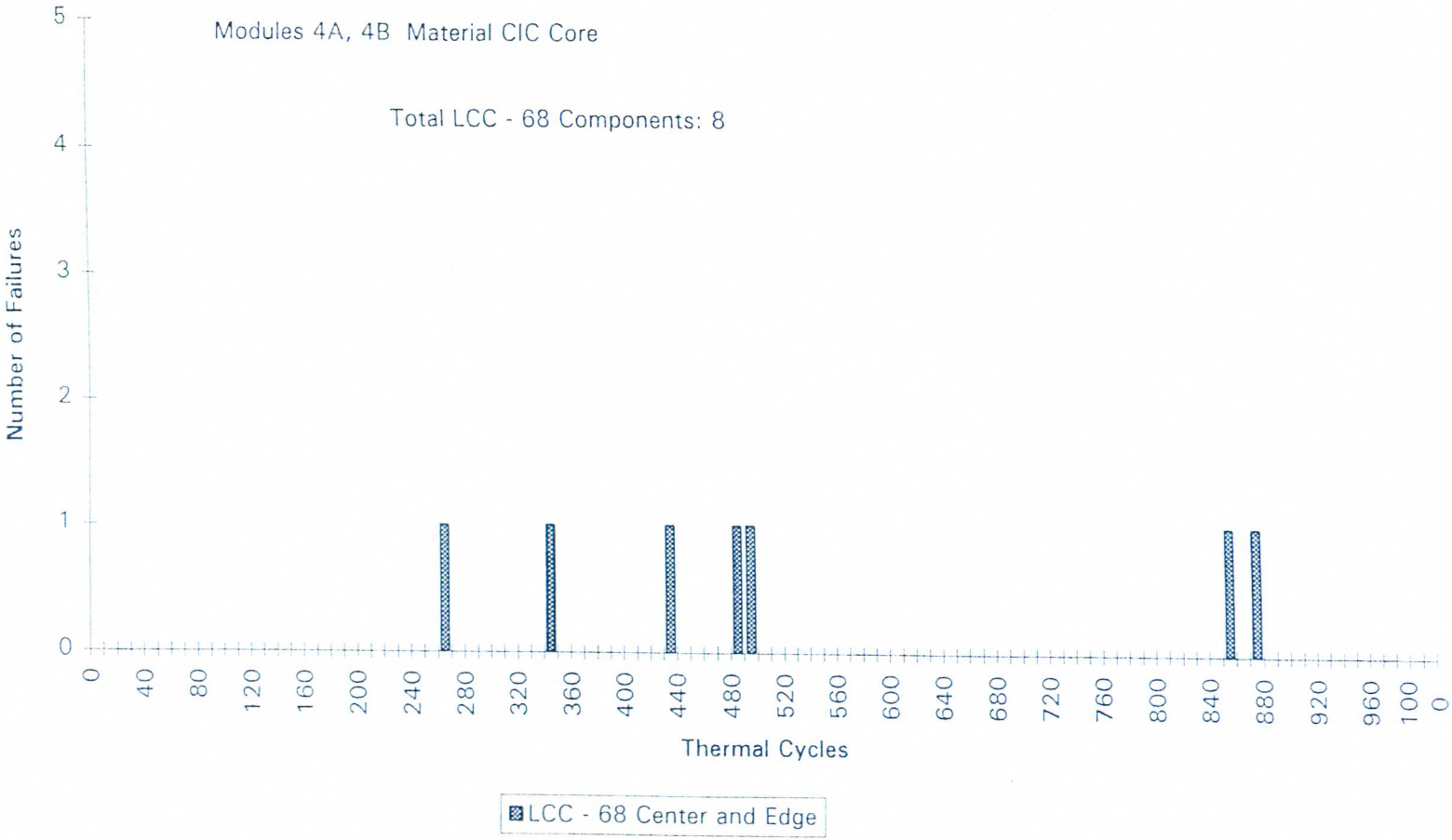


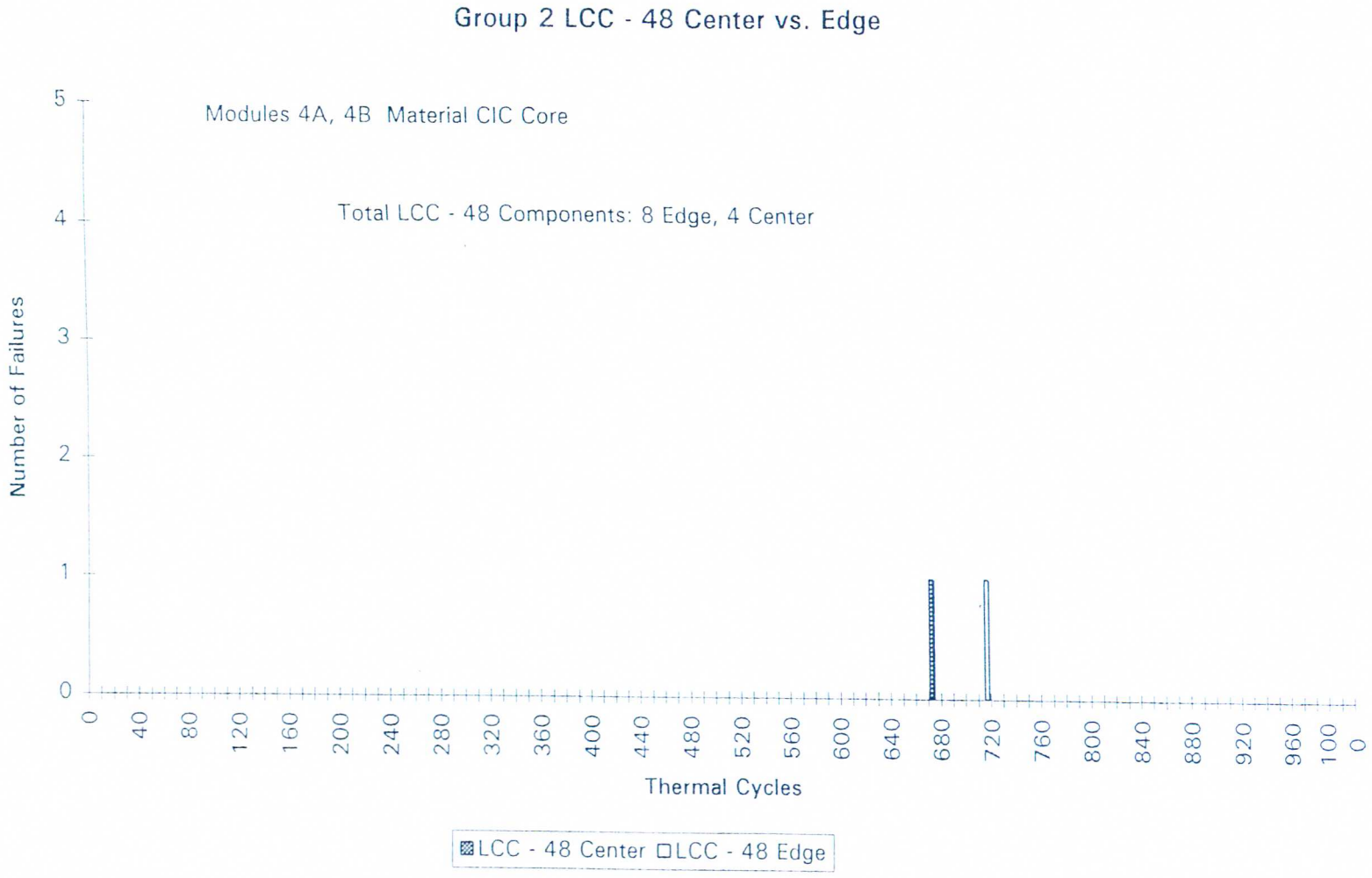
Group 1 LCC - 48 Center vs. Edge



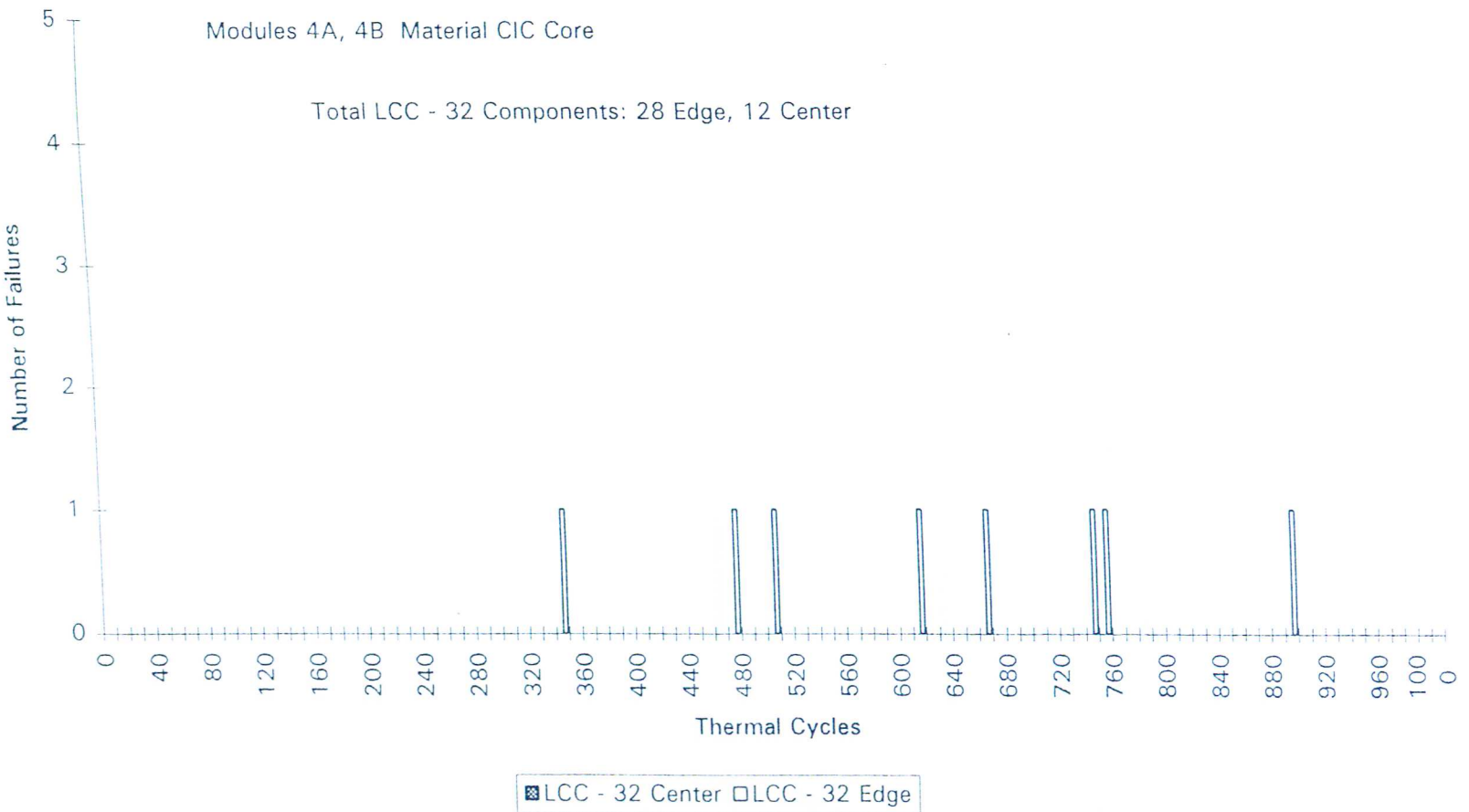

Group 1 LCC - 32 Center vs. Edge
Modules 1, 2A , 2B, 3, 7 Material CIC Foil Adhesive: Compliant
Total LCC - 32 Components: 70 Edge, 30 Center
Number of Failures
0
1
2
3
4
5
0
40
80
120
160
200
240
280
320
360
400
440
480
520
560
600
640
680
720
760
800
840
880
920
960
100
0
Thermal Cycles
LCC - 32 Center
LCC - 32 Edge

Group 2 LCC - 68 Center and Edge

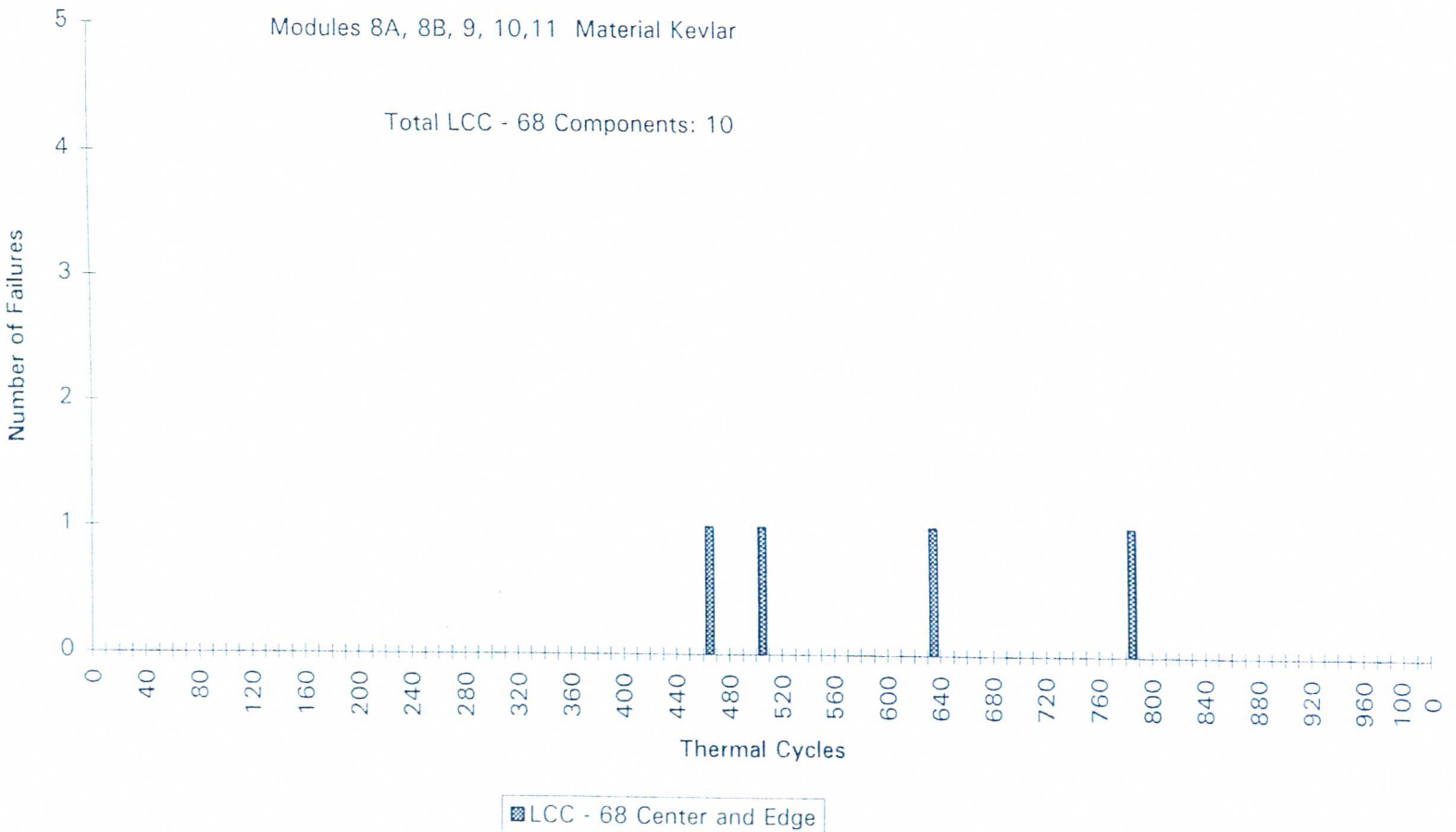



Group 2 LCC - 48 Center vs. Edge
Modules 4A, 4B Material CIC Core
Total LCC - 48 Components: 8 Edge, 4 Center
Number of Failures
0
1
2
3
4
5
0
40
80
120
160
200
240
280
320
360
400
440
480
520
560
600
640
680
720
760
800
840
880
920
960
1000
Thermal Cycles
LCC - 48 Center
LCC - 48 Edge

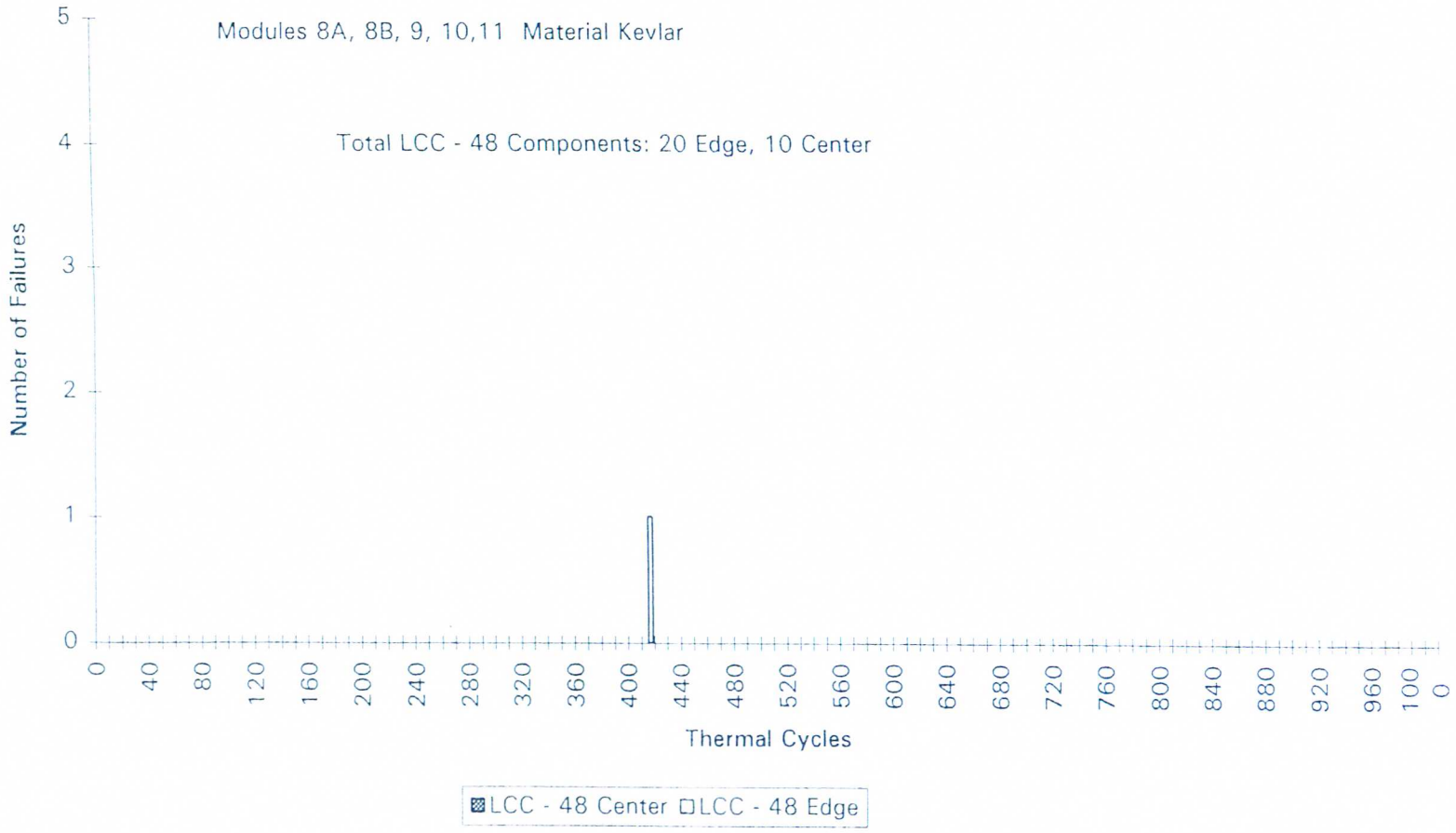
Group 2 LCC - 32 Center vs. Edge



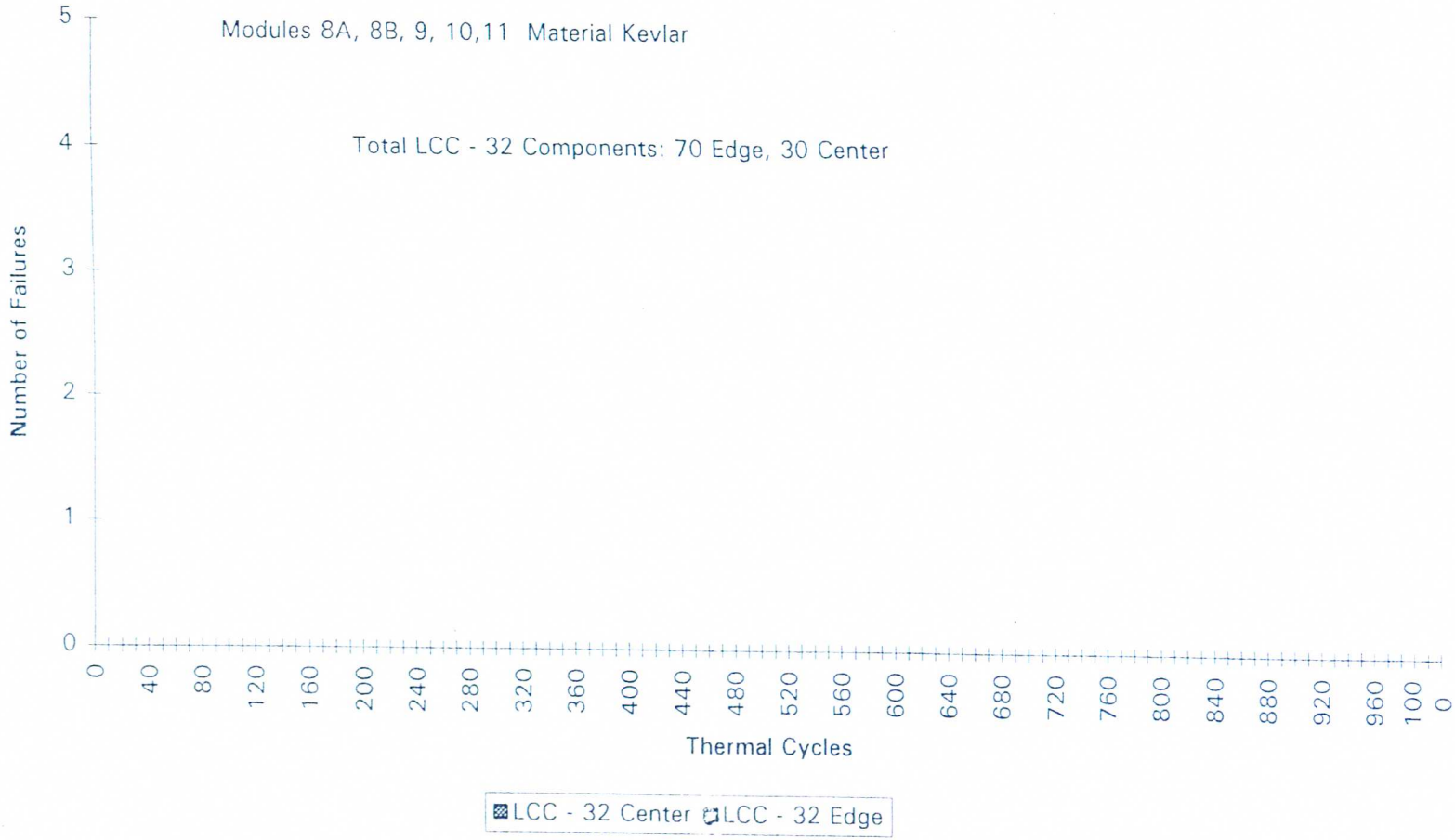
Group 3 LCC - 68 Center and Edge

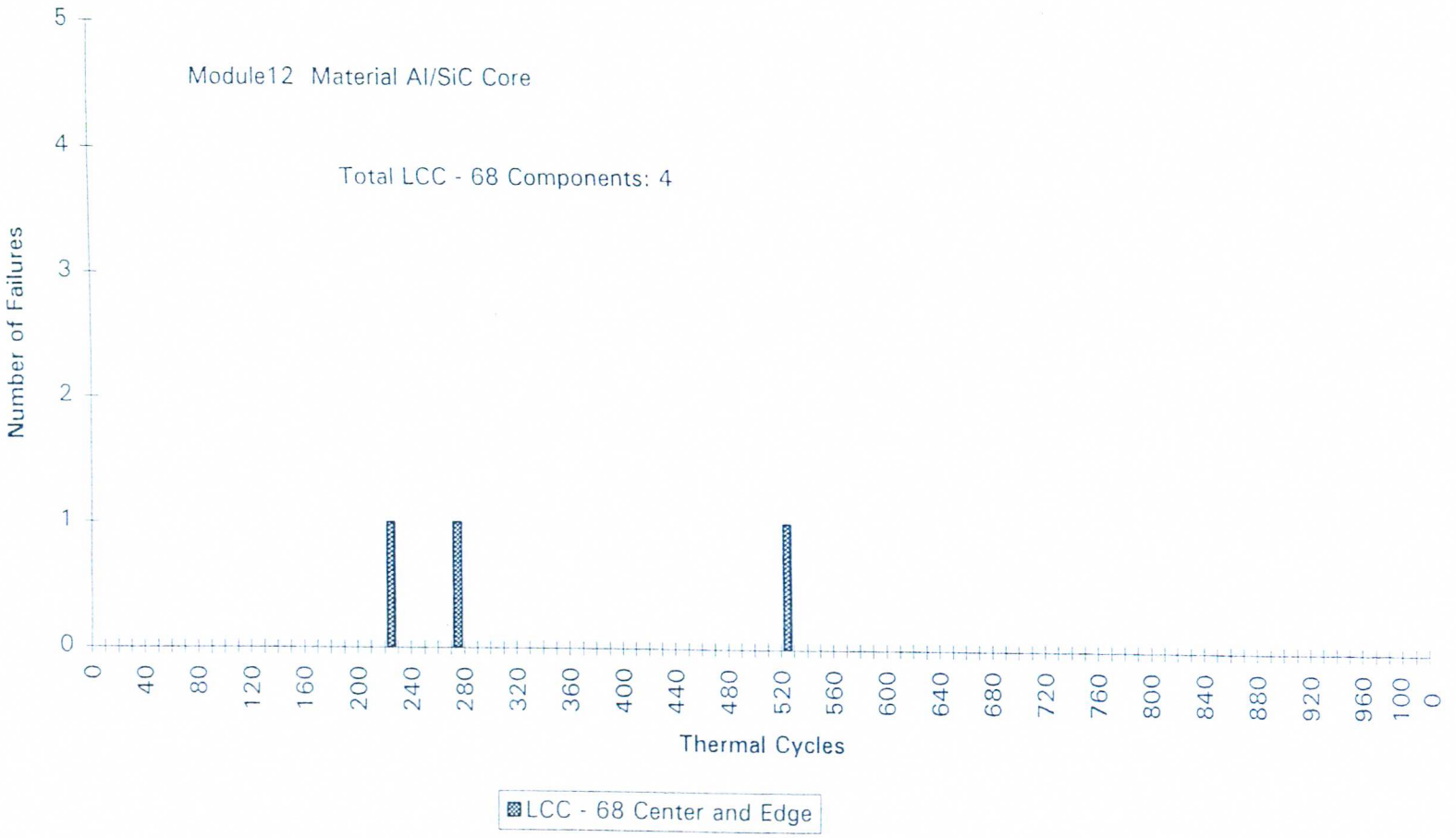


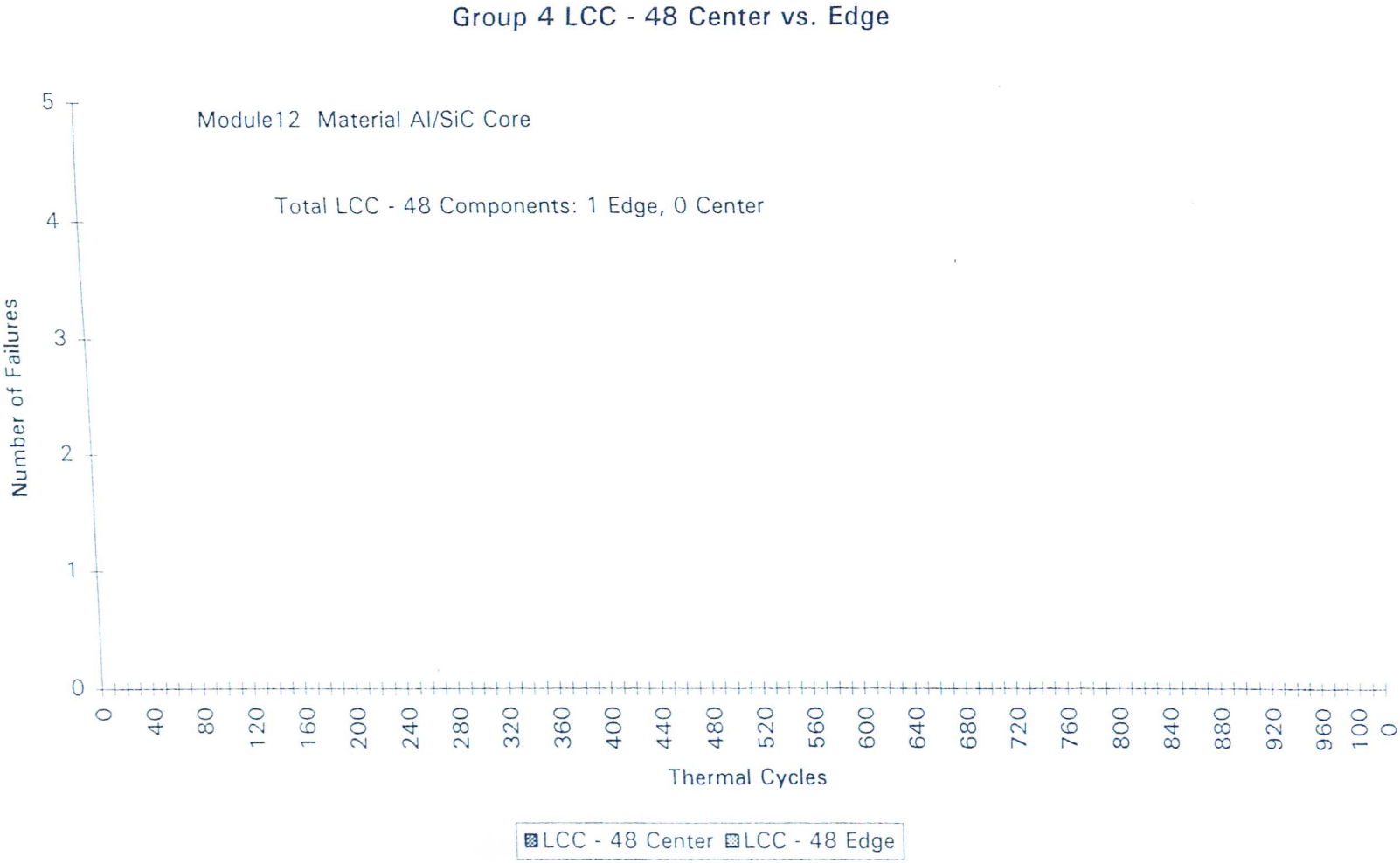
Group 3 LCC - 48 Center vs. Edge



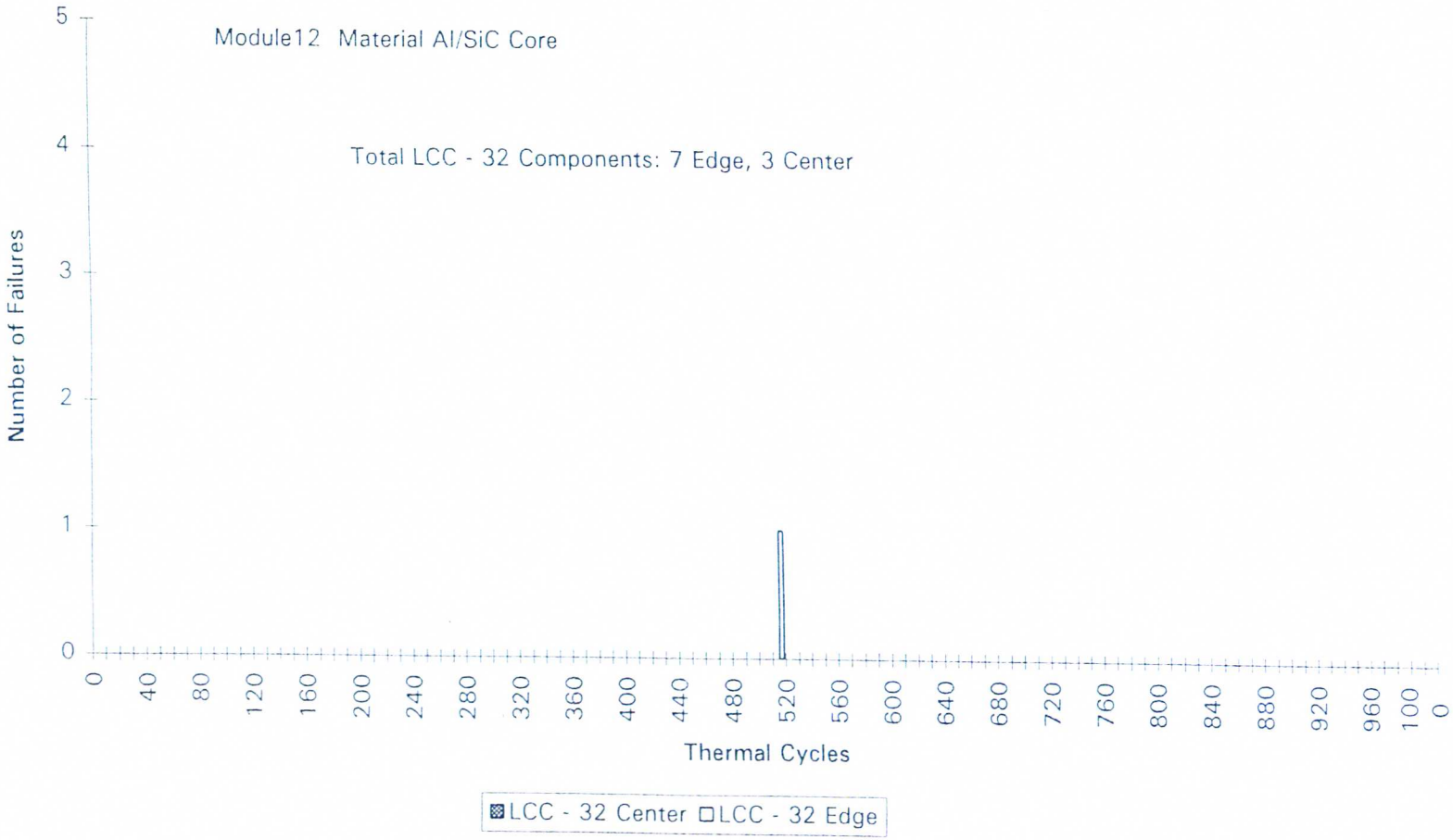
Group 3 LCC - 32 Center vs. Edge

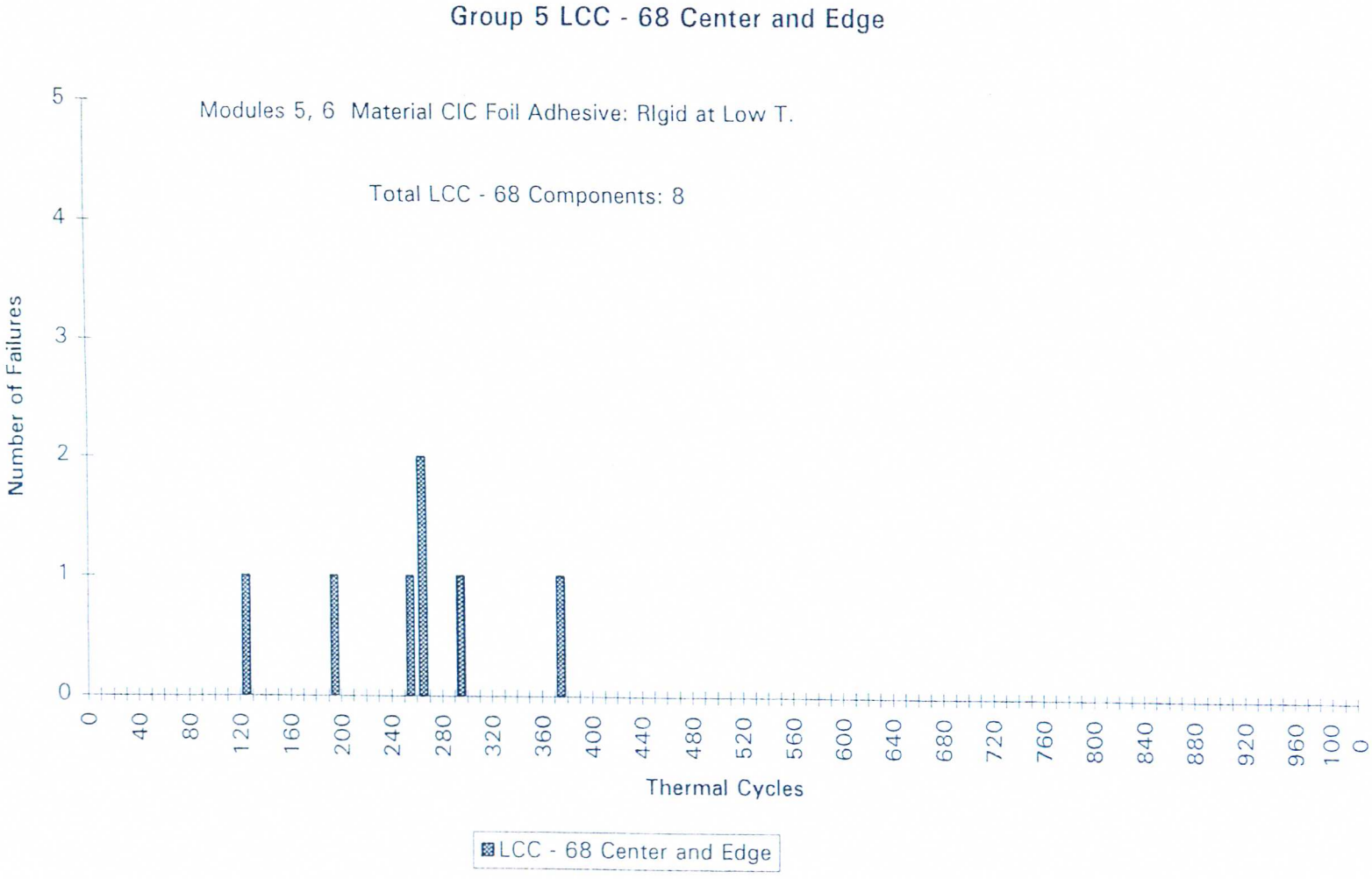


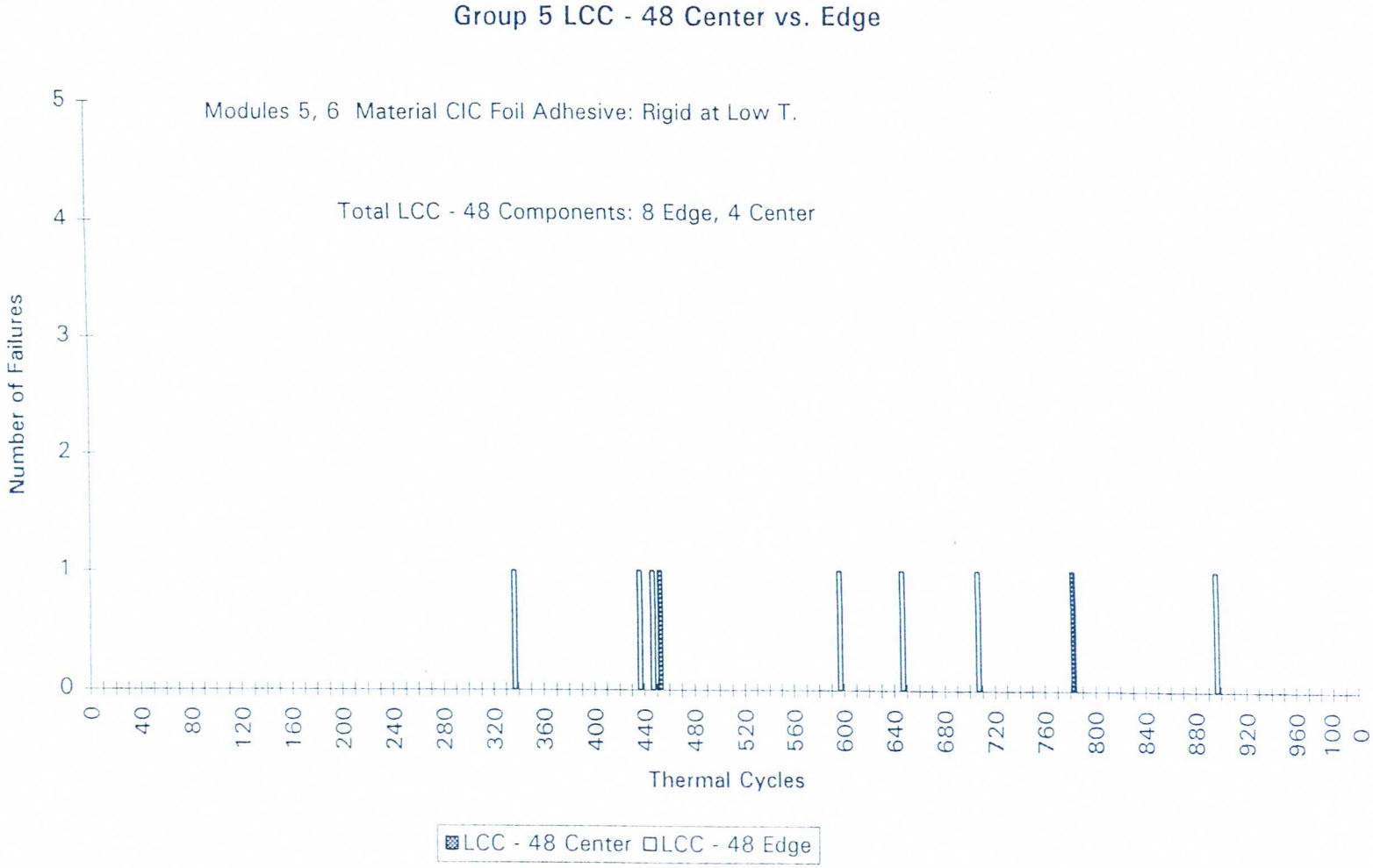

Group 4 LCC - 68 Center and Edge
Module12 Material Al/SiC Core
Total LCC - 68 Components: 4
Number of Failures
0
1
2
3
4
5
0
40
80
120
160
200
240
280
320
360
400
440
480
520
560
600
640
680
720
760
800
840
880
920
960
1000
Thermal Cycles
LCC - 68 Center and Edge


Group 4 LCC - 48 Center vs. Edge
Module12 Material Al/SiC Core
Total LCC - 48 Components: 1 Edge, 0 Center
Number of Failures
0
1
2
3
4
5
0
40
80
120
160
200
240
280
320
360
400
440
480
520
560
600
640
680
720
760
800
840
880
920
960
100
0
Thermal Cycles
LCC - 48 Center
LCC - 48 Edge

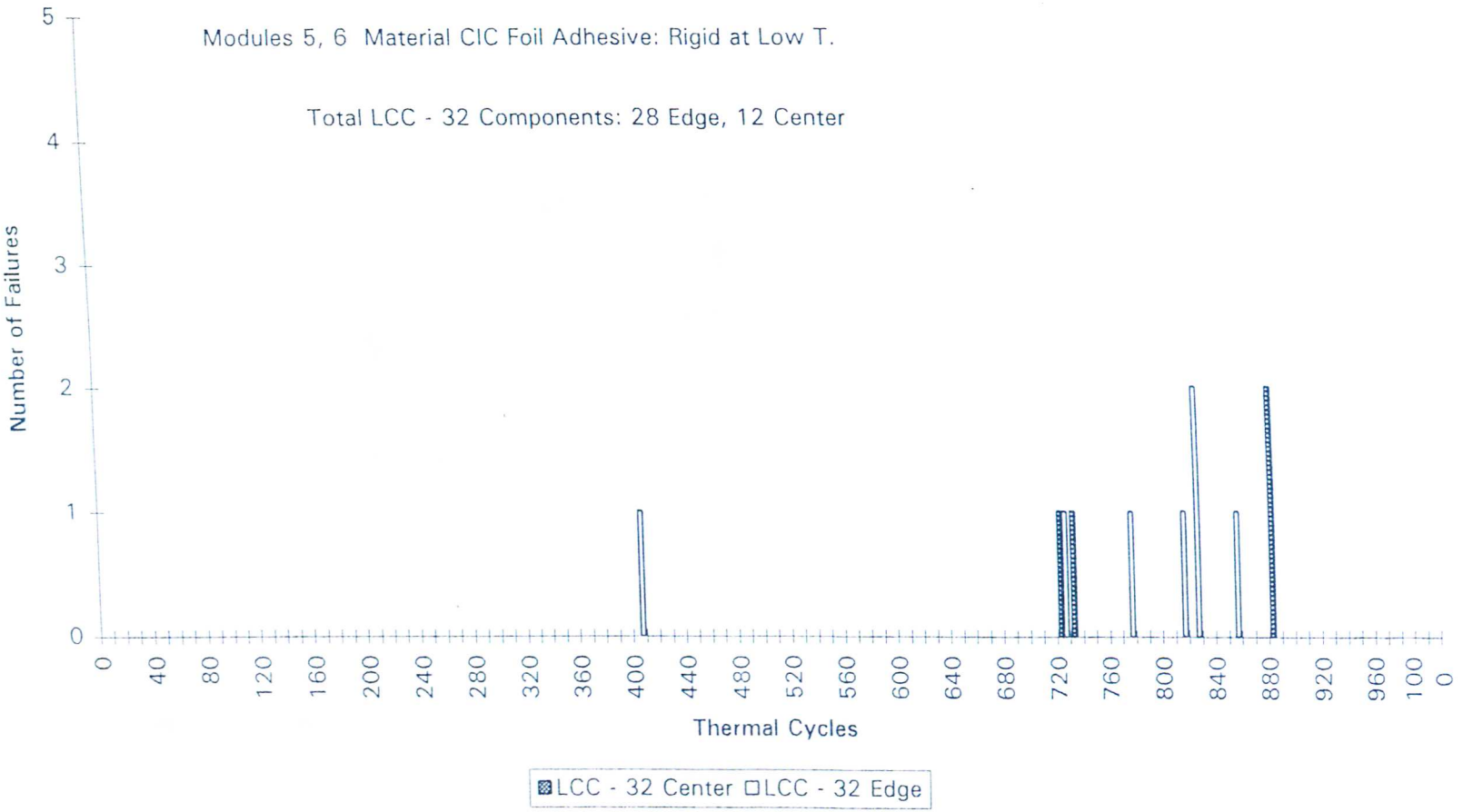
Group 4 LCC - 32 Center vs. Edge

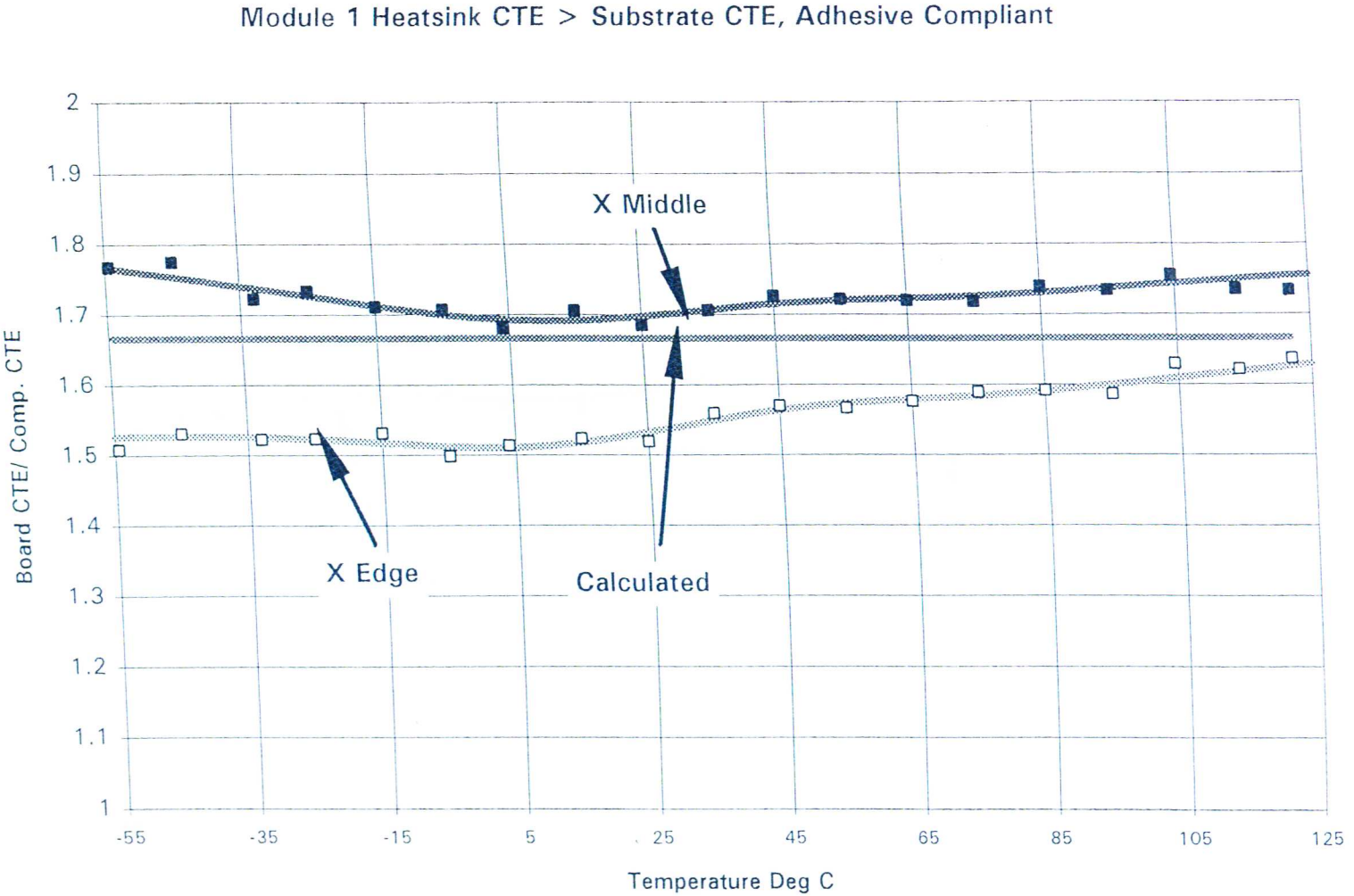



Group 5 LCC - 68 Center and Edge
Modules 5, 6 Material CIC Foil Adhesive: Rlgid at Low T.
Total LCC - 68 Components: 8
Number of Failures
0
1
2
3
4
5
0
40
80
120
160
200
240
280
320
360
400
440
480
520
560
600
640
680
720
760
800
840
880
920
960
100
0
Thermal Cycles
LCC - 68 Center and Edge

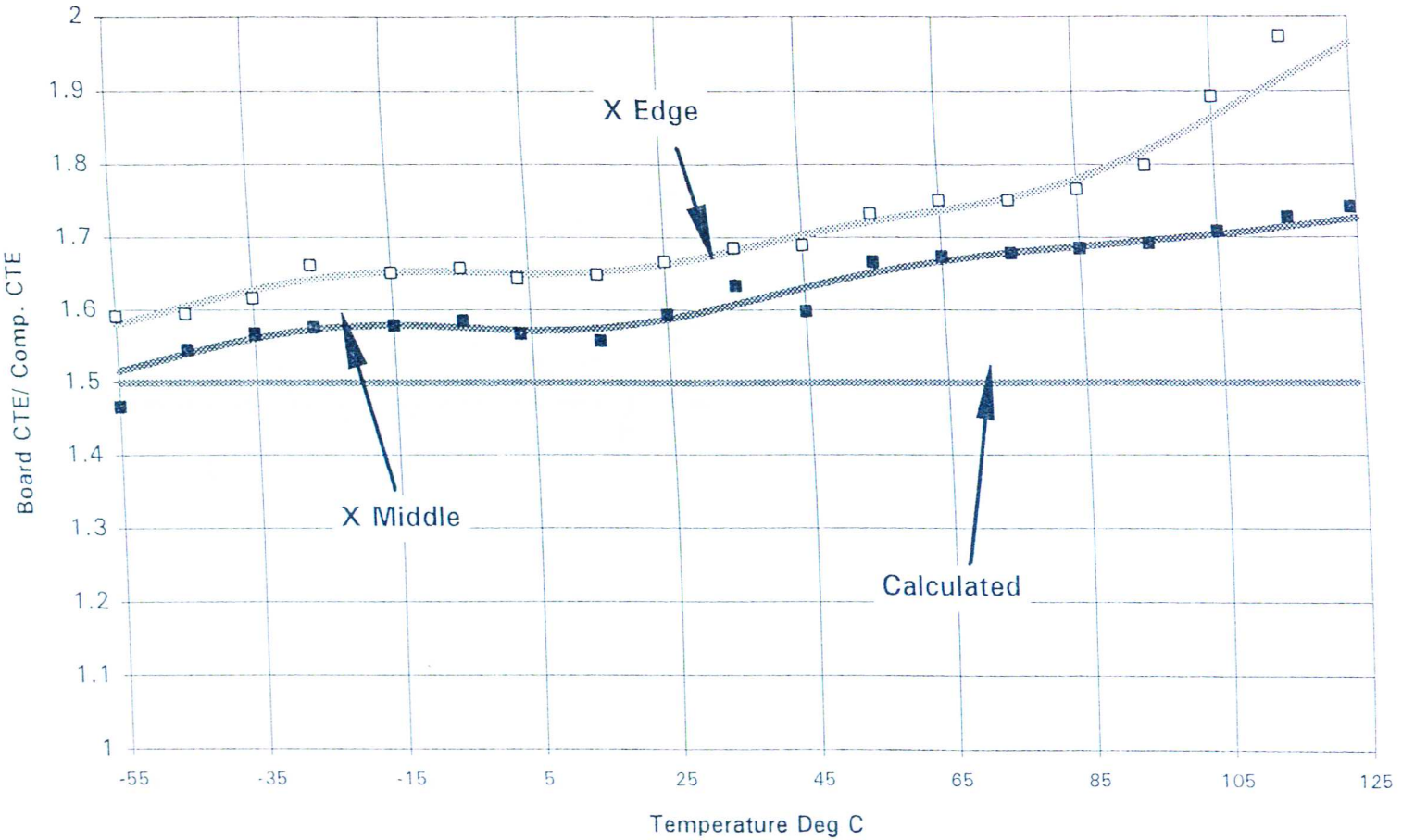

Group 5 LCC - 48 Center vs. Edge
Modules 5, 6 Material CIC Foil Adhesive: Rigid at Low T.
Total LCC - 48 Components: 8 Edge, 4 Center
Number of Failures
0
1
2
3
4
5
0
40
80
120
160
200
240
280
320
360
400
440
480
520
560
600
640
680
720
760
800
840
880
920
960
1000
Thermal Cycles
LCC - 48 Center
LCC - 48 Edge

Group 5 LCC - 32 Center vs. Edge

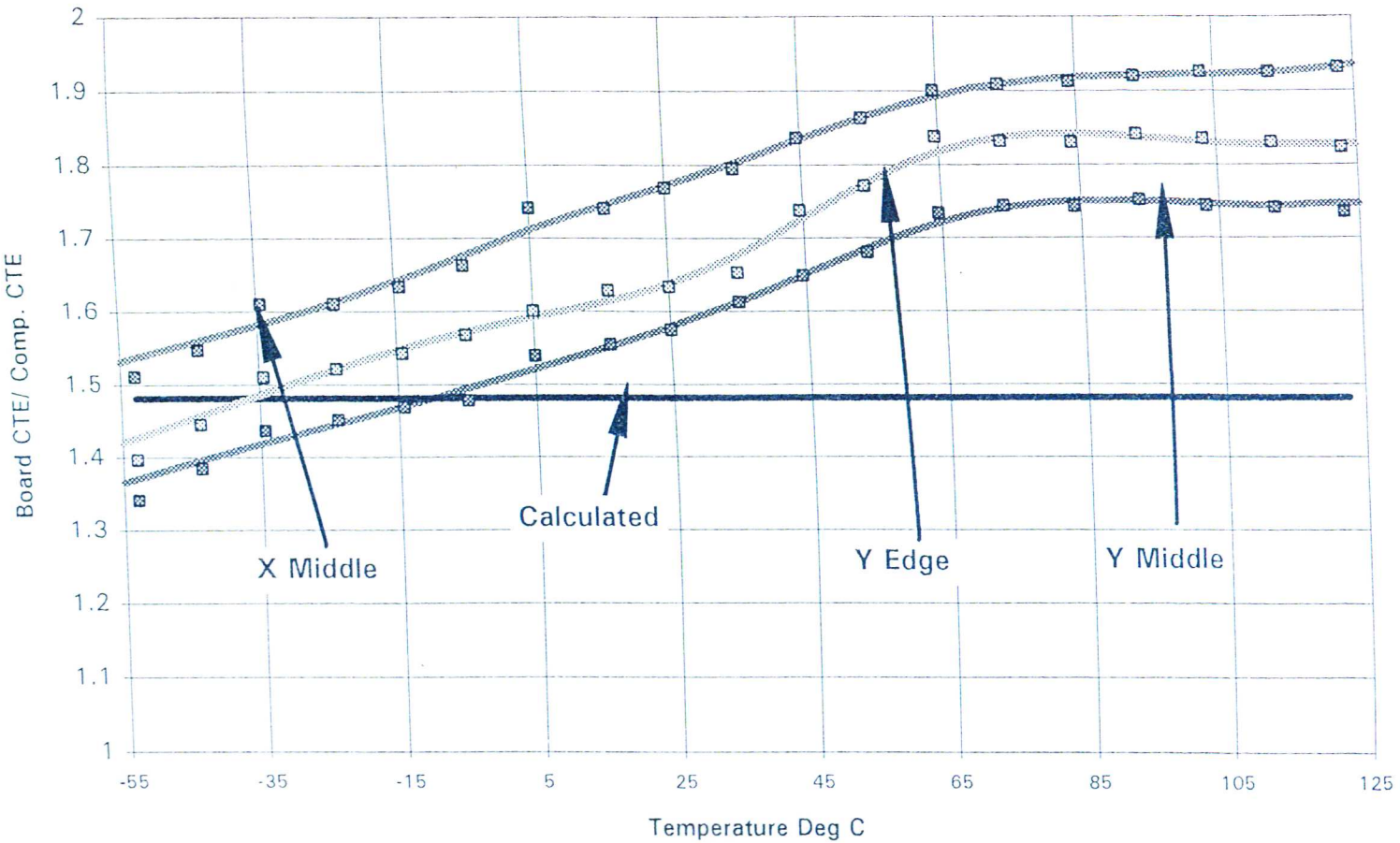


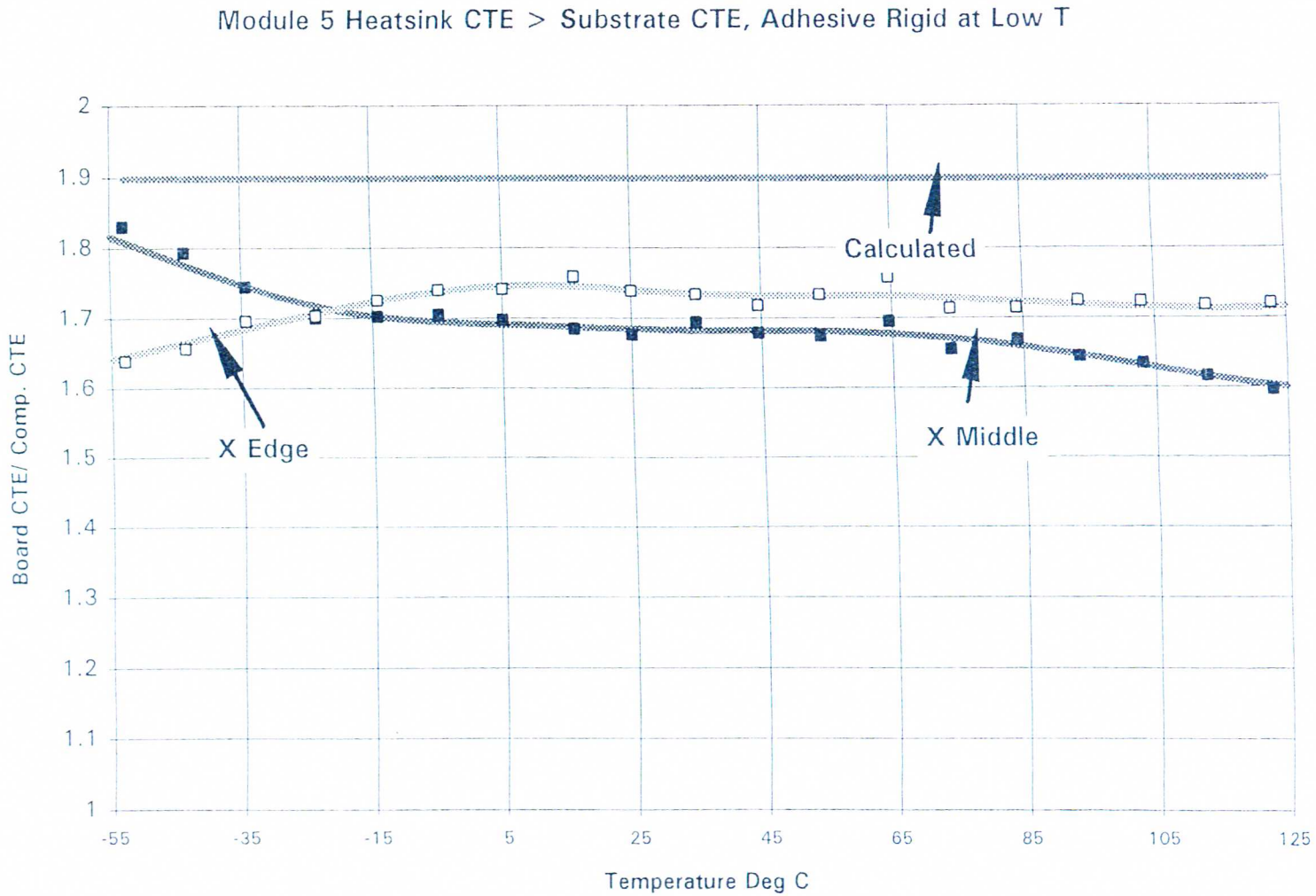

Module 1 Heatsink CTE > Substrate CTE, Adhesive Compliant
Board CTE/ Comp. CTE
2
1.9
1.8
1.7
1.6
1.5
1.4
1.3
1.2
1.1
1
X Middle
X Edge
Calculated
-55
-35
-15
5
25
45
65
85
105
125
Temperature Deg C

Module 3 Heatsink CTE < Substrate CTE, Adhesive Compliant

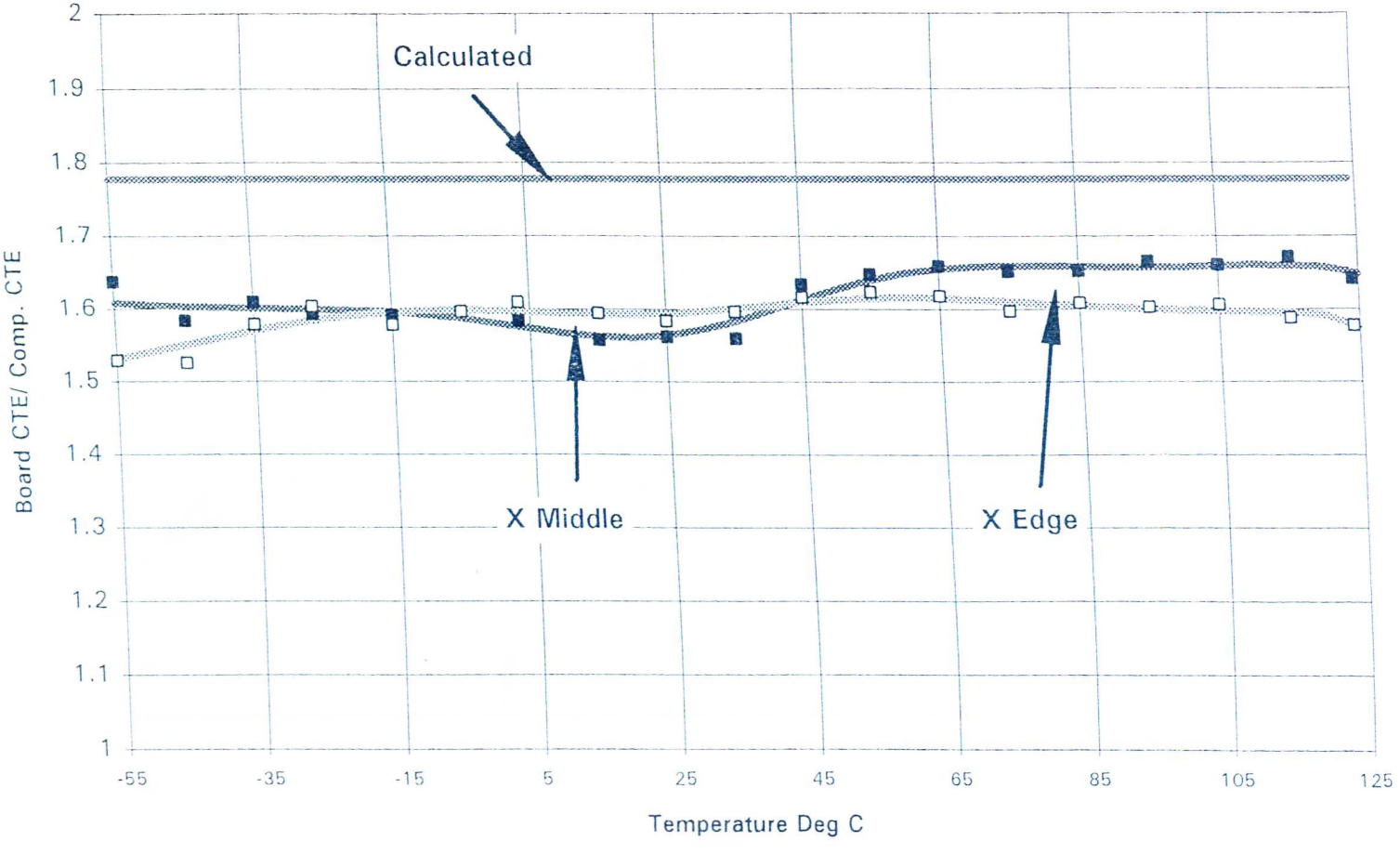


Module 4A Heatsink CTE < Substrate CTE, Adhesive Rigid

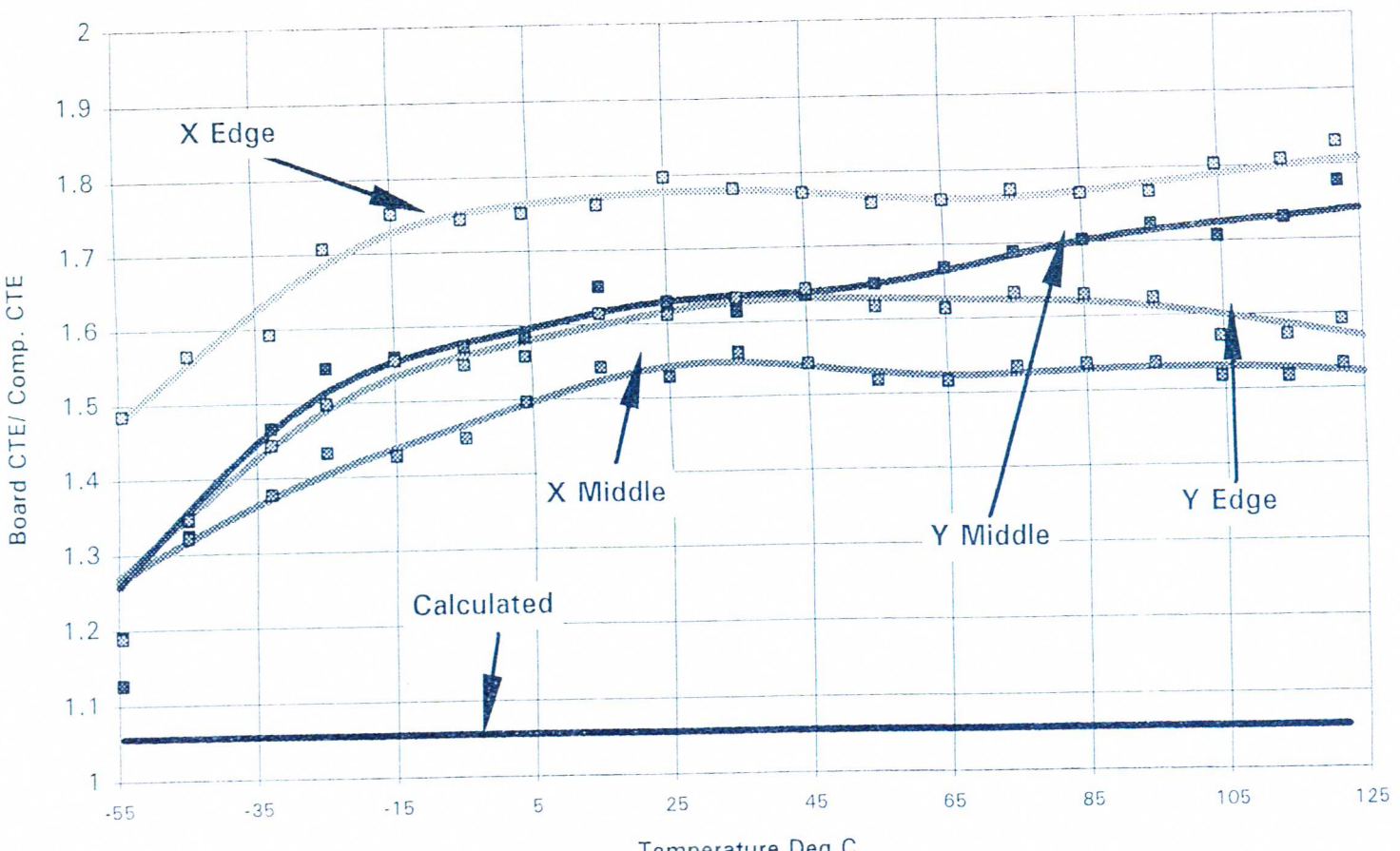


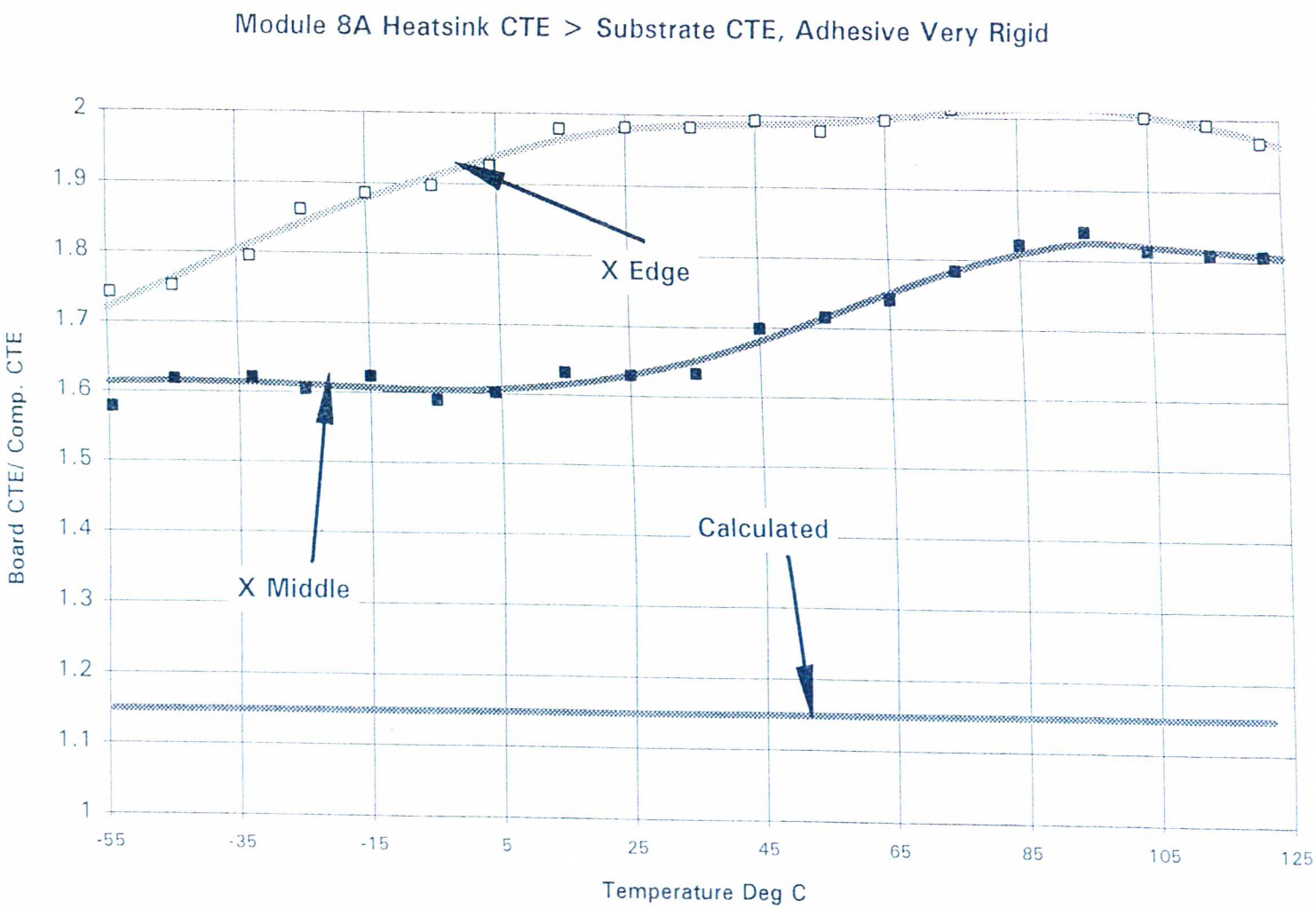

Module 5 Heatsink CTE > Substrate CTE, Adhesive Rigid at Low T
Board CTE/ Comp. CTE
2
1.9
1.8
1.7
1.6
1.5
1.4
1.3
1.2
1.1
1
-55
-35
-15
5
25
45
65
85
105
125
Temperature Deg C
Calculated
X Edge
X Middle

Module 7 Heatsink CTE > Substrate CTE, Adhesive Compliant

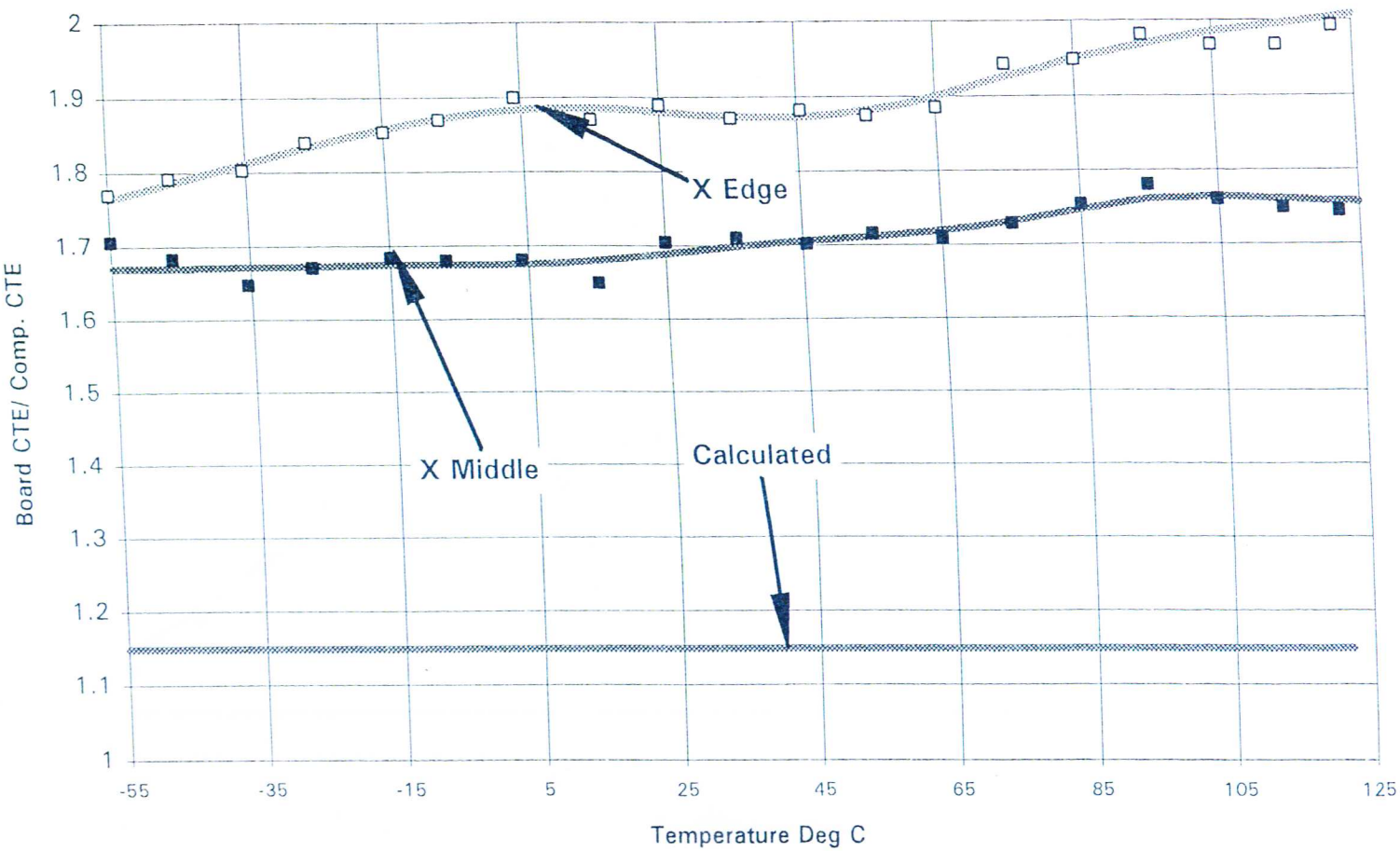


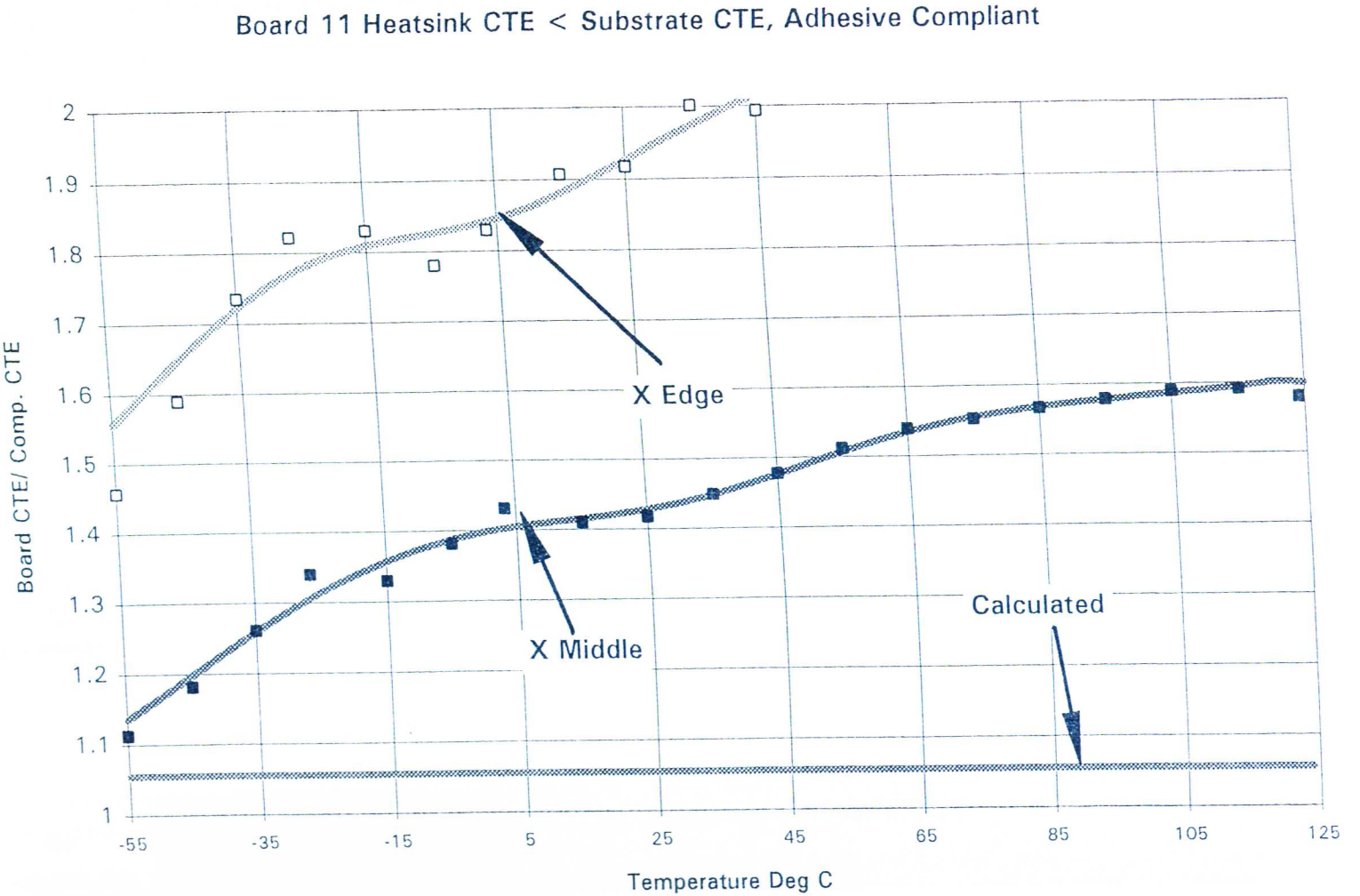
Module 9 Heatsink CTE < Substrate CTE, Adhesive Compliant for All T




Module 8A Heatsink CTE > Substrate CTE, Adhesive Very Rigid
Board CTE/ Comp. CTE
2
1.9
1.8
1.7
1.6
1.5
1.4
1.3
1.2
1.1
1
-55
-35
-15
5
25
45
65
85
105
125
Temperature Deg C
X Edge
X Middle
Calculated

Module 10 Heatsink CTE > Substrate CTE, Adhesive Compliant




Board 11 Heatsink CTE < Substrate CTE, Adhesive Compliant
Board CTE/ Comp. CTE
2
1.9
1.8
1.7
1.6
1.5
1.4
1.3
1.2
1.1
1
-55
-35
-15
5
25
45
65
85
105
125
Temperature Deg C
X Edge
X Middle
Calculated

Group	1	2	3	4	5	6	7	8	9&10	11&12	13	14	15
%γ													
$\Delta\gamma=\Delta\alpha\Delta T_{Ld}/2h$	2.00%	2.60%	2.80%	2.92%	3.05%	3.20%	3.42%	3.55%	3.85%	4.50%	5.70%	6.30%	7.40%
		648	269	347	402	226	338	479	63	156	123	288	460
		708	324	453	546	459	431	541	410	157	194	353	509
		727	347	500	728	719	449	565	855	179	252	357	634
		751	392	619	772	754	590	589	860	196	261	516	787
		784	422	666	772	789	645	645		216	262	524	
		805	435	676	819	24	701	854		218	269	568	
		860	443	728	823		890			245	299	620	
		860	456	734	826					259	343		
		864	475	742	851					264	376		
		888	500	750						280	435		
		894	503	882						295	485		
			516	887						296	495		
			519	893						296	852		
			545							299	870		
			617							310			
			743							312			
										859			
# Failed	0	11	16	13	9	6	7	6	4	17	14	7	4
# Censored at 1000	8	64	18	31	22	58	15	10	56	15	2	1	12
# In Group	8	75	34	44	31	64	22	16	60	32	16	8	16

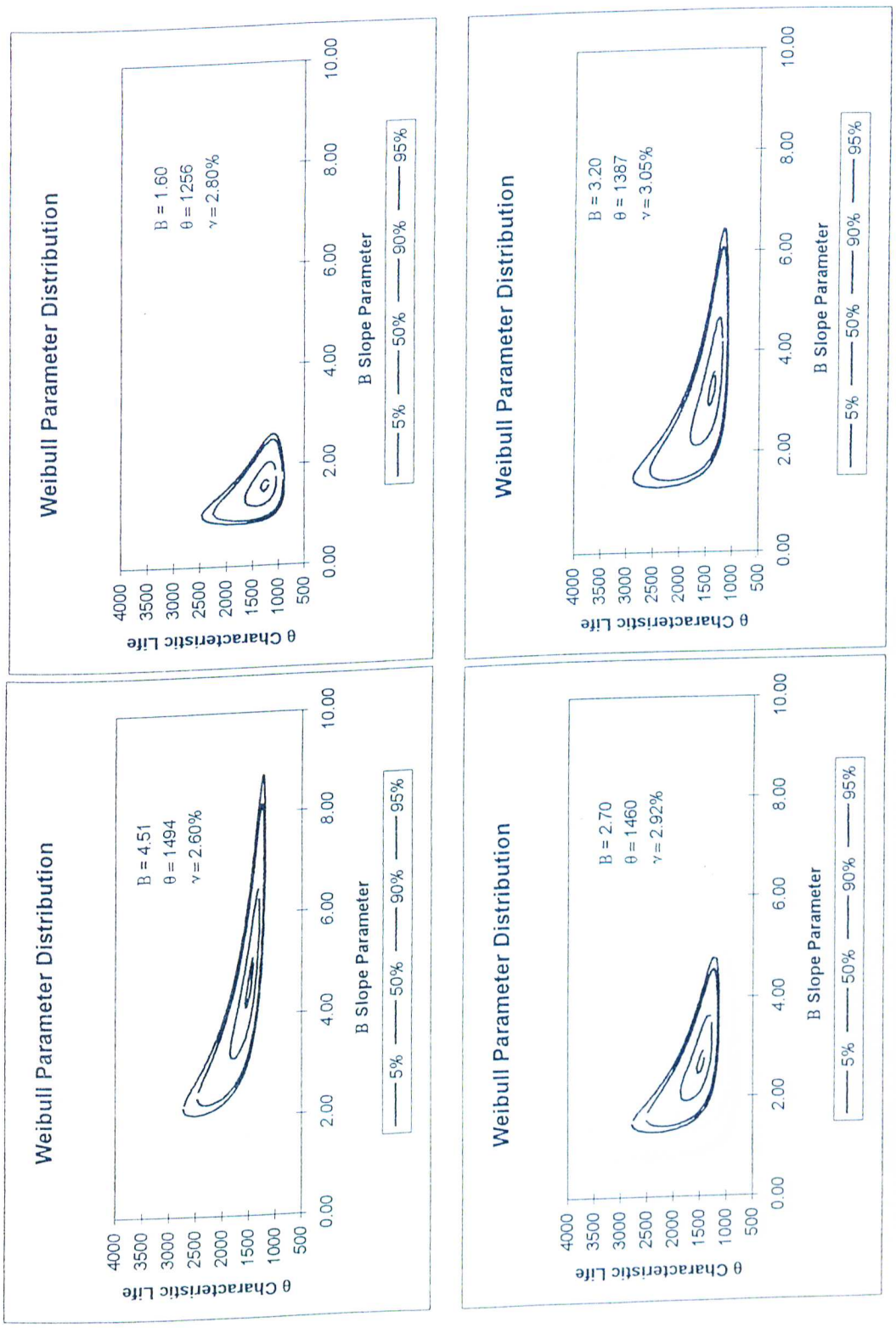
	Group 1	Group 2	Group 3	4	5	6	7	8	9&10	11&12	13	14	15
%γ													
$\Delta\gamma=\Delta\alpha\Delta T_{Ld}/2h$	2.00%	2.60%	2.80%	2.92%	3.05%	3.20%	3.42%	3.55%	3.85%	4.50%	5.70%	6.30%	7.40%
% Failed	00.0%	14.7%	47.1%	29.5%	29.0%	09.4%	31.8%	37.5%	06.7%	53.1%	87.5%	87.5%	25.0%

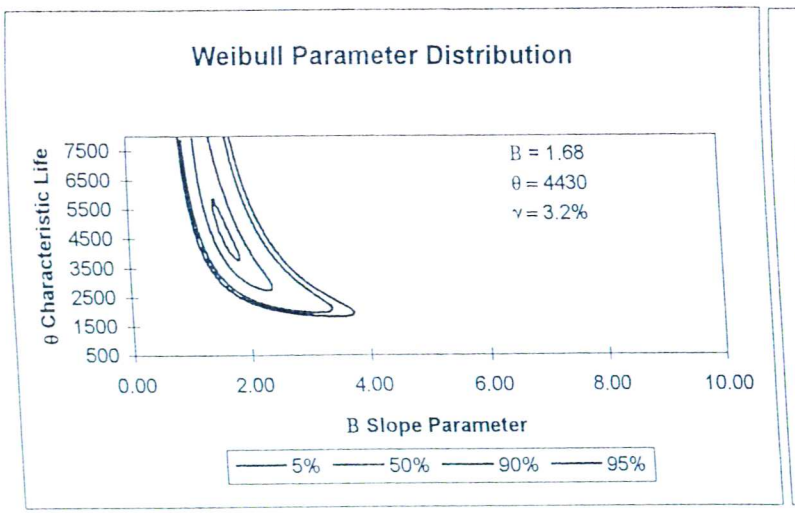
Appendix F Algorithm to Compute Confidence Contours on Distribution Parameter

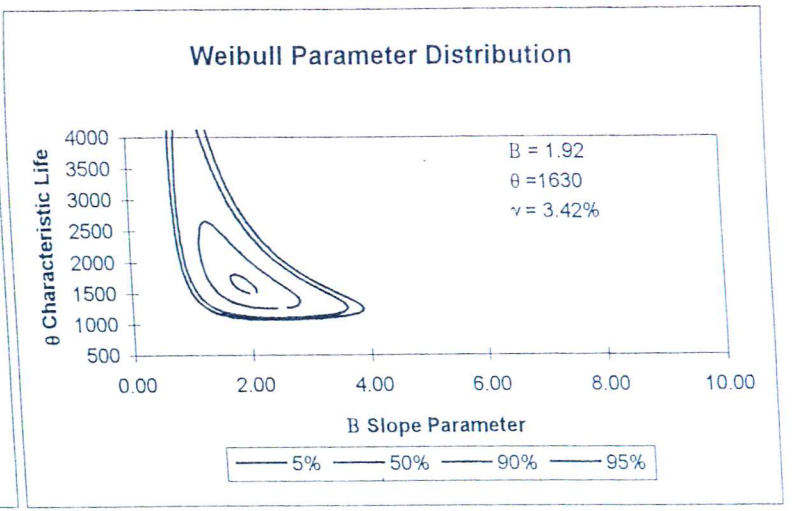
The confidence contours are computed as follows:

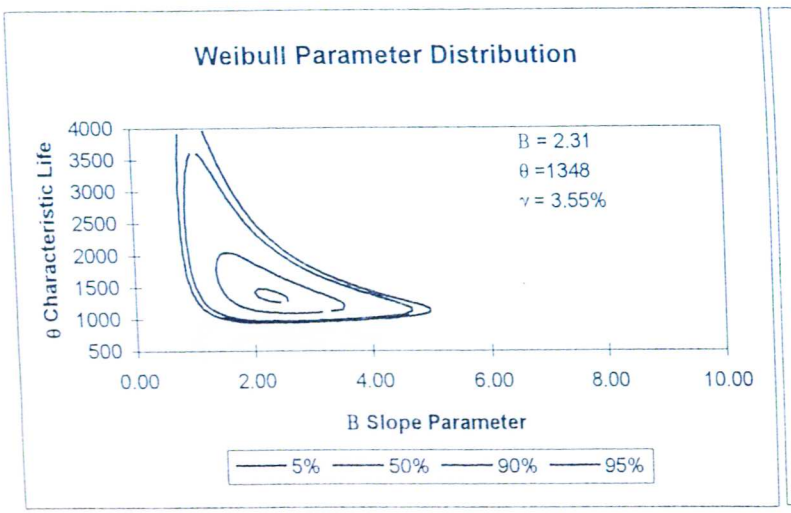
1. Determine the contours at arbitrary altitudes . Approximately 20 contours is sufficient for numerical accuracy
2. Compute the area enclosed in each couture, this is the area of the projection of the probability density contours on the θ-B plane.
3. Compute the volume above each contour
4. Add the volume computed in step 3 to the area of the contour calculated in step 2 multiplied times the altitude of the contour. This is the volume inside the confidence contour.
5. Interpolations between the calculated contours and the desired contour intervals gives the altitudes at the desired confidence level. Confidence levels of 95%, 90%, 50% and 5% are used for this study
6. Determine the contours at the altitudes determined in step 5.

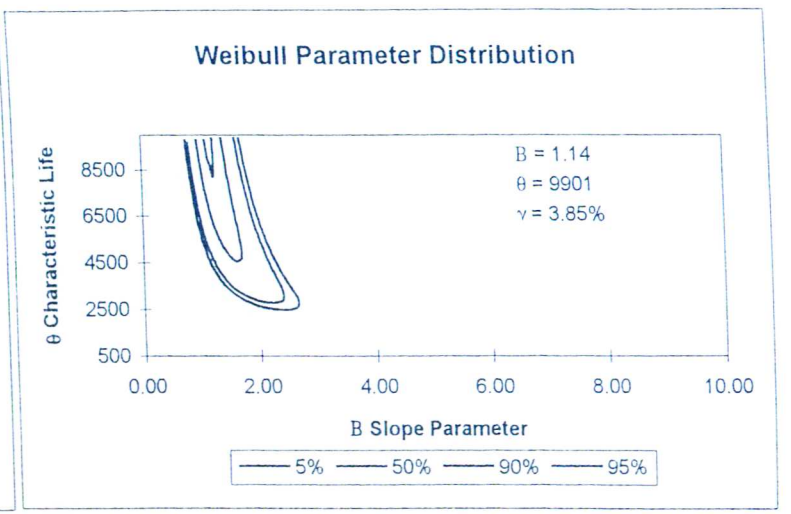
Appendix G Weibull Posterior Parameter Distribution at at Differnet Strain Levels

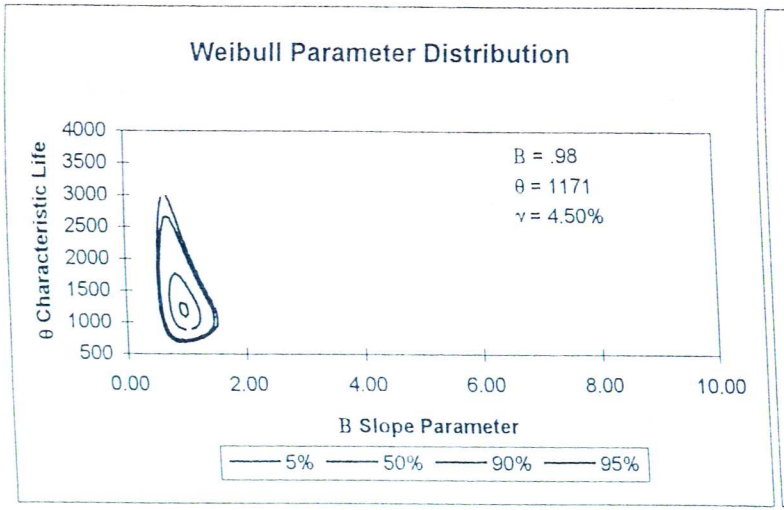


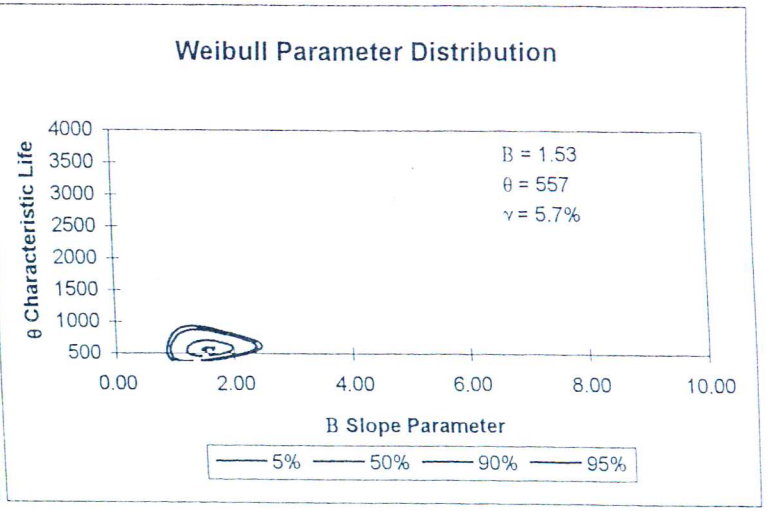

Weibull Parameter Distribution
θ Characteristic Life
7500
6500
5500
4500
3500
2500
1500
500
0.00
2.00
4.00
6.00
8.00
10.00
B Slope Parameter
B = 1.68
θ = 4430
γ = 3.2%
5%
50%
90%
95%

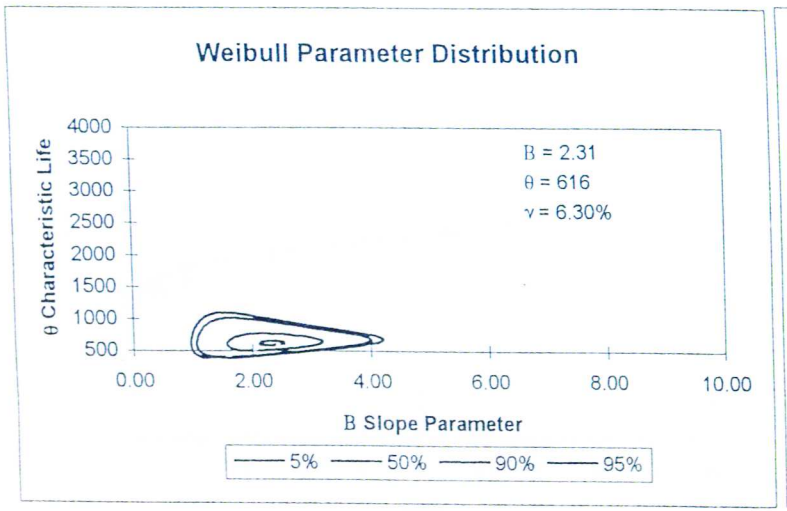

Weibull Parameter Distribution
θ Characteristic Life
4000
3500
3000
2500
2000
1500
1000
500
0.00
2.00
4.00
6.00
8.00
10.00
B Slope Parameter
B = 1.92
θ =1630
γ = 3.42%
5%
50%
90%
95%

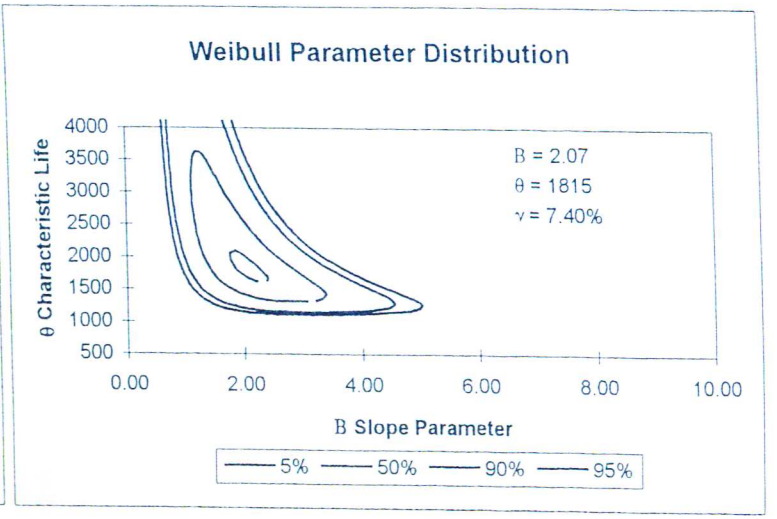

Weibull Parameter Distribution
θ Characteristic Life
4000
3500
3000
2500
2000
1500
1000
500
0.00
2.00
4.00
6.00
8.00
10.00
B Slope Parameter
B = 2.31
θ =1348
γ = 3.55%
5%
50%
90%
95%


Weibull Parameter Distribution
θ Characteristic Life
8500
6500
4500
2500
500
0.00
2.00
4.00
6.00
8.00
10.00
B Slope Parameter
B = 1.14
θ = 9901
γ = 3.85%
5%
50%
90%
95%

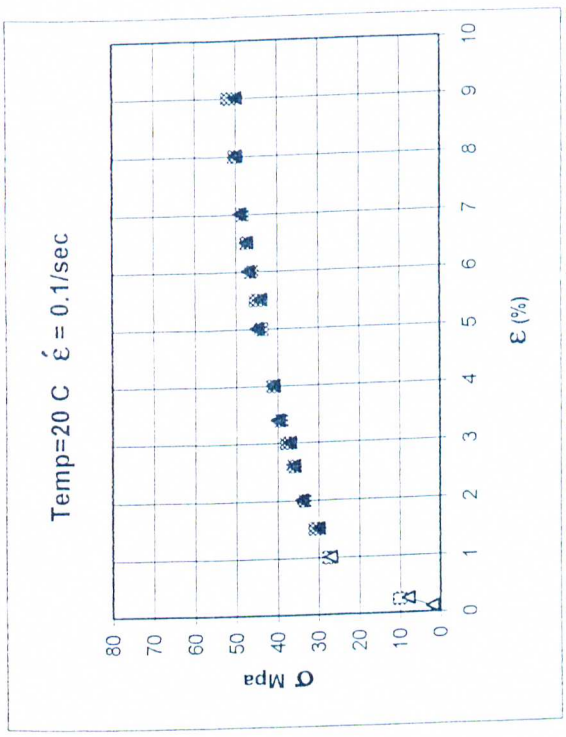

Weibull Parameter Distribution
θ Characteristic Life
4000
3500
3000
2500
2000
1500
1000
500
0.00
2.00
4.00
6.00
8.00
10.00
B Slope Parameter
B = .98
θ = 1171
ν = 4.50%
5%
50%
90%
95%

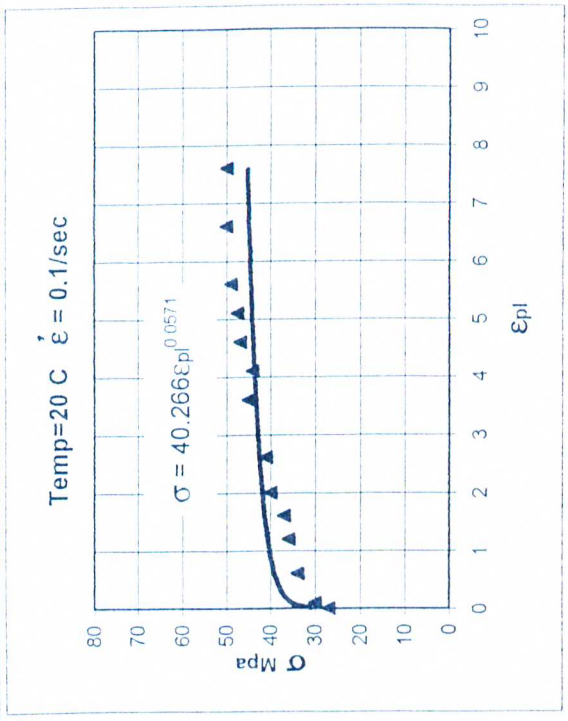

Weibull Parameter Distribution
θ Characteristic Life
4000
3500
3000
2500
2000
1500
1000
500
0.00
2.00
4.00
6.00
8.00
10.00
B Slope Parameter
B = 1.53
θ = 557
ν = 5.7%
5%
50%
90%
95%

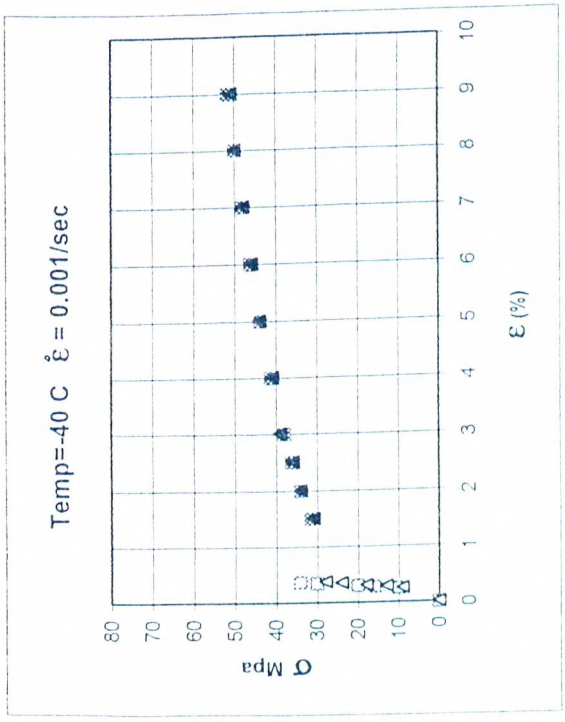

Weibull Parameter Distribution
θ Characteristic Life
4000
3500
3000
2500
2000
1500
1000
500
0.00
2.00
4.00
6.00
8.00
10.00
B Slope Parameter
B = 2.31
θ = 616
ν = 6.30%
5%
50%
90%
95%

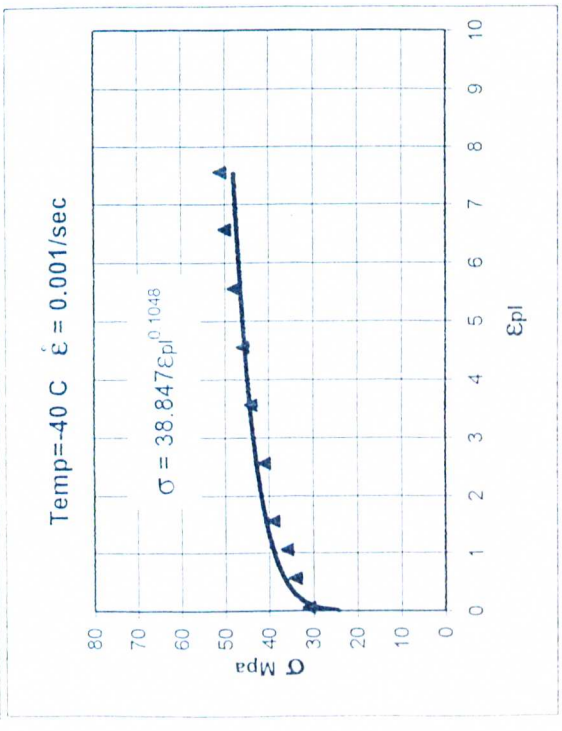

Weibull Parameter Distribution
θ Characteristic Life
4000
3500
3000
2500
2000
1500
1000
500
0.00
2.00
4.00
6.00
8.00
10.00
B Slope Parameter
B = 2.07
θ = 1815
ν = 7.40%
5%
50%
90%
95%

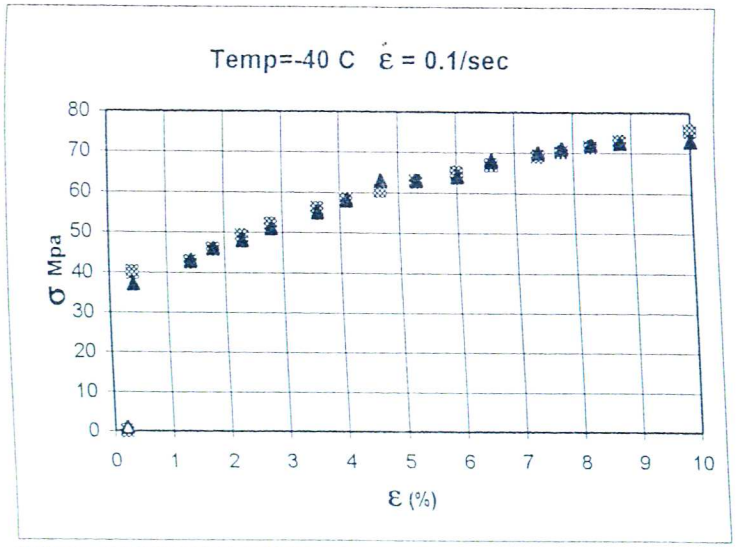
Appendix H Plastic Constitutive Model Constants at Different Temperatures and Strain rates

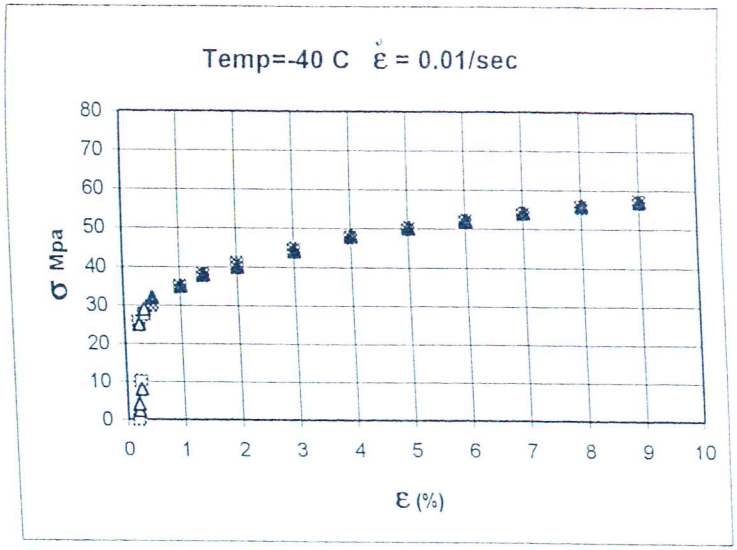


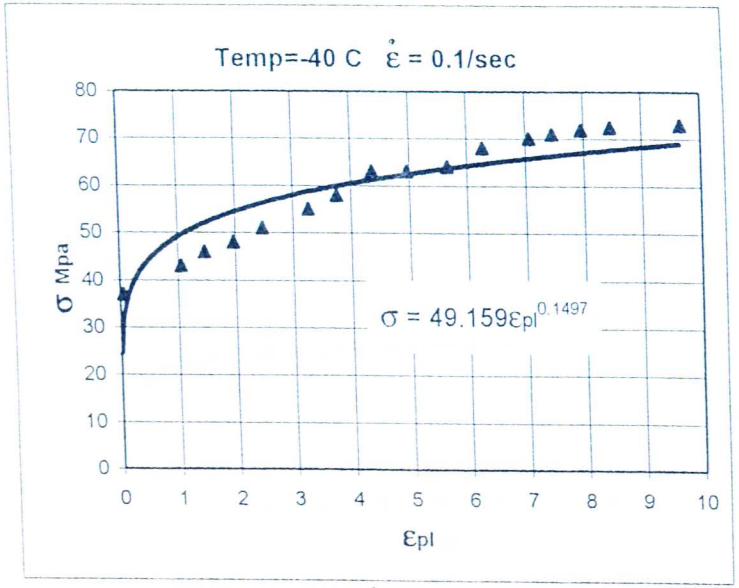


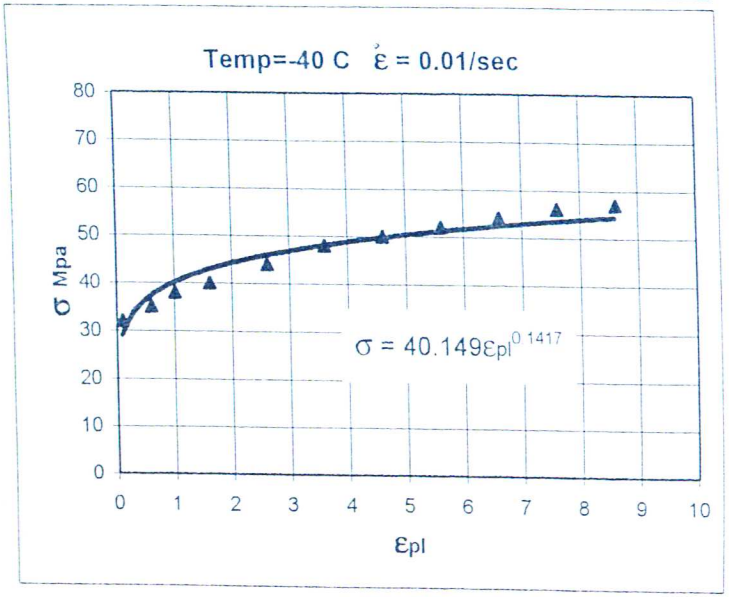


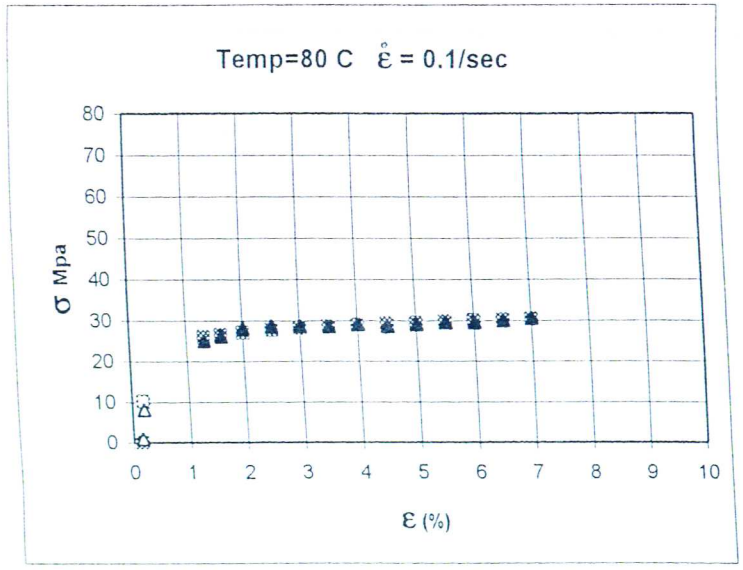


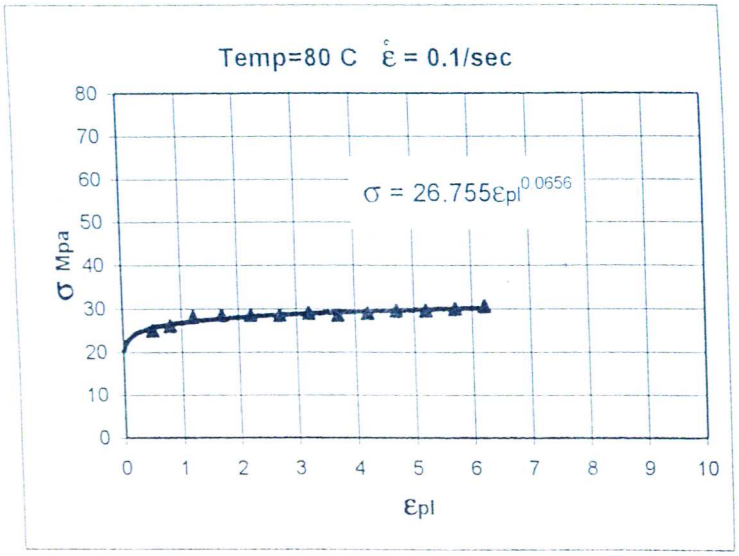

Temp=-40 C $\dot{\varepsilon}$ = 0.1/sec
σ Mpa
ε (%)

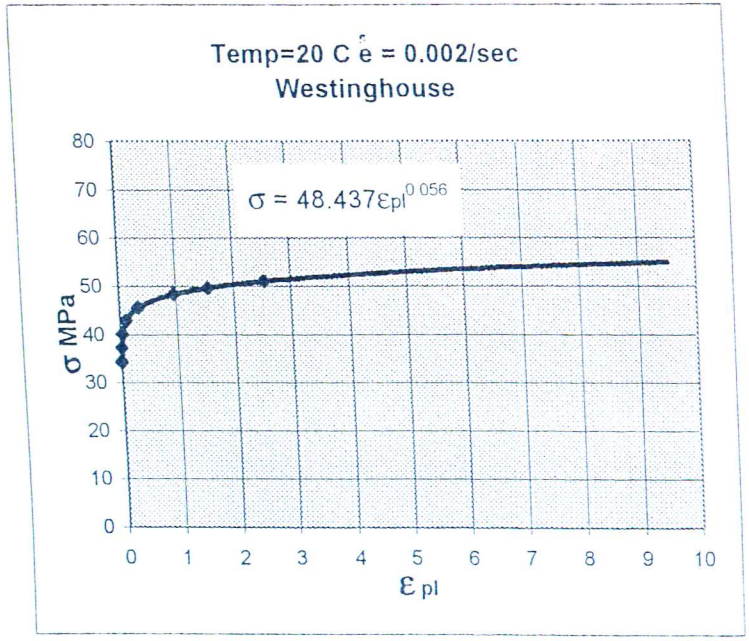

Temp=-40 C $\dot{\varepsilon}$ = 0.01/sec
σ Mpa
ε (%)


Temp=-40 C $\dot{\varepsilon}$ = 0.1/sec
σ = 49.159εpl^0.1497
σ Mpa
εpl


Temp=-40 C $\dot{\varepsilon}$ = 0.01/sec
σ = 40.149εpl^0.1417
σ Mpa
εpl


Temp=80 C $\dot{\varepsilon}$ = 0.1/sec
σ Mpa
ε (%)


Temp=80 C $\dot{\varepsilon}$ = 0.1/sec
$\sigma = 26.755\varepsilon_{pl}^{0.0656}$
σ Mpa
εpl


Temp=20 C $\dot{\varepsilon}$ = 0.002/sec
Westinghouse
$\sigma = 48.437\varepsilon_{pl}^{0.056}$
σ MPa
ε pl

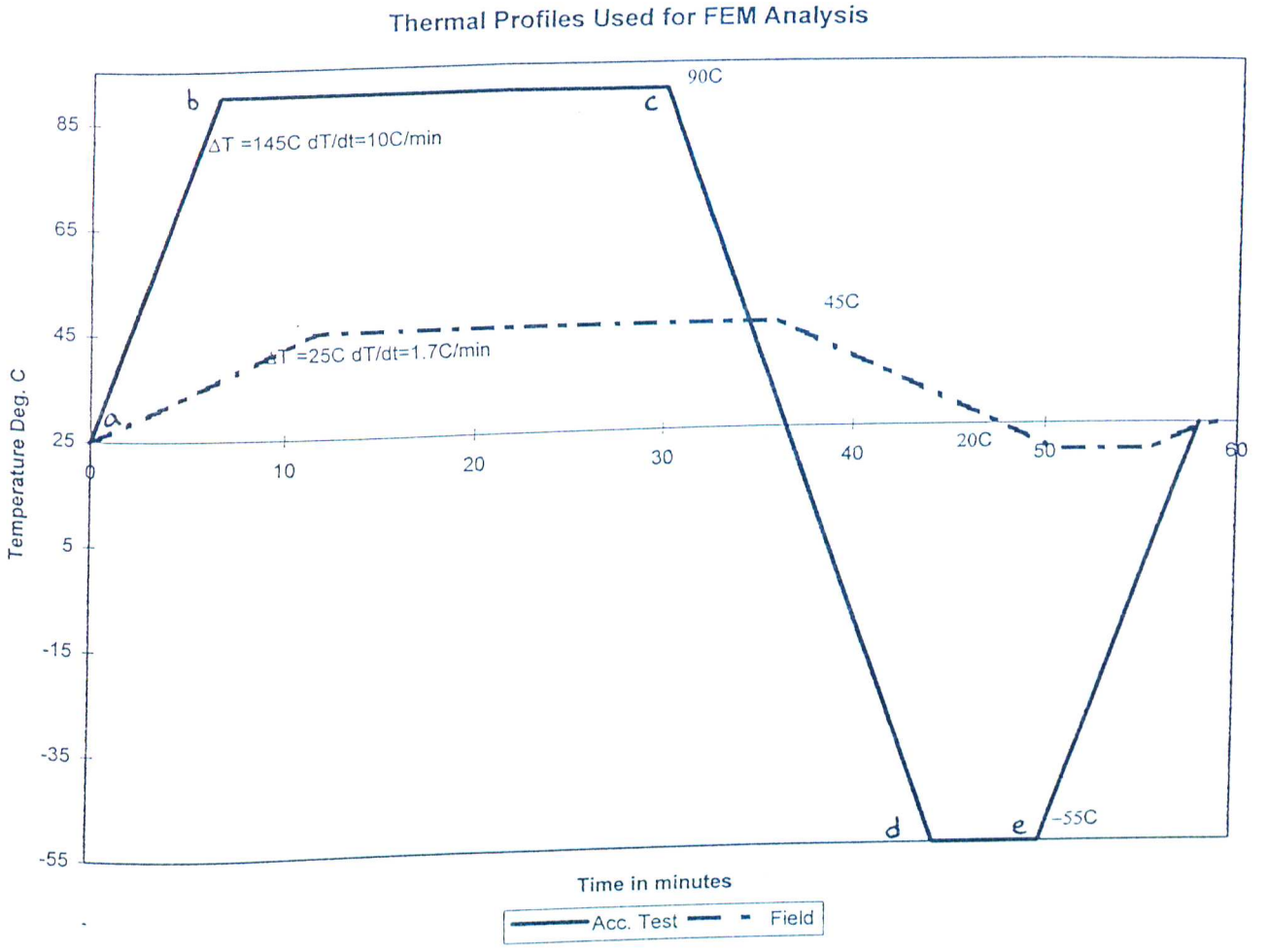
	Pitch (all units mils)	Bond Pad Length	Bond Pad Height	Castelation Width	Castelation Height
LCC-48	40	80	0.5	6	45
LCC-68, 32	50	80	0.5	8	45

	Component Height	Cu-W Comp. Pad Length	Front Over Hang	Component Length Ld/2	Rear Over Hang
LCC-48	45	40	33	396	7
LCC-68, 32	45	50	33	672, 365	-3

Material	In Plane CTE ppm/C	In Plane Modulus 10E+6psi	Out of Plane Modulus 10E+6psi	ν_{xy}	ν_{yz}	ν_{zx}
Copper Electro Deposited	16.7*	12.0*	12.0*	.34*	.34*	.34*
Copper Tungsten	5.4*	10.4*	10.4*	.17*	.17*	.17*
60Pb-40Sn Solder	23.9	4.34	4.34	0.4	0.4	0.4
Ceramic	5.4	54.97***	54.97***	0.21***	0.21***	0.21***
Substrate	6-10	4	4	0.12	0.3	0.14

Substrate height
80 mils

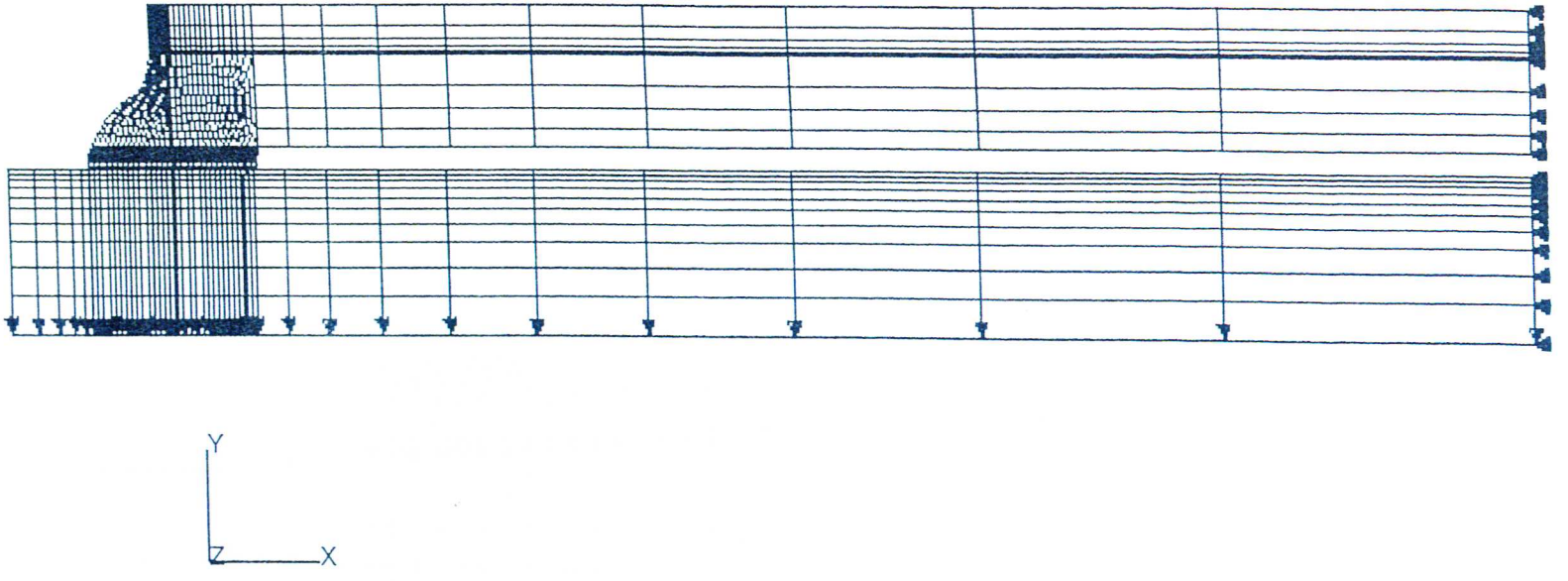
* CALCE Database
*** Papers Verma, Das,...
Otherwise measured by Hamilton Standard

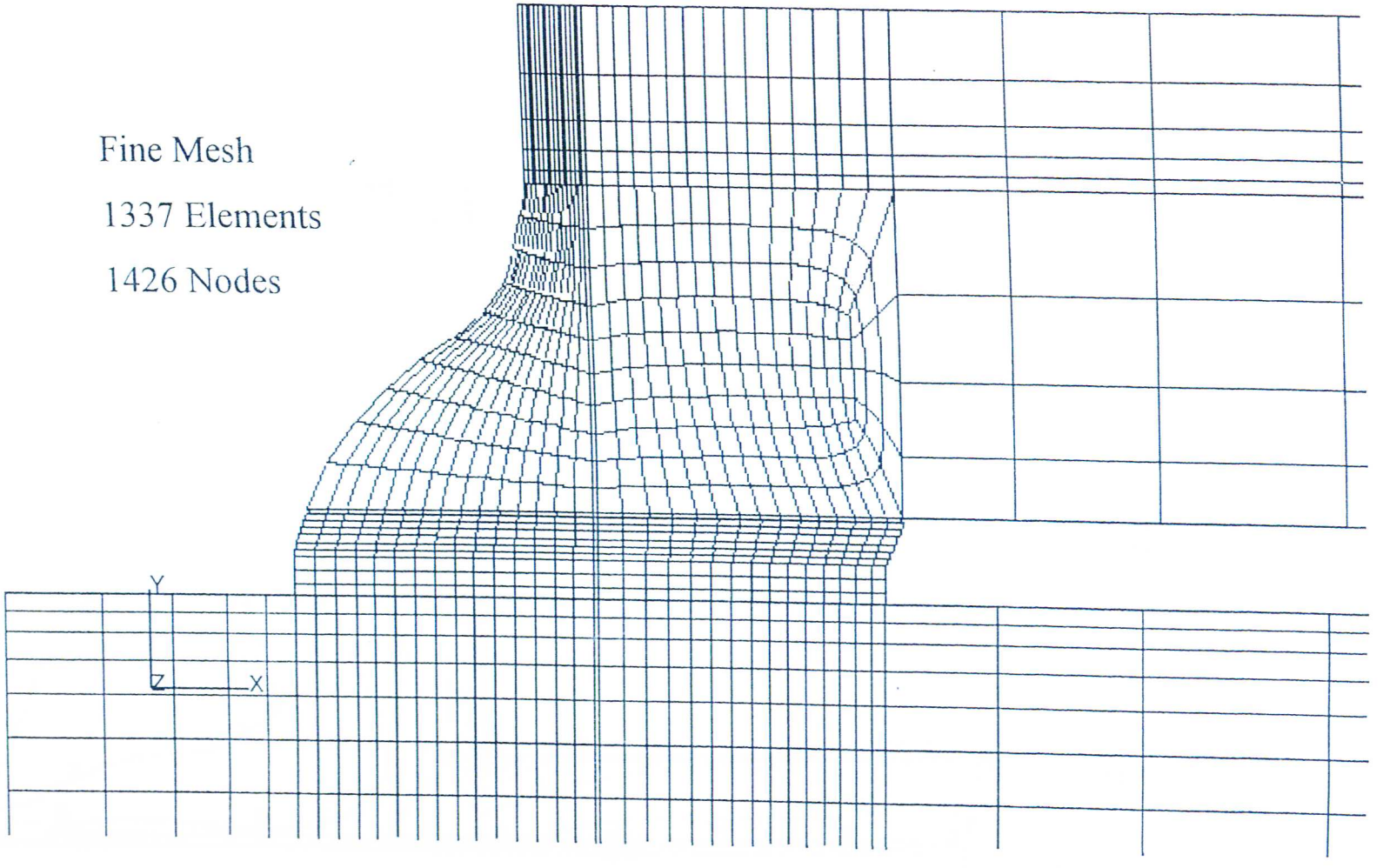

Thermal Profiles Used for FEM Analysis
90C
b
c
85
ΔT =145C dT/dt=10C/min
65
45C
45
ΔT =25C dT/dt=1.7C/min
a
25
20C
0
10
20
30
40
50
60
5
-15
-35
-55
d
e
-55C
Temperature Deg. C
Time in minutes
Acc. Test
Field

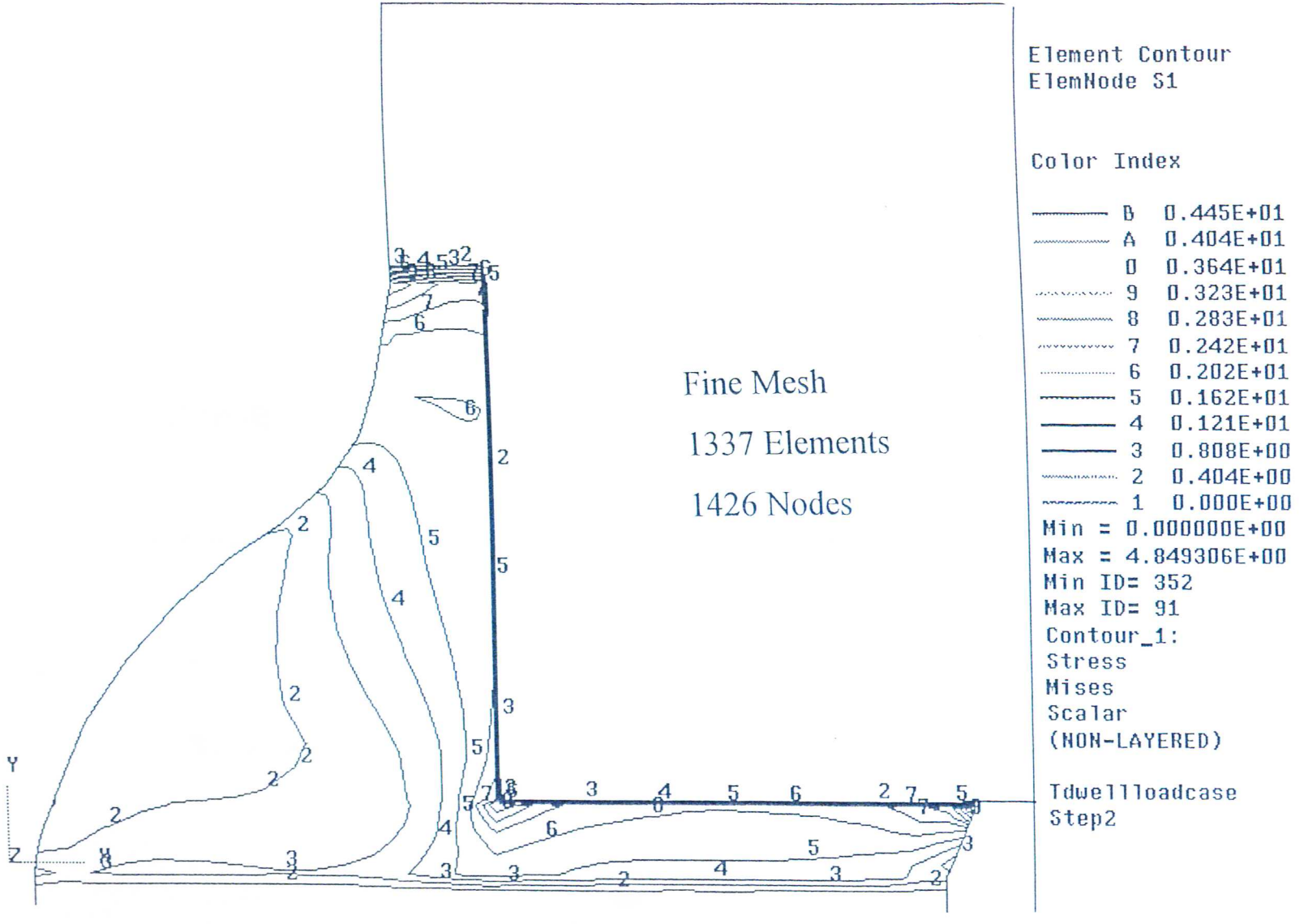
Fine Mesh

1337 Elements

1426 Nodes



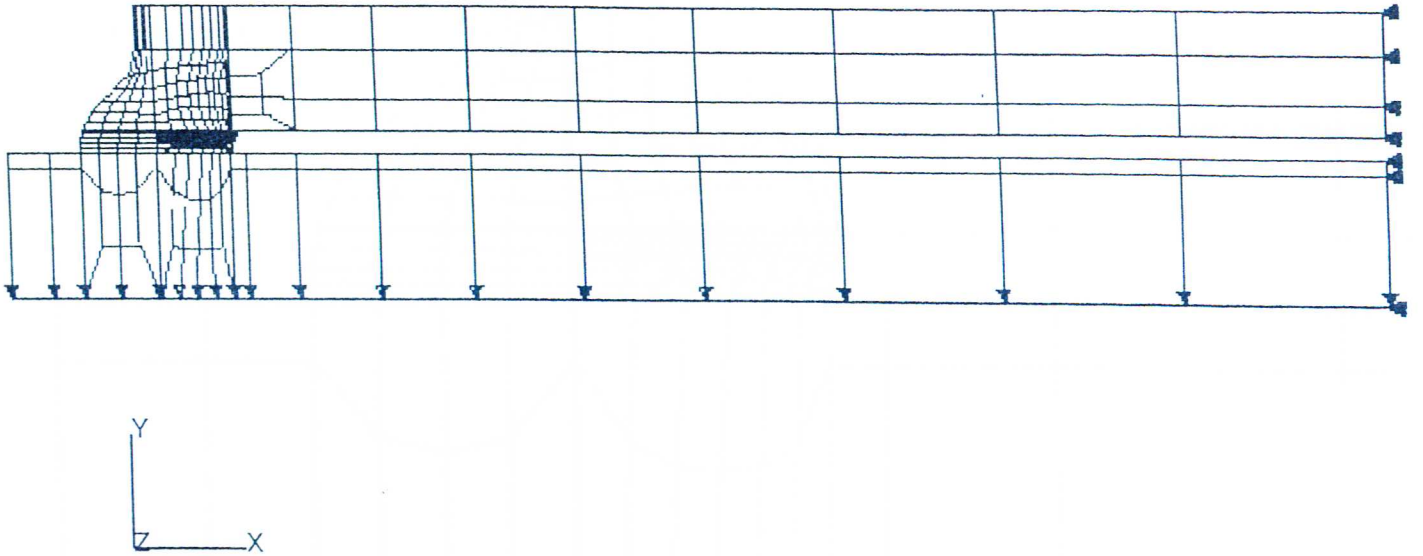

Fine Mesh
1337 Elements
1426 Nodes
Y
Z
X

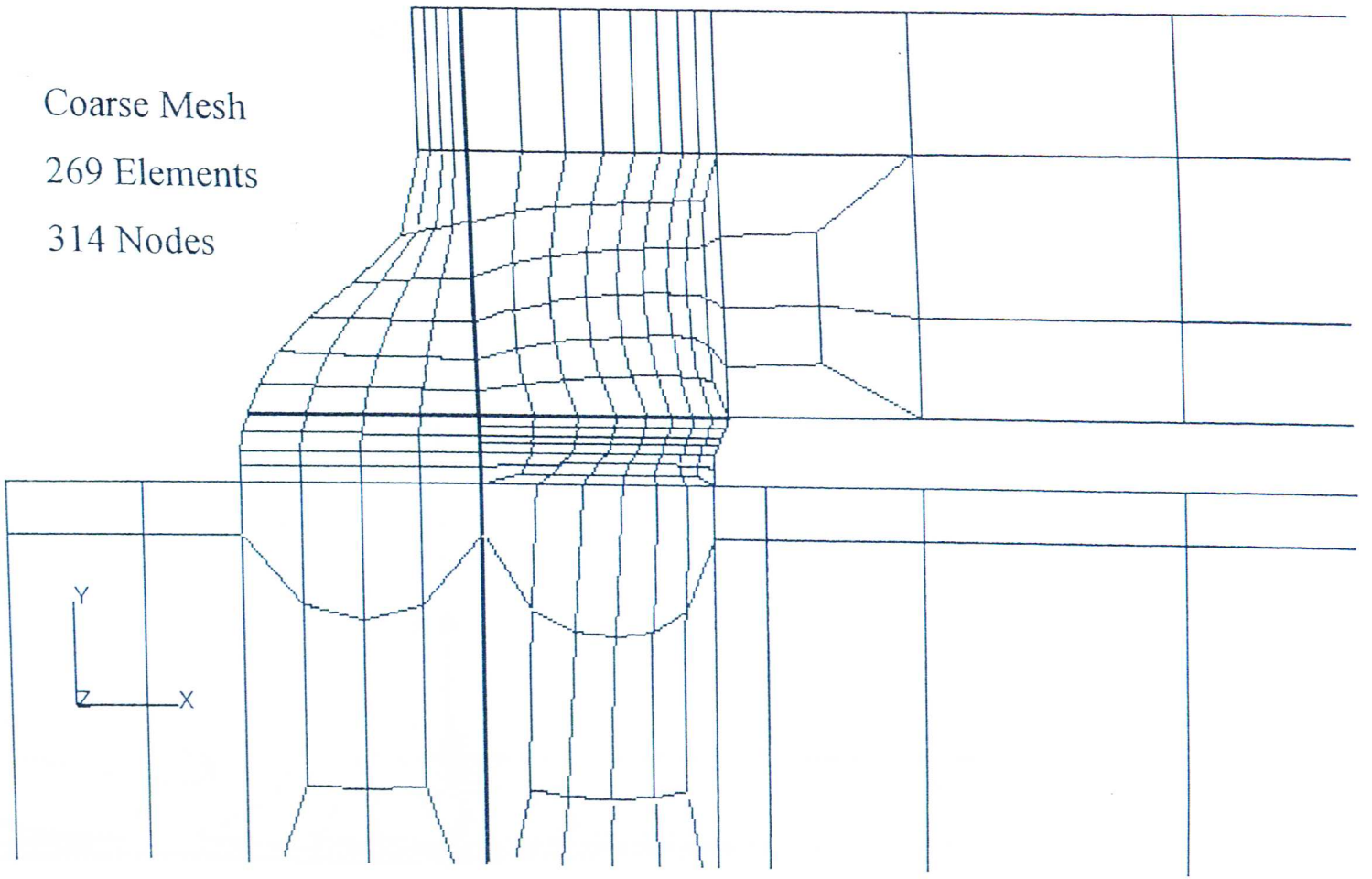

Fine Mesh
1337 Elements
1426 Nodes
Element Contour
ElemNode S1
Color Index
B 0.445E+01
A 0.404E+01
0 0.364E+01
9 0.323E+01
8 0.283E+01
7 0.242E+01
6 0.202E+01
5 0.162E+01
4 0.121E+01
3 0.808E+00
2 0.404E+00
1 0.000E+00
Min = 0.000000E+00
Max = 4.849306E+00
Min ID= 352
Max ID= 91
Contour_1:
Stress
Mises
Scalar
(NON-LAYERED)
Tdwellloadcase
Step2
Y
Z

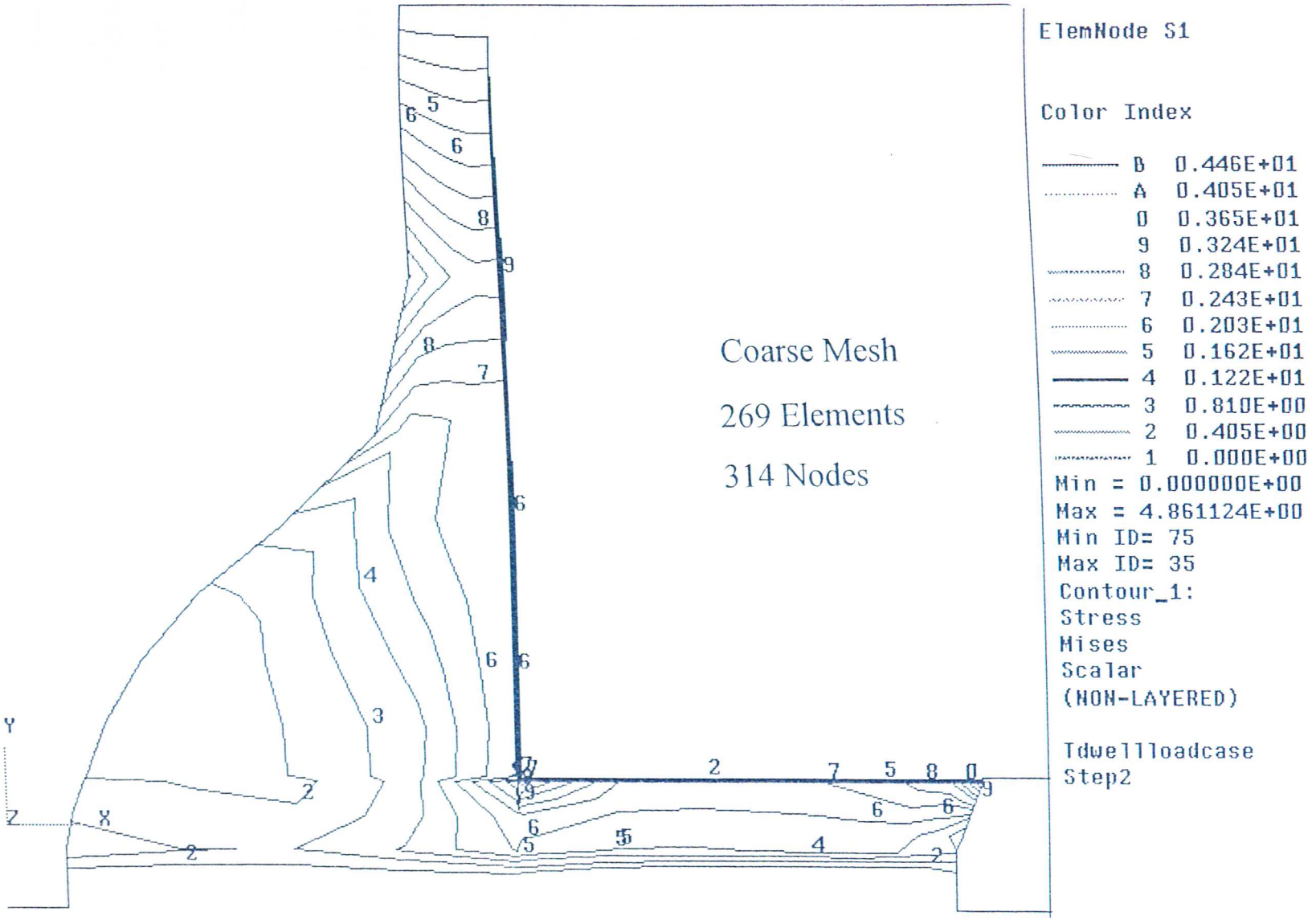
Coarse Mesh

269 Elements

314 Nodes




Coarse Mesh
269 Elements
314 Nodes
Y
Z
X


Coarse Mesh
269 Elements
314 Nodes
ElemNode S1
Color Index
B 0.446E+01
A 0.405E+01
0 0.365E+01
9 0.324E+01
8 0.284E+01
7 0.243E+01
6 0.203E+01
5 0.162E+01
4 0.122E+01
3 0.810E+00
2 0.405E+00
1 0.000E+00
Min = 0.000000E+00
Max = 4.861124E+00
Min ID= 75
Max ID= 35
Contour_1:
Stress
Mises
Scalar
(NON-LAYERED)
Tdwellloadcase
Step2
Y
Z
X

Appendix J Sample Abaqus Input File

```
*HEADING
ABAQUS job created on 14-Sep-95 at 11:07:56
*NODE, NSET=ALLTHEM
     1,    0.2032,         0.
Nodal data in x, y, z coordinates units mm
   314,     8.525,    -1.3144
**
**
*ELEMENT, TYPE=CPS4, ELSET=SOLDERJO
     1,     1,     2,     5,     4
connectivity for solder joint elements
    74,    91,    97,    98,    92
*ELEMENT, TYPE=CPS4, ELSET=ELM91
two critical elements in solder joint
    35,    42,    43,    48,    47
    36,    43,    44,    49,    48
*ELEMENT, TYPE=CPS4, ELSET=COPPERW
    75,     1,     7,    99,    68
connectivity for copper tungsten LCC bond pad elements
    89,   113,    93,    68,    99
*ELEMENT, TYPE=CPS4, ELSET=COPPER
   190,    52,   227,   229,    55
connectivity for copper substrate bond pad elements
   221,   256,   257,   186,   258
*ELEMENT, TYPE=CPS4, ELSET=LCC
    90,    74,    80,   115,   114
connectivity for LCC elements
   189,   213,   216,   226,   225
*ELEMENT, TYPE=CPS4, ELSET=POLY_CIC
   162,   186,   187,   190,   189
connectivity for substrate elements
   269,   310,   311,   314,   313
**
** solderjoint
**
*SOLID SECTION, ELSET=SOLDERJO, MATERIAL=SOLDER
      0.1,
**
**        critical solderjoint element in solder
**
*SOLID SECTION, ELSET=ELM91, MATERIAL=SOLDER
       0.1,
**
** copperW
**
*SOLID SECTION, ELSET=COPPERW, MATERIAL=CU_W
      0.1,
**
** copper
**
*SOLID SECTION, ELSET=COPPER, MATERIAL=CU
```

```
      0.1,
**
** LCC
**
*SOLID SECTION, ELSET=LCC, MATERIAL=CERAMIC
      0.1,
**
** poly_cic
**
*SOLID SECTION, ELSET=POLY_CIC, MATERIAL=SUBSTRAT
      0.1,
**----------------------------------------------------------
*INITIAL CONDITIONS, TYPE=TEMPERATURE
ALLTHEM, 0.2500000E+2
**----------------------------------------------------------
**
** solder
** Date: 30-Aug-95          Time: 16:16:40
**
*MATERIAL, NAME=SOLDER
**
*ELASTIC, TYPE=ISO
    24960.,       0.4
**
*EXPANSION, TYPE=ISO, ZERO=0.2500000E+2
   2.39E-5,
**
**Because plasticity only occurs while at low temp
**can use one plastic law
*PLASTIC, HARDENING=ISOTROPIC
   29.86,        0.
    30.0,       0.00085
    31.0,       0.0011
    33.0,       0.0021
    34.0,       0.0028
    36.0,       0.0048
   38.84,        0.01
    48.0,       0.0132
    55.0,       0.276
*CREEP, LAW=USER
*USER SUBROUTINES
      SUBROUTINE CREEP(DECRA,DESWA,STATEV,SERD,ECO,ESWO,P,QTILD,
     1  TEMP,DTEMP,PREDEF,DPRED,TIME,DTIME,CMNAME,LEXIMP,LEND,
     2  COORDS,NSTATV,NOEL,NPT,LAYER,KSPT,KSTEP,KINC)
      INCLUDE "ABA_PARAM.INC"
      CHARACTER*8 CMNAME
      DIMENSION DECRA(5),DESWA(5),STATEV(*),PREDEF(1),DPRED(1),
     1  TIME(2),COORDS(*)
      A=0.2557
      AN=6.28
      DELH=0.7036
      AK=8.617E-5
      DECRA(1)=A*QTILD**AN*EXP(-1.0*DELH/(AK*(TEMP+273)))*DTIME
      RETURN
```

```
      END
**
** CU
** Date: 30-Aug-95          Time: 16:16:40
**
*MATERIAL, NAME=CU
**
*ELASTIC, TYPE=ISO
    82740.,       0.34
**
*EXPANSION, TYPE=ISO, ZERO=25.
    1.67E-5,
**
** CU_W
** Date: 30-Aug-95          Time: 16:16:40
**
*MATERIAL, NAME=CU_W
**
*ELASTIC, TYPE=ISO
    71708.,       0.17
**
*EXPANSION, TYPE=ISO, ZERO=25.
    5.4E-6,
**
** Ceramic
** Date: 30-Aug-95          Time: 16:16:40
**
*MATERIAL, NAME=CERAMIC
**
*ELASTIC, TYPE=ISO
   379018.,       0.21
**
*EXPANSION, TYPE=ISO, ZERO=25.
    5.4E-6,
**
** substrate
** Date: 30-Aug-95          Time: 16:16:40
**
*MATERIAL, NAME=SUBSTRAT
**
*ELASTIC, TYPE=ISO
    27580.,       0.13
**
*EXPANSION, TYPE=ISO, ZERO=25.
    9.25E-5,
**
**********************************************************
*STEP
LOAD CASE 1: INTRODUCE THE INITIAL BOUNDARY CONDITION
** ALL BCs applied with OP=NEW must be applied during the
**same step.  Do not use OP=MOD with a perturbation step.          *STATIC
*BOUNDARY, OP=NEW
   216, XSYMM
   217, XSYMM
```

```
   218, XSYMM
   226, XSYMM
   312, XSYMM
   313, XSYMM
   314, XSYMM
   314, YSYMM
   188, YSYMM
   191, YSYMM
   194, YSYMM
   261, YSYMM
   264, YSYMM
   266, YSYMM
   271, YSYMM
   275, YSYMM
   277, YSYMM
   280, YSYMM
   283, YSYMM
   288, YSYMM
   293, YSYMM
   296, YSYMM
   299, YSYMM
   302, YSYMM
   305, YSYMM
   308, YSYMM
   311, YSYMM
*END STEP
**********************************************************
**        step 2, GO FROM Tr TO 28 DEG C, TC1
**        one sec. elastic plus 11 sec. viscoelastic
**        each 3deg C = 10deg C/min
*STEP, INC=40, AMPLITUDE=RAMP
**
*STATIC
0.1, 1.0
*TEMPERATURE, OP=MOD
ALLTHEM,        28.
**
*EL FILE, ELSET=ELM91, POSITION=INTEGRATION POINT
 TEMP,S,SINV,ENER,E,PE,CE,EE
*EL PRINT, POSITION=INTEGRATION POINT, FREQUENCY=0
*NODE PRINT, GLOBAL=YES, FREQUENCY=0
*NODE FILE, GLOBAL=YES, FREQUENCY=0
*END STEP
* STEP, INC=1000, AMPLITUDE=RAMP
*VISCO,CETOL=5.E-6,EXPLICIT
1.0E-2, 11
**
*EL FILE, ELSET=ELM91, POSITION=INTEGRATION POINT
TEMP,S,SINV,ENER,E,PE,CE,EE
*EL PRINT, POSITION=INTEGRATION POINT, FREQUENCY=0
*NODE PRINT, GLOBAL=YES, FREQUENCY=0
*NODE FILE, GLOBAL=YES, FREQUENCY=0
*END STEP
**********************************************************
```

```
*STEP, INC=40, AMPLITUDE=RAMP
**
*STATIC
0.1, 1.0
*TEMPERATURE, OP=MOD
ALLTHEM,        31.
**
*EL FILE, ELSET=ELM91, POSITION=INTEGRATION POINT
TEMP,S,SINV,ENER,E,PE,CE,EE
*EL PRINT, POSITION=INTEGRATION POINT, FREQUENCY=0
*NODE PRINT, GLOBAL=YES, FREQUENCY=0
*NODE FILE, GLOBAL=YES, FREQUENCY=0
*END STEP
* STEP, INC=1000, AMPLITUDE=RAMP
*VISCO,CETOL=5.E-6,EXPLICIT
1.0E-2, 11
**
*EL FILE, ELSET=ELM91, POSITION=INTEGRATION POINT
TEMP,S,SINV,ENER,E,PE,CE,EE
*EL PRINT, POSITION=INTEGRATION POINT, FREQUENCY=0
*NODE PRINT, GLOBAL=YES, FREQUENCY=0
*NODE FILE, GLOBAL=YES, FREQUENCY=0
*END STEP
**********************************************************
**the previouse steps are repeated until two thermal cycles
** are completed
```

Appendix K Fortran Post Processing File for FEM Analysis

```
C  In order to link the following command is typed at the command prompt
C f77 namee.f -o name /software/calce/abaqus5.4/lib/shr.a /software/calce/abaqus5.4/lib/interface.a
C
c  This program computes the maximum equivalent stress and strain (elastic,
c  plastic, and creep) in the solder, locate the integration point where
c  the maximum values occurs.
c
c Input Filename: 'fname.fil', where fname is the root name of the
                                        input file.
c
c
c Output Filename: read.dat
c                  output.dat
c
ccccccccccccccccccccccccccccccccccccccccccccccccccccccccccccccccccccccccccccc
c
c Variables used by this programm and ABAQUS subroutines SPRINC and SPRIND:
c
c ndi     -- number of direct components in stress/strain tensor.
c nshr    -- number of shear components in stress/strain tensor.
c ndip1   -- ndi + 1
c array   -- real array containing values read from results file (.fil).
c            equivalenced to jrray.
c jrray   -- integer array containing values read from results file (.fil).
c            equivalenced to array.
c fname   -- root file name of input file (w/o .fil extension).
c nru     -- number of results files (.fil) to be read.
c lrunit-- array containing unit number and format of results files:
c                  lrunit(1,*) --> unit number of input file.
c                  lrunit(2,*) --> format of input file.
c
c loutf   -- format of output file:
c                  0 --> standard ASCII format.
c                  1 --> ABAQUS results file ASCII format.
c                  2 --> ABAQUS results file binary format.
c
c junit   -- unit number of file to be opened.
c jrcd    -- error check return code.
c                  .eq. 0 --> no errors.
c                  .ne. 0 --> errors detected
c key     -- current record key identifier.
c jelnum-- current element number.
c intpn   -- integration point number.
c lstr    -- indicates type of principal value (stress/strain) and
c            ordering used:
c                  for calculation of pricipal value (stress/strain):
c
c                  1 --> stress.
c                  2 --> strain.
c                  for calculatin of directions:
c                  1 --> stress.
c                  2 --> strain.
c s       -- array containing stress tensor.
c ele     -- array containing elastic strain tensor.
c ple     -- array containing plastic strain tensor.
```

```
c cre     -- array containing creep strain tensor.
c totale -- array containing total strain tensor.
c seq     -- equivalent stress.
c eleeq   -- equivalent elastic strain.
c pleeq   -- equivalent plastic strain.
c creeq   -- equivalent creep strain.
c totaleeq -- equivalent total strain.
c seqm    -- maximum equivalent stress.
c eleeqm -- maximum equivalent elastic strain.
c pleeqm -- maximum equivalent plastic strain.
c creeqm -- maximum equivalent creep strain.
c totaleeqm -- maximum total equivalent strain.
c numeles -- element number where maximun mises stress value occurs.
c numints -- int. point number where maximum mises stress value ouucrs.
c numeleel -- element number where eleeqm ouucurs.
c numintel -- int. point number where eleeqm occurs.
c numelepl -- element number where pleeqm occurs.
c numintpl -- int. point number where pleeqm occurs.
c numelecr -- element number where creeqm occurs.
c numintcr -- int. point where creeqm occurs.
c numeletotal -- element number where totaleeqm occurs.
c numinttotal -- int. point where totaleeqm occurs.
      implicit real*8 (a-h,o-z)
      parameter (Ntotal_inc=500,Nele=20,Ngau=4)
      real mus
      common /stress/sigmax(Ntotal_inc,Nele,Ngau),sigmay(Ntotal_inc,
     1   Nele,Ngau),tauxy(Ntotal_inc,Nele,Ngau)
      common/el_strain/el_epsix(Ntotal_inc,Nele,Ngau),el_epsiy(Ntotal_inc,
     1   Nele,Ngau),el_epsiz(Ntotal_inc,Nele,Ngau),
     2   el_gammaxy(Ntotal_inc,Nele,Ngau)
      common/pl_strain/pl_epsix(Ntotal_inc,Nele,Ngau),pl_epsiy(Ntotal_inc,
     1   Nele,Ngau),pl_epsiz(Ntotal_inc,Nele,Ngau),
     2   pl_gammaxy(Ntotal_inc,Nele,Ngau)
      common/cr_strain/cr_epsix(Ntotal_inc,Nele,Ngau),cr_epsiy(Ntotal_inc,
     1   Nele,Ngau),cr_epsiz(Ntotal_inc,Nele,Ngau),
     2   cr_gammaxy(Ntotal_inc,Nele,Ngau)
      common/t_strain/t_epsix(Ntotal_inc,Nele,Ngau),t_epsiy(Ntotal_inc,
     1   Nele,Ngau),t_epsiz(Ntotal_inc,Nele,Ngau),
     2   t_gammaxy(Ntotal_inc,Nele,Ngau)
      common/equivalent/vonmis(Ntotal_inc,Nele,Ngau),el_epsieq(Ntotal_inc,
     1   Nele,Ngau),pl_epsieq(Ntotal_inc,Nele,Ngau),cr_epsieq(Ntotal_inc,
     2   Nele,Ngau),t_epsieq(Ntotal_inc,Nele,Ngau)
      common/energy/strenergy(Ntotal_inc,Nele,Ngau),plwork(Ntotal_inc,
     1   Nele,Ngau),crwork(Ntotal_inc,Nele,Ngau)
      common/time/time_inc(Ntotal_inc),time_total(Ntotal_inc)
      common/temperature/temp(Ntotal_inc)
      common/total_increments/Nof_total_step,Nof_total_inc
      common/solder_property/Es,Gs,cte,mus
      common/H_equivalent/H_vonmis(Ntotal_inc),H_el_epsieq(Ntotal_inc),
     1   H_pl_epsieq(Ntotal_inc),H_cr_epsieq(Ntotal_inc),
     2   H_t_epsieq(Ntotal_inc)

      character fname*80
```

```
      write(6,*) 'Enter the name of the input file (w/o .fil):'
      read(5,'(a)') fname
      write(6,*) fname
      call input_data
      write(6,*) 'got all solder data'
      call read_fil_file(fname)
      write(6,*) 'read all of .fil'
      call do_averaging

      stop
      end


cccccccccccccccccccccccccccccccccccccccccccccccccccccccccccccccccccccccc
ccccccccccccccccccc    SUBROUTINES    ccccccccccccccccccccccccccccccccc
cccccccccccccccccccccccccccccccccccccccccccccccccccccccccccccccccccccccc

cccccccccccccccccccccccccccccccccccccccccccccccccccccccccccccccccccccccc
c input_data: input necessary data for the analysis
cccccccccccccccccccccccccccccccccccccccccccccccccccccccccccccccccccccccc
      subroutine input_data
      implicit real*8 (a-h,o-z)
      real mus
      common/solder_property/Es,Gs,cte,mus
      Es=2.496d6
      Gs=0.5*Es/(1.0+mus)
      mus=0.4
      cte=21.0d-6
      return
      end

cccccccccccccccccccccccccccccccccccccccccccccccccccccccccccccccccccccccc
c read_fil_file: to read result from ABAQUS .fil output data files, and store
c      them in the common blocks, without flip the sign
cccccccccccccccccccccccccccccccccccccccccccccccccccccccccccccccccccccccc
      subroutine read_fil_file(fname)
      parameter (Ntotal_inc=500,Nele=20,Ngau=4)
      implicit real*8 (a-h,o-z)
      dimension array(513), jrray(2,513), lrunit(2,1)
      equivalence (array(1), jrray(1,1))
      common /stress/sigmax(Ntotal_inc,Nele,Ngau),sigmay(Ntotal_inc,
     1   Nele,Ngau),tauxy(Ntotal_inc,Nele,Ngau)
      common/el_strain/el_epsix(Ntotal_inc,Nele,Ngau),el_epsiy(Ntotal_inc,
     1   Nele,Ngau),el_epsiz(Ntotal_inc,Nele,Ngau),
     2   el_gammaxy(Ntotal_inc,Nele,Ngau)
      common/pl_strain/pl_epsix(Ntotal_inc,Nele,Ngau),pl_epsiy(Ntotal_inc,
     1   Nele,Ngau),pl_epsiz(Ntotal_inc,Nele,Ngau),
     2   pl_gammaxy(Ntotal_inc,Nele,Ngau)
      common/cr_strain/cr_epsix(Ntotal_inc,Nele,Ngau),cr_epsiy(Ntotal_inc,
     1   Nele,Ngau),cr_epsiz(Ntotal_inc,Nele,Ngau),
     2   cr_gammaxy(Ntotal_inc,Nele,Ngau)
      common/t_strain/t_epsix(Ntotal_inc,Nele,Ngau),t_epsiy(Ntotal_inc,
     1   Nele,Ngau),t_epsiz(Ntotal_inc,Nele,Ngau),
     2   t_gammaxy(Ntotal_inc,Nele,Ngau)
```

```
      common/equivalent/vonmis(Ntotal_inc,Nele,Ngau),el_epsieq(Ntotal_inc,
     1    Nele,Ngau),pl_epsieq(Ntotal_inc,Nele,Ngau),cr_epsieq(Ntotal_inc,
     2    Nele,Ngau),t_epsieq(Ntotal_inc,Nele,Ngau)
      common/energy/strenergy(Ntotal_inc,Nele,Ngau),plwork(Ntotal_inc,
     1    Nele,Ngau),crwork(Ntotal_inc,Nele,Ngau)
      common/time/time_inc(Ntotal_inc),time_total(Ntotal_inc)
      common/temperature/temp(Ntotal_inc)
      common/total_increments/Nof_total_step,Nof_total_inc
      character fname*80
c=======================================================================
c Open the output file.
c=======================================================================


      open(unit=55,file='menergy.m')
      open(unit=59,file='steps.dat')
      write(55,*)'% strain_energy pl_work cr_work'
      write(55,*)'work=['

      inc_total=0
      nru=1
      loutf=0
      lrunit(1,1)=8
      lrunit(2,1)=2
      call initpf(fname,nru,lrunit,loutf)
      junit=lrunit(1,1)
      call dbrnu(junit)
c=======================================================================
c Read records from the results (.fil) file and process the data.  Cover a
c maximum of 10 million records in the file.
c=======================================================================
      do 1000 k100=1,20000
        do 1000 k1=1,20000
          call dbfile(0,array,jrcd)
          if (jrcd.ne.0) go to 1001
          key=jrray(1,2)
c=======================================================================
c Get the current step, increment number and time.
c=======================================================================
          if (key.eq.2000) then
              inc_total=inc_total+1
              istep=jrray(1,8)
              inc_step=jrray(1,9)
              time_inc(inc_total)=array(4)
              time_total(inc_total)=array(3)
              write(6,2001)istep,inc_step,inc_total,
     1            time_inc(inc_total),time_total(inc_total)
              write(6,*)'-----------------------------------------'
 2001         format(1x,'istep=',i3,1x,'inc_step=',i3,1x,
     1            'inc_total=',i4,1x,'time_inc=',f8.3,1x,'time_total=',
     2            f8.3)
              write(59,2002)istep,inc_step,inc_total
 2002         format(3i4)
c=======================================================================
```

```
c Get the element and integration point numbers, jelnum and intpn, and the
c location of intpn (0--at inp.pt., 1--at centroid, 4--nodal average) and
c the number of direct and shear components in the analysis.
c=======================================================================
              else if (key.eq.1) then
                    jelnum=jrray(1,3)
                    intpn=jrray(1,4)
                    locate=jrray(1,6)
                    ndi=jrray(1,8)
                    nshr=jrray(1,9)
                    ndip1=ndi+1


c=======================================================================
c Get the temperature.
c=======================================================================
              else if (key.eq.2) then
                    temp(inc_total)=array(3)
c=======================================================================
c Get the stress tensor.
c=======================================================================
              else if (key.eq.11) then
                    sigmax(inc_total,jelnum,intpn)=array(3)
                    sigmay(inc_total,jelnum,intpn)=array(4)
                    tauxy(inc_total,jelnum,intpn)=array(5)

c=======================================================================
c Get the von-mises stress
c=======================================================================
                    else if (key.eq.12) then
                      vonmis(inc_total,jelnum,intpn)=array(3)

c=======================================================================
c Get the energy density.
c=======================================================================
                    else if (key.eq.14) then
                      strenergy(inc_total,jelnum,intpn)=array(3)
                      plwork(inc_total,jelnum,intpn)=array(4)
                      crwork(inc_total,jelnum,intpn)=array(5)
                      if (jelnum.eq.35.and.intpn.eq.4) then
                        write(55,2060) strenergy(inc_total,jelnum,intpn),
     1                        plwork(inc_total,jelnum,intpn),
     2                        crwork(inc_total,jelnum,intpn)
                      endif
 2060                 format(f12.4,f12.4,f12.4,';')
c=======================================================================
c Get the total strain tensor
c=======================================================================
                    else if (key.eq.21) then
                      t_epsix(inc_total,jelnum,intpn)=array(3)
                      t_epsiy(inc_total,jelnum,intpn)=array(4)
                      t_gammaxy(inc_total,jelnum,intpn)=array(5)
                      call get_z_component(t_epsiz(inc_total,jelnum,intpn),
     1                        t_epsix(inc_total,jelnum,intpn),
```

```
     2                t_epsiy(inc_total,jelnum,intpn),
     3                t_gammaxy(inc_total,jelnum,intpn))

c=======================================================================
c Get the plastic strain tensor, and the equivalent plastic strain
c=======================================================================
            else if (key.eq.22) then
              pl_epsix(inc_total,jelnum,intpn)=array(3)
              pl_epsiy(inc_total,jelnum,intpn)=array(4)
              pl_gammaxy(inc_total,jelnum,intpn)=array(5)
              pl_epsieq(inc_total,jelnum,intpn)=array(6)
              ipart=2
              call get_z_component(pl_epsiz(inc_total,jelnum,intpn),
     1                pl_epsix(inc_total,jelnum,intpn),
     2                pl_epsiy(inc_total,jelnum,intpn),ipart)

c=======================================================================
c Get the creep strain tensor and the equivalent creep strain.
c=======================================================================
            else if (key.eq.23) then
              cr_epsix(inc_total,jelnum,intpn)=array(3)
              cr_epsiy(inc_total,jelnum,intpn)=array(4)
              cr_gammaxy(inc_total,jelnum,intpn)=array(5)
              cr_epsieq(inc_total,jelnum,intpn)=array(6)
              ipart=2
              call get_z_component(cr_epsiz(inc_total,jelnum,intpn),
     1                cr_epsix(inc_total,jelnum,intpn),
     2                cr_epsiy(inc_total,jelnum,intpn),ipart)

c=======================================================================
c Get the elastic strain tensor.
c=======================================================================
            else if (key.eq.25) then
              el_epsix(inc_total,jelnum,intpn)=array(3)
              el_epsiy(inc_total,jelnum,intpn)=array(4)
              el_gammaxy(inc_total,jelnum,intpn)=array(5)
              ipart=1
              call get_z_component(el_epsiz(inc_total,jelnum,intpn),
     1                el_epsix(inc_total,jelnum,intpn),
     2                el_epsiy(inc_total,jelnum,intpn),ipart)
              call get_equivalent_strain(el_epsieq(inc_total,jelnum,
     1                intpn),
     2                el_epsix(inc_total,jelnum,intpn),
     3                el_epsiy(inc_total,jelnum,intpn),
     4                el_epsiz(inc_total,jelnum,intpn),
     5                el_gammaxy(inc_total,jelnum,intpn))
            endif
1000      continue
1001      write(6,*)'NO MORE INCREMENTS, END OF POSTPROCESS'
          Nof_total_step=istep
          Nof_total_inc=inc_total
          write(6,*)'Nof_total_step=',Nof_total_step
          write(6,*)'Nof_total_inc=',Nof_total_inc
```

```
      write(55,*)'];'

        close(unit=55)
        close(unit=59)

      return
      end

ccccccccccccccccccccccccccccccccccccccccccccccccccccccccccccccccccccccccccccccc
c get_z_component: to get the z compoment of the strain tensor for plane
c     stress problem.  ipart=1 for plastic and creep, where mu=0.5, while
c     ipart=1 for elastic, where mu=mus
ccccccccccccccccccccccccccccccccccccccccccccccccccccccccccccccccccccccccccccccc
      subroutine get_z_component(epsiz,epsix,epsiy,ipart)
      implicit real*8 (a-h,o-z)
      real mus,mu
      common/solder_property/Es,Gs,cte,mus
      if (ipart.eq.2) then
        mu=0.5d0
      else if (ipart.eq.1) then
        mu=mus
      endif
      epsiz=-1.0*mu*(epsix+epsiy)/(1.0-mu)
      return
      end

ccccccccccccccccccccccccccccccccccccccccccccccccccccccccccccccccccccccccccccccc
c get_equivalent_strain: get the equivalent strain (elastic...) from the
c     individual strain components.  pl_epsieq and cr_epsieq are obtained
c     directly from ABAQUS
ccccccccccccccccccccccccccccccccccccccccccccccccccccccccccccccccccccccccccccccc
      subroutine get_equivalent_strain(epsieq,epsix,epsiy,epsiz,gammaxy)
      implicit real*8 (a-h,o-z)
      epsixy=gammaxy/2.0d0
      fi=epsix+epsiy+epsiz
      si=(epsixy)**2-(epsix*epsiy+epsix*epsiz+epsiy*epsiz)
      epsieq=(2.0/3.0)*sqrt(fi**2+3.0*si)
      return
      end

ccccccccccccccccccccccccccccccccccccccccccccccccccccccccccccccccccccccccccccccc
c do_averaging: for the purpose of averaging.  Store /H_equivalent/ common
c     block from /equivalent/ common block
ccccccccccccccccccccccccccccccccccccccccccccccccccccccccccccccccccccccccccccccc
      subroutine do_averaging
      implicit real*8 (a-h,o-z)
      parameter(Ntotal_inc=500,Nele=20,Ngau=4)
      common/equivalent/vonmis(Ntotal_inc,Nele,Ngau),el_epsieq(Ntotal_inc,
     1   Nele,Ngau),pl_epsieq(Ntotal_inc,Nele,Ngau),cr_epsieq(Ntotal_inc,
     2   Nele,Ngau),t_epsieq(Ntotal_inc,Nele,Ngau)
      common/total_increments/Nof_total_step,Nof_total_inc
      common/H_equivalent/H_vonmis(Ntotal_inc),H_el_epsieq(Ntotal_inc),
     1   H_pl_epsieq(Ntotal_inc),H_cr_epsieq(Ntotal_inc),
     2   H_t_epsieq(Ntotal_inc)
```

```
      common/time/time_inc(Ntotal_inc),time_total(Ntotal_inc)
      common/temperature/temp(Ntotal_inc)

      write(6,*)'Input: Nofele, Nofint'
      read*,Nofele,Nofint
      open(unit=60,file='stepnum.m')
      open(unit=50,file='loop.m')


            write(50,*)'% temp von eleq pleq creq tote filename='
            write(60,*)'% step tot_time'
            write(60,*)'nstep=['
            write(50,*)'a=['

c     Nofele=91
c     Nofint=3
      do 100 line=1,Nof_total_inc

        H_vonmis(line)=vonmis(line,Nofele,Nofint)
        H_el_epsieq(line)=el_epsieq(line,Nofele,Nofint)
        H_pl_epsieq(line)=pl_epsieq(line,Nofele,Nofint)
        H_cr_epsieq(line)=cr_epsieq(line,Nofele,Nofint)
        H_t_epsieq(line)=t_epsieq(line,Nofele,Nofint)
100   continue
      open(unit=59,file='steps.dat')
      do 200 line=1,Nof_total_inc
        read(59,*)istep,inc_step,inc_total
      H_total_epsieq=H_el_epsieq(line)+H_pl_epsieq(line)+H_cr_epsieq(line)
        write(60,*)istep,time_total(line)
        write(50,1193)temp(line),H_vonmis(line),H_el_epsieq(line),
     1  H_pl_epsieq(line),H_cr_epsieq(line),H_total_epsieq
1193            format(f7.2,5e13.6,';')

200   continue
1000  format(1x,3i5,5x,3e12.4)
      write(50,*)'];'
      write(60,*)'];'

      close(unit=54)
      close(unit=55)
      close(unit=59)
      return
      end
```

Appendix L Matlab Post Processing File Used to Create Hysteresis Plots

```
clear
loop;                    % loop, stepnum, and menergy are created from
stepnum;                 % fortran post processing file
menergy;
sub=[43 166 233 358]     % array which determines when stresses flip
k=length(sub)
[rows,columns]=size(a);
laststep1=190            % last step in first thermal cycle
%=========================================================================
%       Read Temperature "temp"
%=========================================================================
for i=1:rows;
temp(i)=a(i,1);
end;
temp=temp';
%=========================================================================
%       Read Von-Mises stress unflipped "von"
%=========================================================================
for i=1:rows;
von(i)=a(i,2);
end;
von=von';
%=========================================================================
%       Flip according to von change in concavity
%       Creates flip array from sub array
%       sub array contains the subscripts which correspond
%       to changes in concavity of the von mises stresses
%=========================================================================
for i=1:rows;
flip(i)=0;
end;

for i=sub(1):sub(2)-1;
flip(i)=1;
end;
for i=sub(3):sub(4)-1;
flip(i)=1;
end;

flip=flip';

%       Flip the von mises stress
for i=1:rows;
if flip(i)==0;
vonflip(i)=a(i,2);
else;
vonflip(i)=-a(i,2);
end;
end;
%=========================================================================
```

```
%       Flip equivalent elastic strains (%)
%=============================================================
for i=1:rows;
if flip(i)==0;
eleshift(i)=100*a(i,3);
else;
eleshift(i)=-100*a(i,3);
end;
end;
%=============================================================
%       Flip equivalent strains (%)
%=============================================================

eshift(1)=0;
eflipped(1)=100*a(1,5);
tmp=0;
for i=2:rows;
eshift(i)=eshift(i-1);
        for j=1:k;
        if sub(j)==i & flip(i) == 1;
        eshift(i) = a(i,5)-tmp + eshift(i);
        tmp = a(i,5);
        elseif sub(j)==i & flip(i) == 0;
        eshift(i) = eshift(i)-a(i,5)+tmp ;
        tmp = a(i,5);
        end;
        end;
deltae(i)=a(i,5)-tmp;
  if flip(i)==0 ;
  eflipped(i)=100*(deltae(i)+eshift(i));
  else;
  eflipped(i)=100*(eshift(i)-deltae(i));
  end;
end;            %end i
                %=============================================
                %       Average
                %=============================================
                for i=1:rows-1;
                eavg(i)=(eflipped(i)+eflipped(i+1))/2;
                vonavg(i)=(vonflip(i)+vonflip(i+1))/2;
                end;    % end i on average
                eavg(rows)=eflipped(rows);
                vonavg(rows)=von(rows);


        creshift=eavg';   %creep flipped averaged

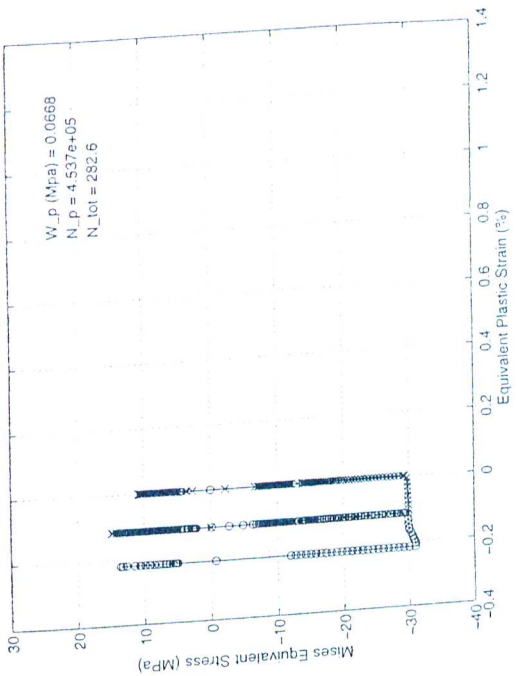
clear eflipped;
clear eavg;
vonel=vonflip;          %Doesnt average von for elastic
vonflip=vonavg';
%=============================================================
%       Flip Plastic
%=============================================================
```

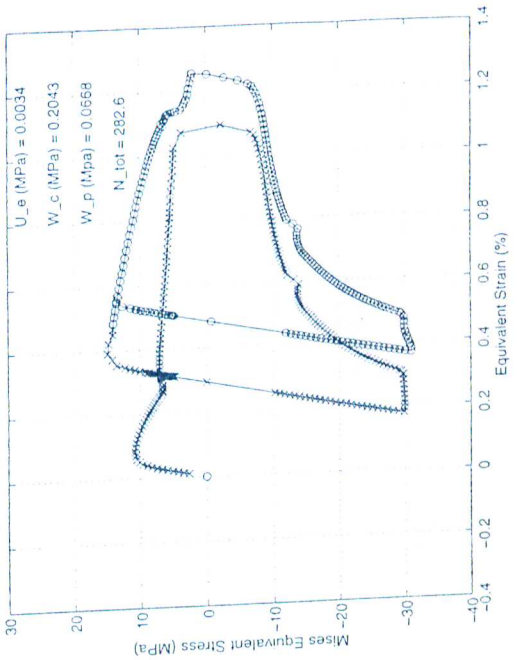
```
eshift(1)=0;
eflipped(1)=100*a(1,4);
tmp=0;
for i=2:rows;
eshift(i)=eshift(i-1);
        for j=1:k;
        if sub(j)==i & flip(i) == 1;
        eshift(i) = a(i,4)-tmp + eshift(i);
        tmp = a(i,4);
        elseif sub(j)==i & flip(i) == 0;
        eshift(i) = eshift(i)-a(i,4)+tmp ;
        tmp = a(i,4);
        end;
        end;
deltae(i)=a(i,4)-tmp;
  if flip(i)==0 ;
  eflipped(i)=100*(deltae(i)+eshift(i));
  else;
  eflipped(i)=100*(eshift(i)-deltae(i));
  end;
end;            %end i
        pleshift=eflipped';     %plastic strains flipped averaged
%=================================================
%       New total strain
%=================================================
for i=1:rows;
eleshift(i)=100*vonavg(i)/24960;
totshift(i)=pleshift(i)+creshift(i)+eleshift(i);
end;
totshift=totshift';
%=================================================================
%       Read unflipped stress and strains (%)
%=================================================================
for m=3:6;
for i=1:rows;
unflip(i)=100*a(i,m);
end;            %end i
        if m==3;
        ele=unflip';    %elastic unflipped
        elseif m==4;
        ple=unflip';    %plastic unflipped
        elseif m==5;
        cre=unflip';    %creep unflipped
        elseif m==6;
        tote=unflip';   %total unflipped
        end;            %end if on m
end;                    %end m
%=================================================================
%       Compute Total inel. flipped strains (%) "inel"
%=================================================================
for i=1:rows;
inelshift(i)=creshift(i)+pleshift(i);
end;
inelshift=inelshift';
```

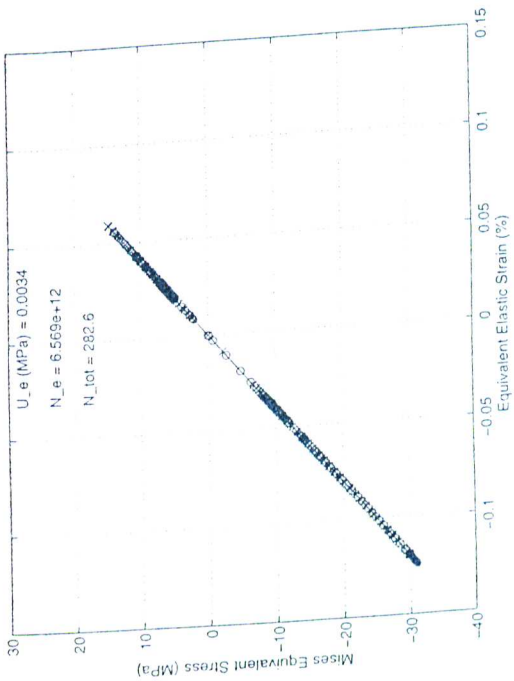
```
clear a;

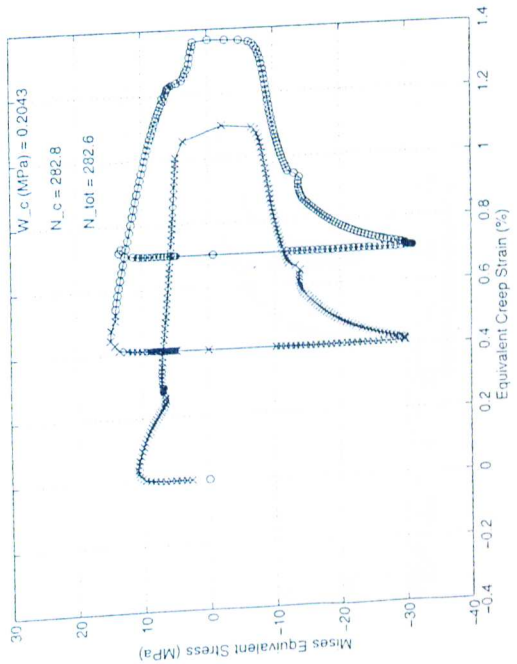
%=================================================================
%                          get the work
%=================================================================
for m=1:3;
for i=1:rows;
temp1(i)=work(i,m);
end      %end i
         if m==1;
         strain=temp1';    %strain energy
         elseif m==2;
         pl_work=temp1'; %plastic work
         elseif m==3;
         cr_work=temp1'; %creep work
         end;            %end if on m
end;                     %end m
%=================================================================
%       compute life from work for 2nd thermal cycle
%=================================================================
delstrain=strain(rows)
delpl_work=pl_work(rows)-pl_work(laststep1)
delcr_work=cr_work(rows)-cr_work(laststep1)
nf_el=(delstrain/.689)^(-1/.18)
nf_pl=(145*delpl_work/165.5)^(-1/.6)
nf_cr=(145*delcr_work/142.5)^(-1/1.16)
nf_tot=nf_el*nf_pl*nf_cr/(nf_el*nf_pl+nf_pl*nf_cr+nf_cr*nf_el)
%nf_tot=nf_el*nf_cr/(nf_cr+nf_el)          %use in case delpl_work=0
echo on;
```

Appendix M Hysteresis Plots From FEM Analysis

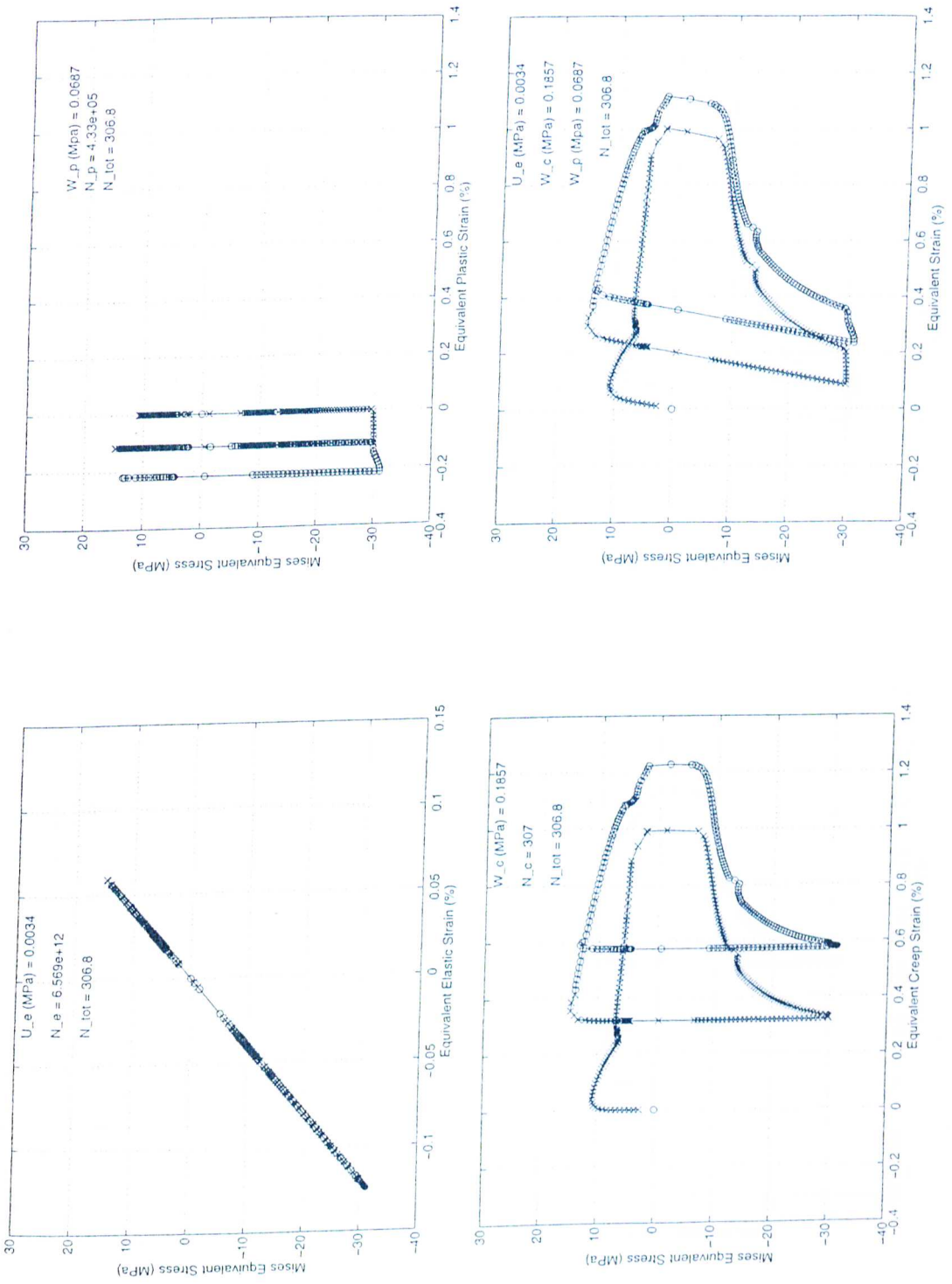




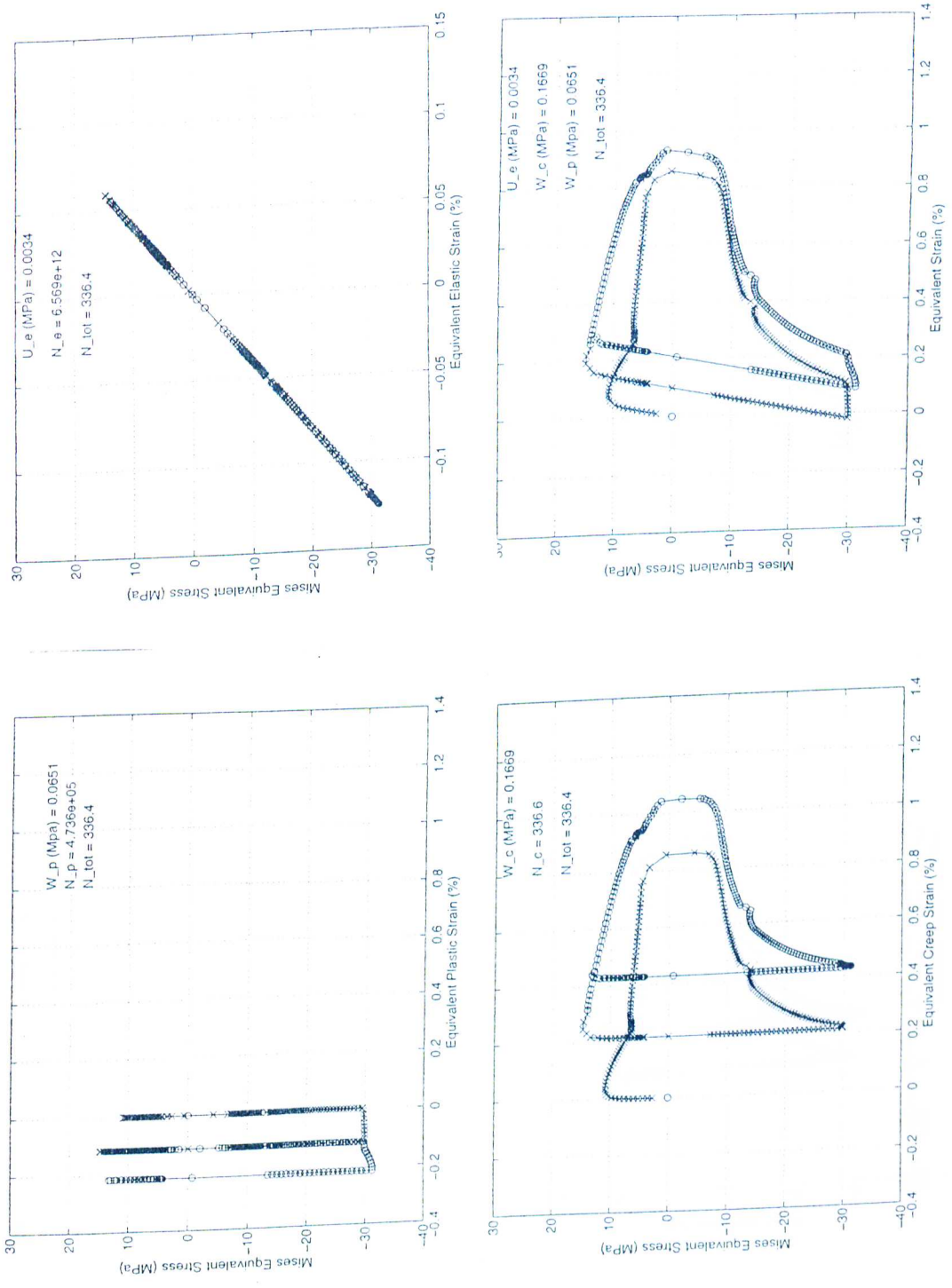




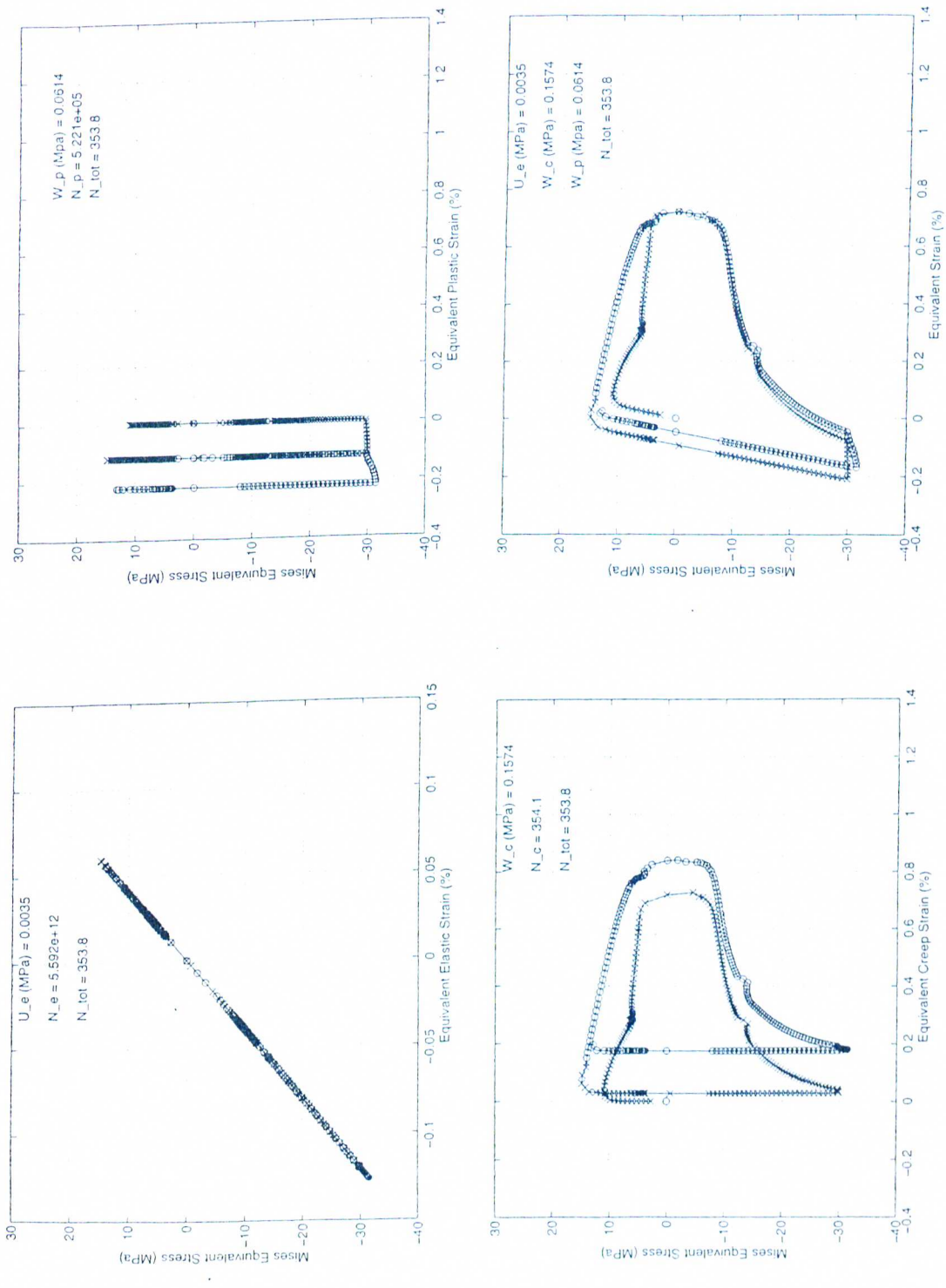
Hysteresis Plots for $L_d\Delta\alpha$=5372 X 10^{-6} mils/ ^{o}C



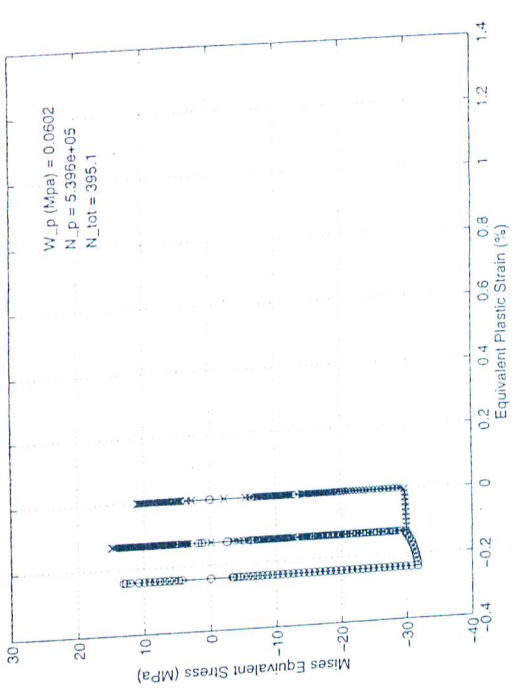
Hysteresis Plots for $L_d\Delta\alpha$=4902 X 10^{-6} mils/ ^{o}C

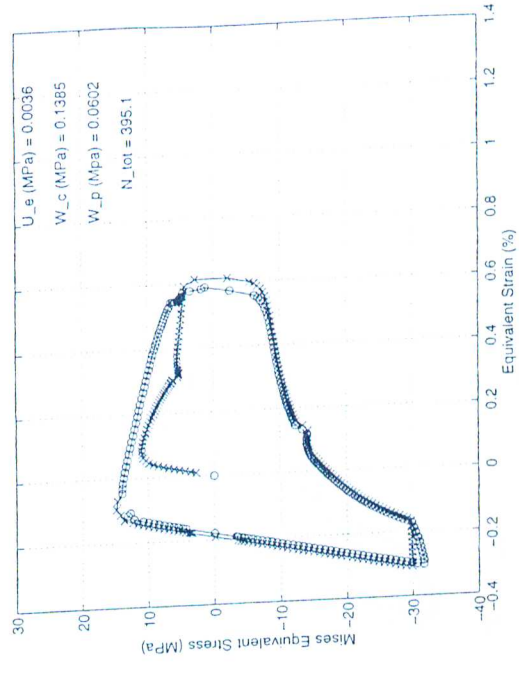


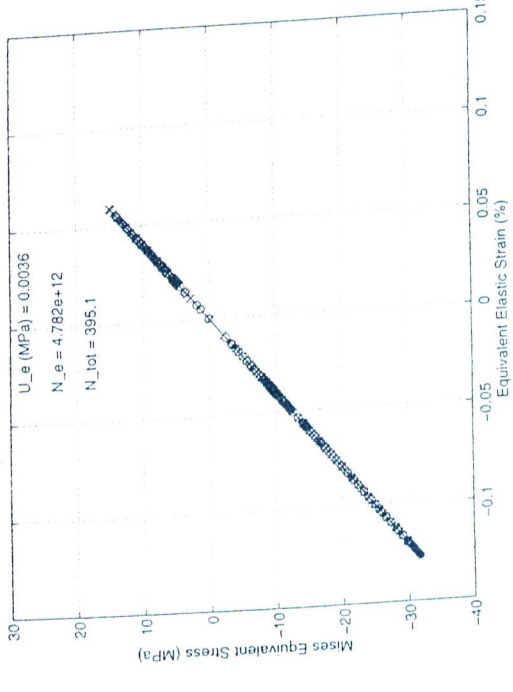
Hysteresis Plots for $L_d\Delta\alpha$=4257 X 10^{-6} mils/ ^{o}C

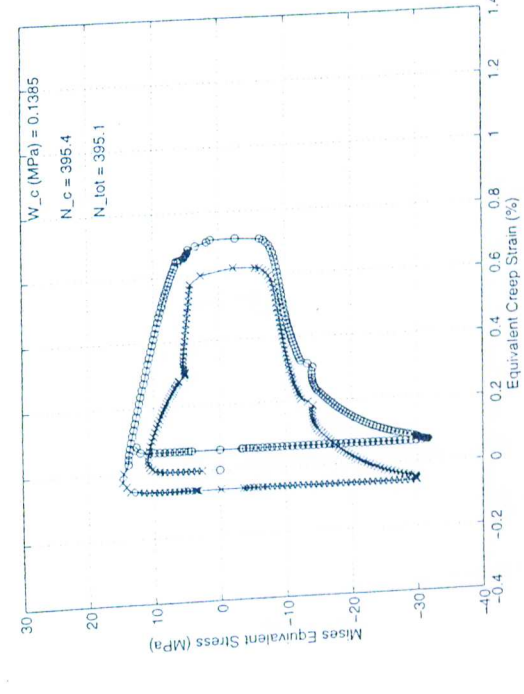


Hysteresi Plots for $L_d\Delta\alpha$=3707 X 10^{-6} mils/ ^{o}C

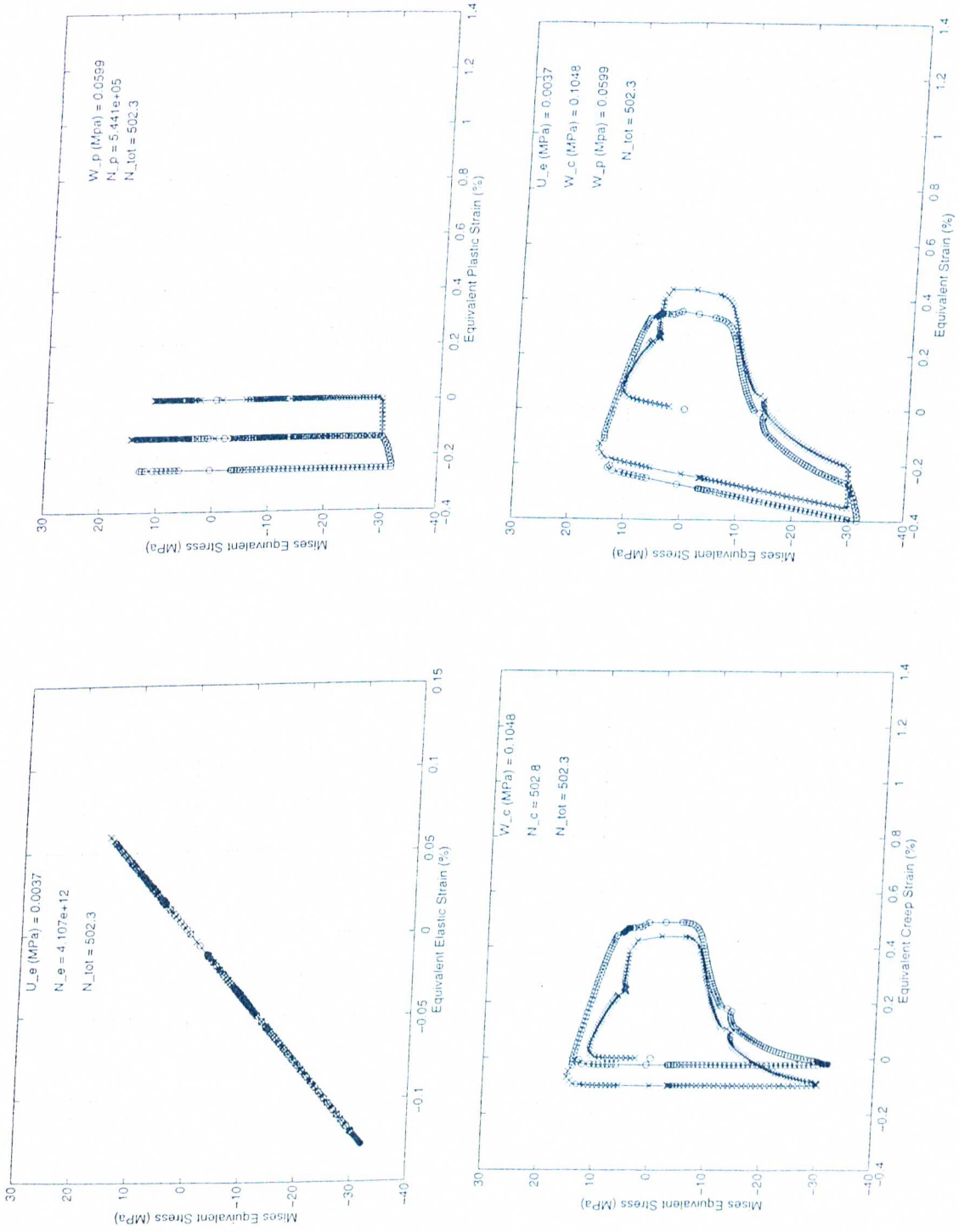




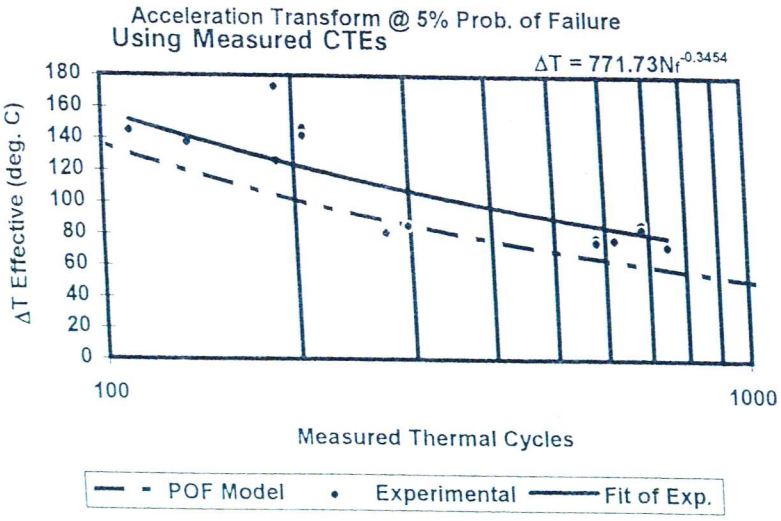


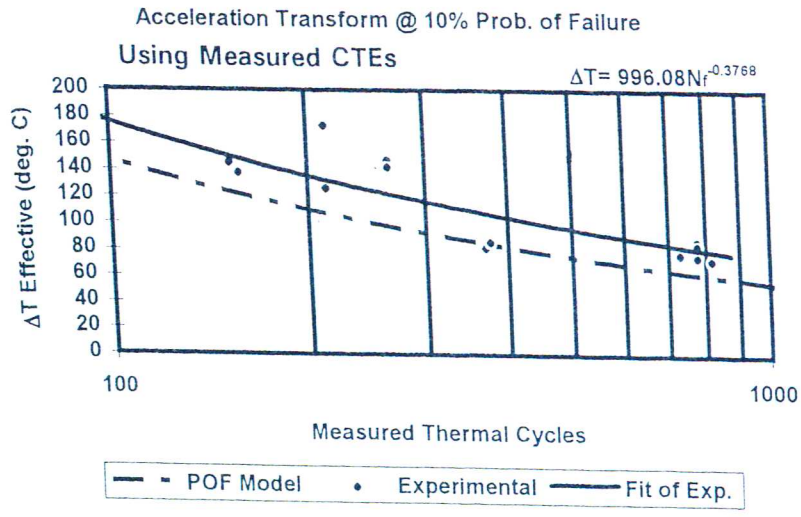


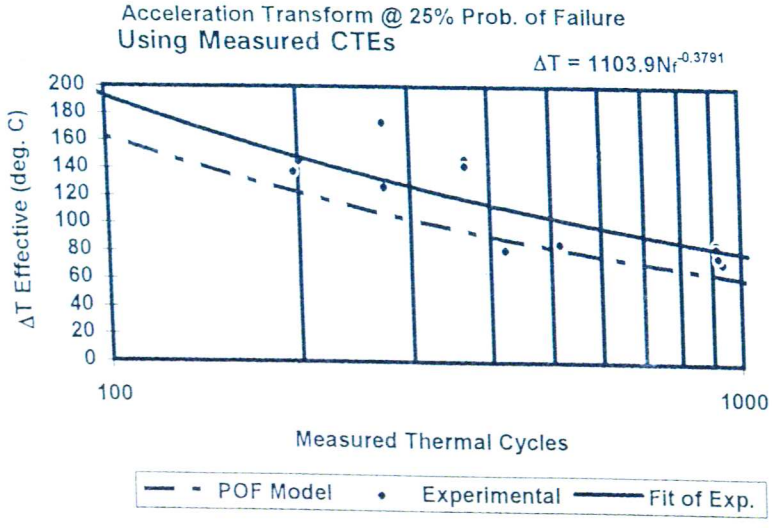
Hysteresis Plots for $L_d\Delta\alpha$=3166 X 10^{-6} mils/ ^{o}C

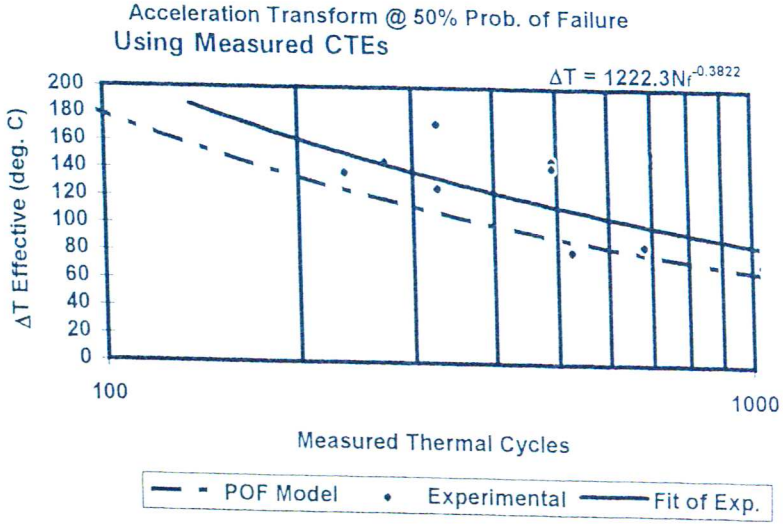


Hysteresis Plots for $L_d\Delta\alpha$=2592 X 10^{-6} mils/ ^{o}C


Acceleration Transform @ 5% Prob. of Failure
Using Measured CTEs
ΔT = 771.73Nf^-0.3454
ΔT Effective (deg. C)
180
160
140
120
100
80
60
40
20
0
100
1000
Measured Thermal Cycles
POF Model
Experimental
Fit of Exp.


Acceleration Transform @ 10% Prob. of Failure
Using Measured CTEs
ΔT= 996.08Nf^-0.3768
ΔT Effective (deg. C)
200
180
160
140
120
100
80
60
40
20
0
100
1000
Measured Thermal Cycles
POF Model
Experimental
Fit of Exp.


Acceleration Transform @ 25% Prob. of Failure
Using Measured CTEs
ΔT = 1103.9Nf^-0.3791
ΔT Effective (deg. C)
200
180
160
140
120
100
80
60
40
20
0
100
1000
Measured Thermal Cycles
POF Model
Experimental
Fit of Exp.


Acceleration Transform @ 50% Prob. of Failure
Using Measured CTEs
ΔT = 1222.3Nf^-0.3822
ΔT Effective (deg. C)
200
180
160
140
120
100
80
60
40
20
0
100
1000
Measured Thermal Cycles
POF Model
Experimental
Fit of Exp.

7. Refererences

[1]. Dasgupta, A. and Pecht. M., "Material Failure Mechanisms and Damage Models", *IEEE Transactions on Reliability*, Vol. 40, No. 4, pp. 531-536, 1992.

[2]. MIL-HDBK-217F, "Reliability Prediction of Electronic Equipment", Revision F, Department of Defense, 1992.

[3]. Hu, J. M. and Barker, D. "Design Approach of Reliable MCM Packages Based on Physics of Failure Models", *Proceedings of 1st International Conference on Multichip Modules*, IEPS and ISHM, pp. 386-393, 1992.

[4]. Pecht, M. (Ed.), *Integrated Circuit, Hybrid and Multichip Module Package Design Guidelines*, John Wiley and Sons, New York, 1994.

[5]. Hu, J.M., "Physics-of-Failure Based Reliability Qualification of Automotive Electronics," *Communication in Reliability, Maintainability, and Supportability, An International Journal,* Vol 1, No. 2, 1994.

[6]. Hu, J.M., Barker, D., Dasgupta, A., Arora, A., "The Role of Failure Mechanism Identification in Accelerated Testing," *Journal of the Institute of Environmental Science*, pp. 39-45, July 1993.

[7]. Rothman, T.R., Dasgupta, A., Binder M.C., "A Physics-of-Failure Case Study for Accelerated Testing of Electronic Packages," *Proceedings -Institute for Environmemtal Sciences*, Hawaii, 1995.

[8]. Jih, E., Pao, Y., "Evaluation of Design Parameters for Leadless Chip Resistor Solder Joints," *Transactions of the ASME*, pp 94-99, Vol. 117, June 1995.

[9]. Desaulnier, W.E., Binder, M.C., Al-Husseini, J.L., "A Modification of Engelmaier's Equation to Account for Leadless Solder Joint Bulbousness," *ASME Advances in Electronic Packaging*, EEP-Vol. 10-2, 1995.

[10]. Weiss, S., "Developing Automotive Reliability Models", *Test & Measurement Word*, pp. 27-28, February, 1993.

[11]. Askeland, Donald R., *The Science and Engineering of Materials*, Second Edition, PWS-Kent, pp. 472-473, 1989.

[12]. Miner, M.A., "Cumulative Damage in Fatigue", *Journal of Applied Mechanics*, vol. 12, 1945.

[13]. Clech, J.M., Noctor, D.M., Manock, J.C., Lynott, G.W., and Bader, F.E., "Surface Mount Assembly Failure Statistics and Failure Free Time", 44th Electronic Components and Technology Conference, Washington, D.C., May 1994.

[14]. Dally, J.W., Riley, W.F., and McConnell, K.G., *Instrumentation for Engineering Measurements*, second edition, John Wiley and Sons, New York, pp 531-533, 1984.

[15]. Frear, D.R., Grivas, D., and Morris, J.W. Jr., "Parameters Affecting Thermal Fatigue Behavior of 60Sn-40Pb Solder Joints", *Journal of Electronic Materials*, Vol. 18, No. 6, pp 671-680, 1989.

[16]. Box, G., Tiao, C., *Bayesian Interference in Statistical Analysis*, Addison Wesely Publ. Co., Reading Mass., 1973.

[17]. Lindley, D., *Scandinavian Journal of Statistics*, Vol 5., 1, 1978.

[18]. Barlow, R., Toland, R., "A Bayesian Analysis of the Stress Rupture Life of Kevlar/Epoxy Spherical Pressure Vessels", *Accelerated Life Testing and Expert's Opinions* .,

Italy, pp 203-236, 1988.

[19]. Institute for Interconnecting and Packaging of Electronic Circuits, *Guidelines for Accelerated Reliability Testing of Surface Mount Solder Attachments IPC SM-785*, March 1992.

[20]. Manson, S.S., *Thermal Stress and Low Cycle Fatigue*, McGraw-Hill, New York, 1966.

[21]. Morrow, J.D., "Cyclic Plastic Strain Energy and Fatigue of Metals", *ASTM STP 378*, ASTM, Philadelphia, PA, pp 45-87, 1964.

[22]. Wild, R.N., "Some Fatigue Properties of Solders and Solder Joints", *IBM Federal Systems Division IBM No. 73Z000421* ,Owega,NY, pp 45-87, Jan 1973.

[23]. Engelmaier, W., "Generic Reliability Figures of Merit Design Tools for Surface Mount Solder Attachments", *IEEE transactions on Components, Hybrids, and Manufacturing Technology*, Vol. 16, No. 1, pp 103-112, Feb., 1993.

[24]. Manson, S.S., Halford, G.R., and Hirshberg, M. H., "Creep-Fatigue Analysis by Strain-Range Partitioning ," *ASME Symposium on Design for elevated Temperature-Environment*, San Fransisco CA, 1971.

[25]. Dasgupta, A., Oyan, C., Barker, D., Pecht, M., "Solder Creep-Fatigue Analysis by an Energy Partitioning Approach ," *Transactions of the ASME*, Vol. 114 pp 152-160 June 1992.

[26]. Verma, S., Dasgupta, A., Barker, D., "A Numerical Analysis of J-Leaded Solder Joints Using the Energy Partitioning Approach ," *Transactions of the ASME*, Vol. 115 pp 416-423 December 1993.

[27]. Shine, M.C., Fox, L.R., "Fatigue of Solder Joints in Surface Mount Devices," *Special Technical Publication American Society for Testing and Materials* Philadelphia PA, 1987.

[28]. Conrad, H., Guo, Z., Sprecher, A.F., "Plastic Deformation Kinetics of Eutectic Pb-Sn Solder Joints in Monotonic Loading and Low-Cycle Fatigue," *Transactions of the ASME,* Vol. 114, pp 112-117, June 1992.

[29]. Shiratori, M., Yu, Q., Wang, S.B., "A Computational and Experimental Hybrid Approach to Creep-Fatigue Behavior of Surface-Mounted Solder Joints," ASME Advances in Electronic Packaging, EEP-Vol. 10-1, pp 451-457 1995.

[30]. Solomon, H.D., "High and Low Temperature Strain-Life Behavior of a Pb Rich Solder" *ASME Journal of Electronic Packaging*, Vol. 112 pp 123-128, June 1990.